

**A HIGHLY-SENSITIVE FIBER BRAGG GRATING TRANSVERSE STRAIN SENSOR  
USING MICRO-STRUCTURE FIBERS**

by

Charles M. Jewart

BSEE, University of Pittsburgh, 2004

Submitted to the Graduate Faculty of

SCHOOL OF ENGINEERING in partial fulfillment

of the requirements for the degree of

Master of Science in Electrical Engineering

University of Pittsburgh

2006

UNIVERSITY OF PITTSBURGH

School of Engineering

This thesis was presented

by

Charles M. Jewart

It was defended on

April 18, 2006

and approved by

Joel Falk, Professor, Department of Electrical and Computer Engineering

Steven Levitan, Professor, Department of Electrical and Computer Engineering

Thesis Advisor: Kevin Chen, Assistant Professor, Department of Electrical and Computer

Engineering

Copyright © by Charles M. Jewart

2006

**A HIGHLY-SENSITIVE FIBER BRAGG GRATING TRANSVERSE STRAIN  
SENSOR USING MICRO-STRUCTURE FIBERS**

Charles M. Jewart, M.S

University of Pittsburgh, 2006

In-fiber Bragg gratings are key components for optical sensing. As embedded sensors, in-fiber gratings find important applications in mechanical structural health monitoring, vibration detection, pressure monitoring and acoustic sensing. However, the current state-of-the-art grating sensors inscribed in standard fiber only provide for the detection of stress and vibration in one dimension, along the axial dimension (length) of the fiber.

In this thesis, we developed fiber Bragg grating sensors in specialty micro-structural fibers that can not only detect structural stress along the fiber, but also can detect stress along the transverse directions with high sensitivity. Finite element analysis (ANSYS) was used to design and study both longitudinal and transverse strain induced in microstructural fibers by external loads. Air holes were strategically placed in the fiber cladding to focus the external stress into the fiber cores to enhance the response of the fiber Bragg grating sensors. Stress-induced birefringence in the fiber core was studied in both standard and two-hole microstructural fibers with various air hole and fiber core configurations. Based on simulation studies, the optimal position to place the fiber core was determined to maximize the influence of transverse stress on the fiber cores. To validate the simulation results, Bragg grating sensors was inscribed in two-hole microstructure fibers for transverse stress sensing. Transverse stress, as measured by resonance peak splitting of the grating sensor, was used to compare with both predictions from simulation results. Both the simulation and measurement results indicate that the sensitivity of grating sensors to the transverse stress can be enhanced eight times more in a two-hole fiber than in a standard fiber.

## TABLE OF CONTENTS

<b>PREFACE.....</b>	<b>XII</b>
<b>1.0        INTRODUCTION.....</b>	<b>1</b>
1.1        MOTIVATION .....	1
1.2        OUR APPROACH.....	2
1.3        THESIS LAYOUT.....	3
<b>2.0        FIBER BRAGG GRATING BACKGROUND .....</b>	<b>5</b>
2.1        INTRODUCTION TO FIBER BRAGG GRATINGS AND THEIR FABRICATION.....	5
2.2        PHOTOREACTIVITY IN OPTICAL FIBER .....	15
2.3        FBGS AS SENSORS.....	19
2.4        TRANSVERSE STRAIN SENSOR .....	23
<b>3.0        THEORY .....</b>	<b>27</b>
3.1        STRESS IN A STRUCTURE .....	27
3.2        BIREFRINGENCE.....	36
<b>4.0        ANSYS MODELING .....</b>	<b>41</b>
4.1        FIBER MODELS.....	41
4.1.1    SMF-28.....	41
4.1.2    Two-Hole Fiber .....	43
4.2        ANSYS RESULTS.....	46

<b>4.2.1</b>	<b>Contour Plots.....</b>	<b>46</b>
<b>4.2.1.1</b>	<b>SMF-28.....</b>	<b>47</b>
<b>4.2.1.2</b>	<b>Two-Hole Vertical Orientation.....</b>	<b>49</b>
<b>4.2.1.3</b>	<b>Two-Hole Horizontal Orientation .....</b>	<b>51</b>
<b>4.2.1.4</b>	<b>45° Rotation .....</b>	<b>53</b>
<b>4.2.2</b>	<b>Stress through fiber .....</b>	<b>55</b>
<b>4.2.3</b>	<b>Peak Splitting Plots .....</b>	<b>56</b>
<b>4.2.3.1</b>	<b>SMF-28.....</b>	<b>56</b>
<b>4.2.3.2</b>	<b>Vertical Orientation.....</b>	<b>57</b>
<b>4.2.3.3</b>	<b>Horizontal Orientation.....</b>	<b>58</b>
<b>4.2.3.4</b>	<b>Splitting at 45 Degree Rotation .....</b>	<b>59</b>
<b>4.2.3.5</b>	<b>Splitting as a Function of Rotation.....</b>	<b>60</b>
<b>5.0</b>	<b>EXPERIMENT.....</b>	<b>62</b>
<b>5.1</b>	<b>FABRICATION AND SETUP .....</b>	<b>62</b>
<b>5.2</b>	<b>RESULTS .....</b>	<b>65</b>
<b>5.2.1</b>	<b>SMF-28.....</b>	<b>65</b>
<b>5.2.2</b>	<b>Two-Hole Fiber .....</b>	<b>67</b>
<b>5.2.3</b>	<b>Comparison with Simulated Results and Discussion of Error .....</b>	<b>69</b>
<b>6.0</b>	<b>CONCLUSION.....</b>	<b>71</b>
<b>6.1</b>	<b>SUMMARY .....</b>	<b>71</b>
<b>6.2</b>	<b>FUTURE WORK.....</b>	<b>72</b>
<b>6.2.1</b>	<b>Six-Hole Microstructured Fiber .....</b>	<b>73</b>
<b>6.2.2</b>	<b>Pressure Sensor .....</b>	<b>77</b>

<b>BIBLIOGRAPHY .....</b>	<b>83</b>
---------------------------	-----------

## **LIST OF TABLES**

Table 1 Fiber Parameters .....	40
Table 2 Material Properties of Fused Silica in $\mu$ MKS units .....	41

## LIST OF FIGURES

Figure 1 Illustration of a uniform Bragg grating. Included is an example of the transmission spectrum.....	6
Figure 2 Schematic of a typical setup for internally inscribing FBGs.....	7
Figure 3 Schematic of setup used for amplitude splitting.....	8
Figure 4 Schematic of prism interferometer used to fabricate FBGs .....	9
Figure 5 Lloyd interferometer.....	9
Figure 6 Illustration of point-by-point fabrication setup .....	10
Figure 7 Schematic of phase mask geometry for inscribing Bragg gratings into optical fiber ...	12
Figure 8 Photograph of FBG being written using phase mask technique.....	13
Figure 9 Photograph of first-order diffraction pattern .....	14
Figure 10 Sample reflection spectrum of FBG for both unapodized (a) and apodized (b) .....	15
Figure 11 Figure of bond structures for photo-sensitization and recombination process.....	17
Figure 12 Examples of low-pass filtering techniques for FBG sensor systems (a) and a sensor system employing a low pass filter technique (b).....	20
Figure 13 Schematic of PM fiber used by Lawrence <i>et al.</i> [3] .....	24
Figure 14 Reflection spectra of PM fiber used by Lawrence <i>et al.</i> [3].....	24
Figure 15 Reflection spectra from Silva-Lopez <i>et al.</i> for two orientations of multi-core fiber [6] .....	25
Figure 16 Three dimensional Cartesian Stress.....	28

Figure 17 Isotropic crystal Matrix .....	31
Figure 18 Two dimensional plan stress and plane strain problems .....	33
Figure 19 Two-dimensional triangular three-node element.....	34
Figure 20 SMF-28 Simulation Model.....	43
Figure 21 Cross-Section of two-hole fiber .....	44
Figure 22 Illustration of two-hole fiber with dimensions .....	45
Figure 23 Two-Hole Fiber Simulation Model, Holes in the Vertical Orientation.....	46
Figure 24 Stress in the X-direction ( $\sigma_x$ ) for SMF-28.....	47
Figure 25 Stress in the Y-direction ( $\sigma_y$ ) for SMF-28 .....	48
Figure 26 Stress in the X-direction ( $\sigma_x$ ) for two-hole fiber in the vertical orientation .....	49
Figure 27 Stress in the Y-direction ( $\sigma_y$ ) for two-hole fiber in the vertical orientation .....	50
Figure 28 Stress in the Y-direction ( $\sigma_y$ ) for two-hole fiber in the horizontal orientation .....	51
Figure 29 Stress in the X-direction ( $\sigma_x$ ) for two-hole fiber in the horizontal orientation .....	52
Figure 30 X-Component ( $\sigma_x$ ) of two-hole fiber rotated 45° .....	53
Figure 31 Y-Component ( $\sigma_y$ ) of two-hole fiber rotated 45° .....	54
Figure 32 Stress vs. distance between the air holes in two-hole fiber (F=50-N).....	55
Figure 33 Peak splitting plot for SMF-28 .....	56
Figure 34 Peak splitting of two-hole fiber in the vertical orientation.....	57
Figure 35 Peak splitting of two-hole fiber in the horizontal orientation.....	58
Figure 36 Peak splitting for two-hole fiber at 45° rotation .....	59
Figure 37 Peak splitting as a function of rotation (F=50-N/cm).....	60
Figure 38 Illustration of experimental setup.....	63
Figure 39 Photograph of rotation stage (1), load cell (2), compression stage (3), microscope objective (4) and CCD camera (5) .....	64

Figure 40 Simulated and experimental results plot for SMF-28. The solid lines represent the simulated values.....	65
Figure 41 Normalized spectral response of solid fiber at 197-N/cm.....	66
Figure 42 Simulated and experimental results for two-hole fiber in vertical and horizontal orientations. The solid lines represent the simulated values.....	67
Figure 43 Normalized spectral response of two-hole fiber for both vertical and horizontal orientations at 80-N/cm.....	68
Figure 44 Cross sectional photograph of six-hole microstructured fiber (provided by Dr. John Canning of Optical Fiber Technology Center at the University of Sydney, Sydney, Australia)..	73
Figure 45 Meshed ANSYS model of six-hole microstructured fiber .....	74
Figure 46 Six-Hole microstructured fiber X-component of stress (F=50-N/cm) .....	75
Figure 47 Six-Hole microstructured fiber Y-component of stress (F=50-N/cm) .....	76
Figure 48 Two-hole fiber with 100-Bar of pressure in both holes, $\sigma_x$ .....	78
Figure 49 Two-hole fiber with 100-Bar of pressure in both holes, $\sigma_y$ .....	79
Figure 50 Two-hole fiber with 100-Bar of pressure in one hole, $\sigma_x$ .....	80
Figure 51 Two-hole fiber with 100-Bar of pressure in one hole, $\sigma_x$ .....	81

## **PREFACE**

I would first and foremost like to thank Dr. Chen, without his guidance none of this would ever have been possible. Thanks to Ben McMillen for his ability to make up for my shortcomings in all things mechanical. Thanks to Mike Bails for teaching me how to use ANSYS. Thanks to Dr. Falk for his help with the theory and Dr. Levitan for him being on my committee.

## **1.0 INTRODUCTION**

### **1.1 MOTIVATION**

Fiber Bragg Gratings (FBGs) are important components for optical sensing and communication. These in-fiber components offer advantages over other preexisting optical and electronic devices. These include low manufacturing costs, immunity to electromagnetic fields (EMF), long lifetime, high sensitivity and are ideal for deployment in harsh environments. The small size and low loss characteristics of the optical fiber allow for the deployment of sensor networks for multiple-point-long distance remote sensing. Embedding these structures can provide real-time information on structural behavior.

Strain and vibration sensing is an important application of FBG sensors [1, 2]. To date FBG sensors have been widely used for manufacturing process monitoring and structural health monitoring of dams, buildings, jetliners and spacecraft. Embedding these sensor networks into a material is ideal, not only due to their low-cost, but also because they are less invasive than traditional sensors. In turn they have the ability to give immediate feedback on how the internal stresses and strains are affecting the material in which they have been deployed without having an adverse affect on the surrounding material's structural integrity.

The majority of FBG sensors have the ability to measure the axial components of the strain along the fiber [1]. However, in an embedded sensor it is desirable to have the ability to measure the strain transverse to the fiber, which would give a complete three-dimensional view of the internal stresses and strains. In order to have the ability to measure the stress in a structure it is necessary to obtain more than one component of the strain along the fiber, being that the stress in a structure is a composite of the multiple strains. Typically, in order to accomplish this, it would be required to deploy multiple sensors into the structure. This could weaken the host structure, and the near presence of other sensor could make the measurements difficult to isolate

from each other. Therefore it is desirable to be able to monitor the necessary strains with a single fiber.

The presence of transverse strain in the fiber changes the refractive-index profile of the fiber and thus creates an induced birefringence effect. Studies have been carried out on the birefringence induced in the fiber due to an external load. It was demonstrated by Lawrence *et al.* [3] that the Bragg wavelength shifts corresponding to the two orthogonal modes present in polarization maintaining fiber increases linearly with the applied load. In standard fiber however, the resonant peak wavelength will split into these two polarizations due to the stress induced birefringence as predicted by the modeling done by Gafsi and El-Sherif [4]. These well defined peaks also increase linearly with the increased load and allow for determining the magnitude of the load applied to the fiber. However, at smaller loads the splitting is less defined, and more difficult to differentiate. Ye *et al.* [5] employed a polarization maintaining fiber-coupler in order to avoid this problem and also showed that using this technique imposed no limits on the observable strain. Recently, Silva-Lopez *et al.* [6] presented experimental measurements of the peak splitting in a multi-core fiber. By comparing the FBG peak splitting and shift in fiber cores located in different locations of the fiber, both magnitude and the orientation of the transverse stress were measured using a single fiber.

## 1.2 OUR APPROACH

Standard telecommunications fiber however is not designed for the purpose of measuring transverse strain. In standard SMF-28 the core is located in the center of the fiber, thus causing the stress to decrease to a minimum in the center, with the maximum on the outer edges. Gafsi and El-Sherif [4] predicted that an approximately 50-N/cm applied force to the FBG would result in a 0.3 and 0.03-nm shift of the X and Y-polarizations, respectively. This small shift in the resonant wavelength peak requires the use of additional optical elements in the sensing system, such as a polarizer in order to resolve the peak splitting.

Our solution addresses this problem by designing microstructure fiber with strategically placed air-holes in the fiber cladding. The addition of these air holes allows one to control how

the stress is distributed in the fiber's core. This causes the applied loads to have a maximum impact on the fiber's core. The introduction of air holes also breaks the symmetry of the fiber structure since they are placed asymmetrically. Thus fiber sensors become sensitive to both the magnitude and the orientation of the external force. For this work we used a two-hole fiber that was 220- $\mu\text{m}$  wide with two 90- $\mu\text{m}$  wide air holes.

In order to accurately model the stress in the fiber, finite element analysis (FEA) was preformed on both SMF-28 and the two-hole fiber using ANSYS v. 10.0, a powerful tool commonly employed in mechanical and civil engineering. The principles from civil engineering still apply here, except now the structure is on the micron scale as opposed to the macro scale. Here the FEA models were used to predict the peak splitting characteristics of both of the fibers so that there would be a correlation to the experimental results. The two-hole fiber was inscribed with a 1-cm Bragg grating. An external load was applied to the fiber, resulting in a peak splitting of the resonant wavelength. The observed peak splitting was in good agreement with the results obtained from the simulations.

### 1.3 THESIS LAYOUT

Chapter two of this thesis emphasizes the background of Fiber Bragg Gratings. Beginning with and introduction as to what a FBG is and how it operates. This includes a discussion of the Bragg condition as it relates to optical fiber. The history of the gratings is then discussed beginning with their discovery and the different fabrication techniques. The technical aspects of photosensitivity in optical fibers are discussed along with methods of making fiber photosensitive. Different methodologies for using FBGs as sensors are discussed along with how the sensing systems work. Technical details of FBGs are discussed including wavelength division and time division multiplexing and strain and temperature discrimination. The chapter ends with discussions of previous work done on transverse strain sensors and includes a discussion of our work.

Chapter three covers the necessary theoretical background to understand the work done in this thesis. A definition of stress is defined for a material and this is expanded into how the

stress relates into FEA. The birefringence is then discussed. This includes the derivations from Gafsi and El-Sherif [4] that relates the stress to an induced wavelength shift for optical fiber.

The ANSYS modeling is covered in chapter four. This includes how the fiber models were created in ANSYS (dimensions, material properties) and how the simulations were setup in the software for both SMF-28 and two-hole fiber. The results obtained from ANSYS are presented. These include contour plots of the stress through both types of fibers in both orientations. The theoretical peak splitting is presented in plots for SMF-28 and the two-hole fiber for vertical and horizontal orientations, along with how the stress reacts between the air holes for both orientations.

Chapter five covers the experimental section of the thesis. It opens with how the FBGs were fabricated in our lab. The experimental setup used to obtain our results is presented. Finally the results obtained from the experiment are presented along with how they compare to the simulated results obtained from ANSYS.

Chapter six concludes this work with a summary of the thesis and the future work.

## **2.0 FIBER BRAGG GRATING BACKGROUND**

### **2.1 INTRODUCTION TO FIBER BRAGG GRATINGS AND THEIR FABRICATION**

A Fiber Bragg Grating (FBG) consists of a length of Single Mode Fiber (SMF) that has a periodic change in the refractive index of the fiber core. The light propagates down the fiber's core, and the light will be scattered at each index of refraction perturbation. This results in a notch in the transmission spectrum of the fiber, while in the more widely used reflection spectrum a well defined peak is seen. The Bragg condition is defined as

$$\lambda_B = 2n_{eff}\Lambda \quad (2.1)$$

where the Bragg wavelength ( $\lambda_B$ ) is the center wavelength of the reflected light,  $n_{eff}$  is the effective index of refraction of the fiber core and  $\Lambda$  is the period of the grating [1]. In Figure 1 a schematic of a FBG is shown along with a typical spectrum for transmission and reflection spectrums.

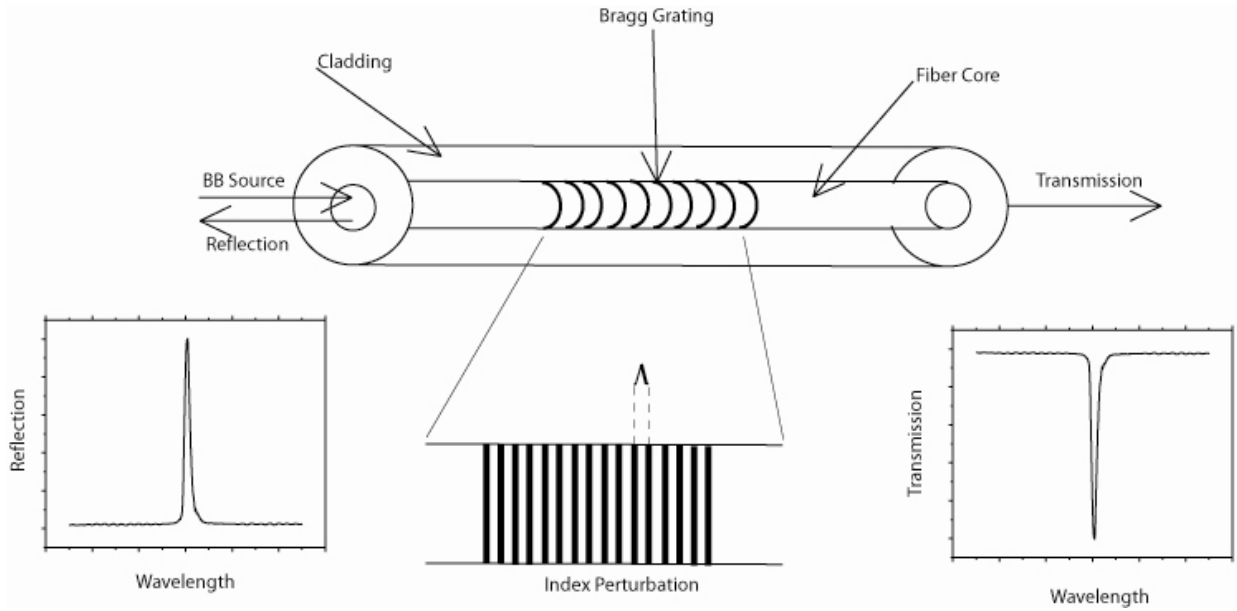


**Figure 1** Illustration of a uniform Bragg grating. Included is an example of the transmission spectrum

Over the years there have been several techniques developed to inscribe gratings into optical fiber. The first of these was discovered by Hill *et al.* [7] in 1978 and is called the internal inscription technique. This method requires the use of an argon ion laser (514.5 or 488-nm) to create a standing wave pattern in the fiber core. The creation of the standing wave arises from the incident light interfering with the reflection from the cleaved end of the fiber. The points where constructive interference occurs have a higher intensity. These points permanently change the index of refraction and in turn create a periodic perturbation to create a Bragg grating. A schematic of this setup is shown below in Figure 2 with the argon light creating the standing wave pattern. While this method is one of the easier methods to create FBGs, the downfall of this technique is that the Bragg wavelength is based upon the incident laser wavelength and therefore fabrication techniques are limited. Also, in order to obtain a useful reflection spectrum from this method, the grating needs to be quite long, typically on the order of a few tens of centimeters in length. [1]

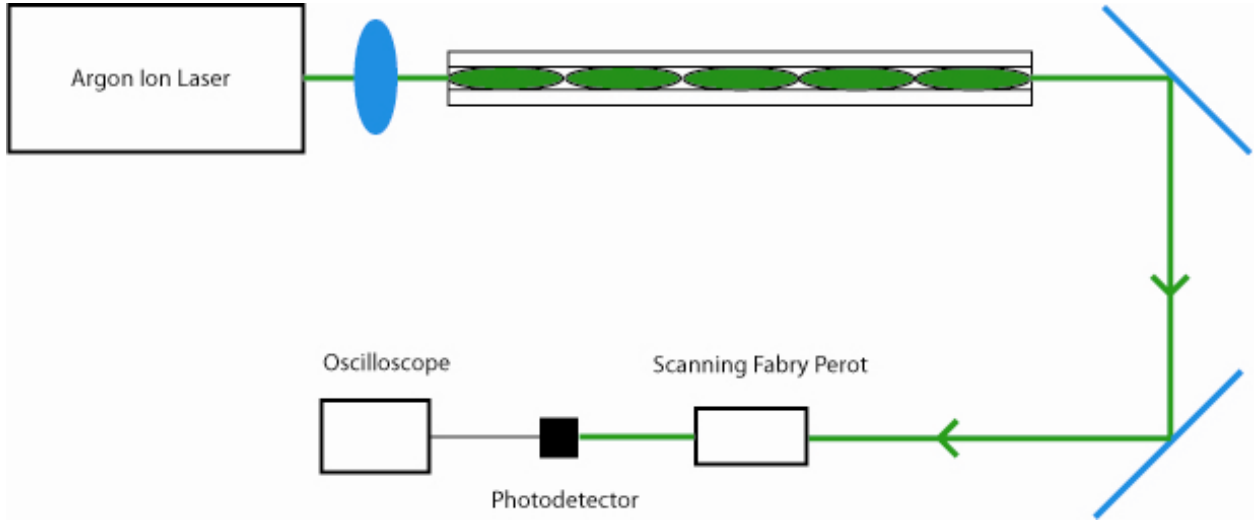


**Figure 2** Schematic of a typical setup for internally inscribing FBGs

An improved method of inscribing FBGs is the interferometric technique. There are two different methods that employ interferometers for making FBGs, these are the amplitude and wavefront splitting techniques. The amplitude splitting method was first developed by Meltz *et al.* [8] and uses a tunable excimer pumped dye laser with a wavelength between 486 and 500-nm which is frequency doubled into the UV spectrum (244-nm). The beam is split into two equal beams that when recombined create an interference pattern on the fiber. A schematic for this setup can be found below in Figure 3. In this figure one can see the splitting of the beam that creates the two different path lengths and in turn the interference pattern on the fiber. The major drawback of this method is that it is very susceptible to mechanical vibrations. Displacements in the optical components can cause the beam to drift and wash out the grating in the fiber. The wavefront method, while not as widely used as the amplitude splitting technique, does have some advantages. There are two possible ways of implementing this method. The first requires the use of a prism interferometer (as depicted in Figure 4) and the other uses a Lloyd interferometer (depicted in Figure 5) and requires the use of a lens and a dielectric mirror. Both of these methods require a UV source with good spatial coherence. The major benefit of this method is that both interferometers only have a single optical component, which causes a reduction in the

sensitivity to vibrations. The major drawback of the two wavefront methods is that the grating's length is limited to half the beam's width, and the wavelength tuning is restrained by the interferometer. [1]

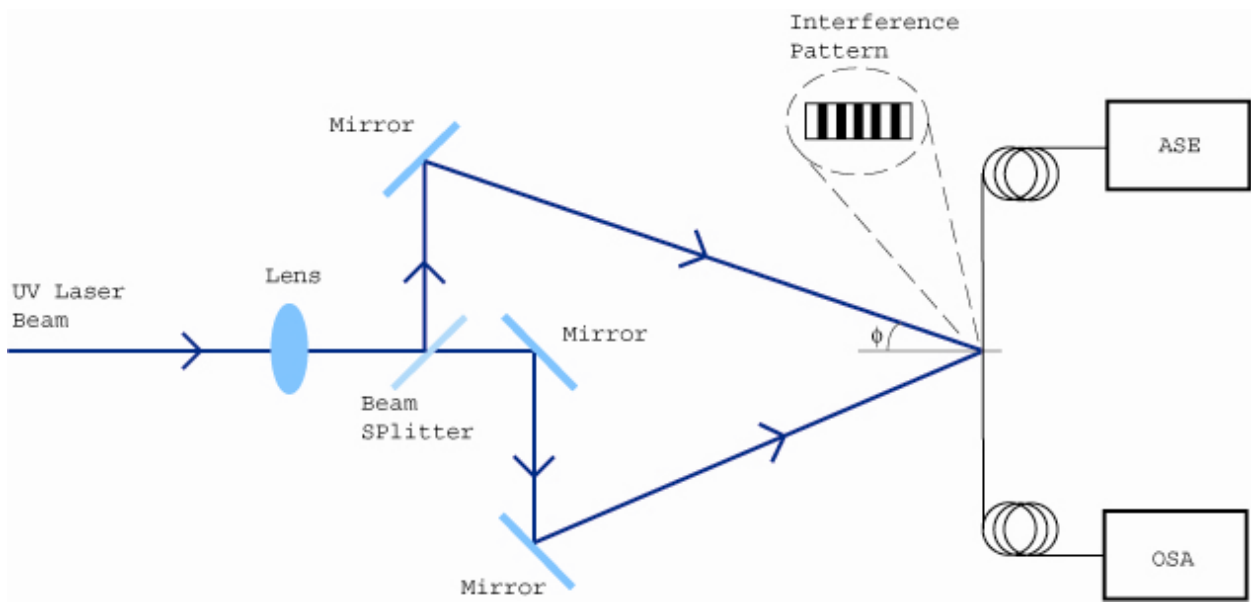


**Figure 3** Schematic of setup used for amplitude splitting

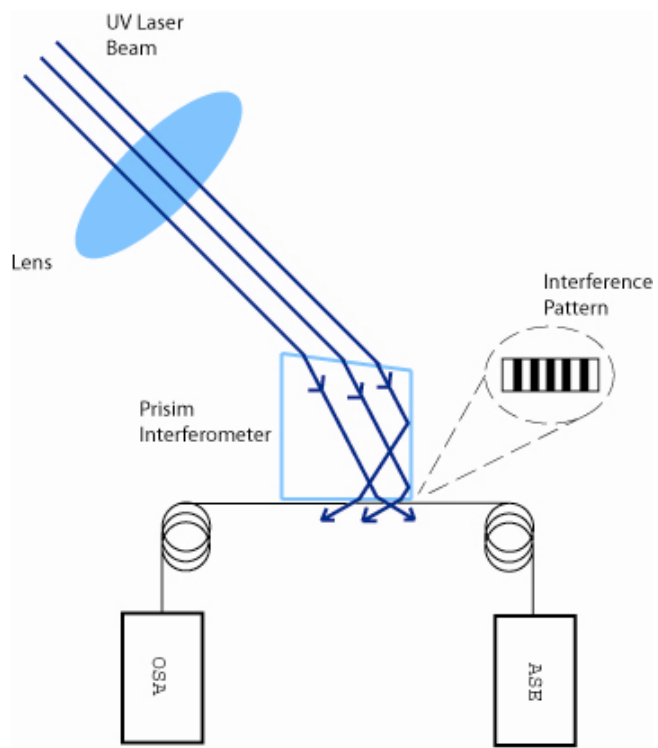


**Figure 4** Schematic of prism interferometer used to fabricate FBGs

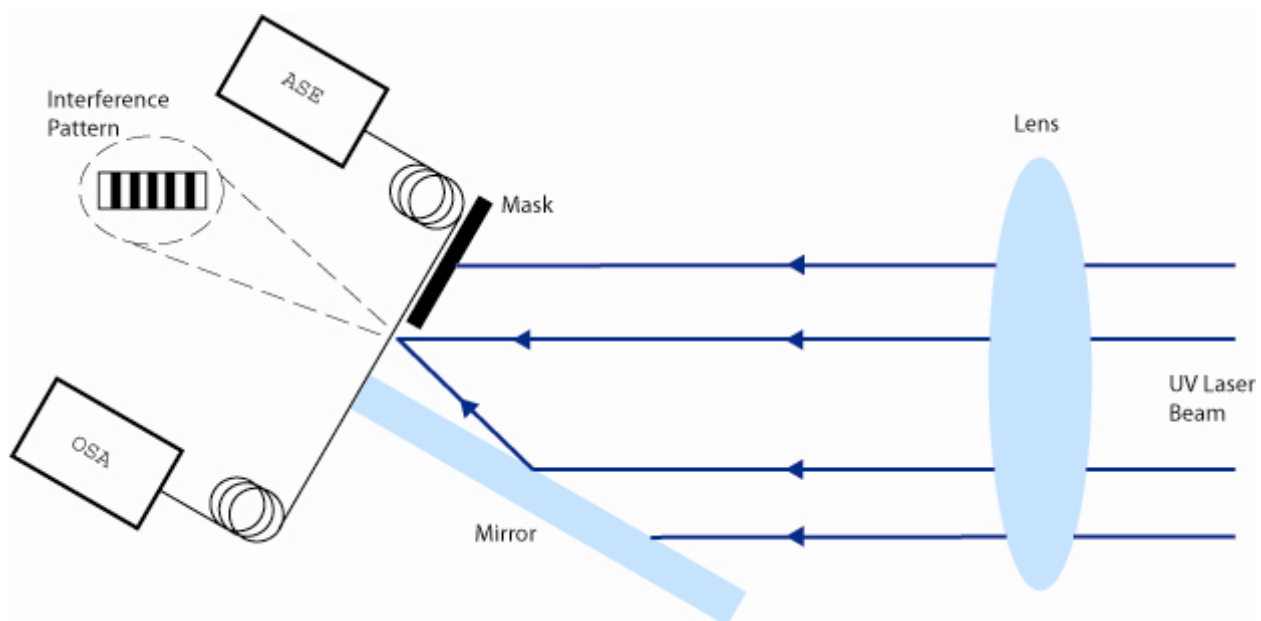


**Figure 5** Lloyd interferometer

One of the more flexible methods in inscribing Bragg gratings into optical fiber is the point-by-point method. This method uses a UV source that is passed through a slit and then focused down onto the fiber to produce an index change at one point. The fiber is then shifted a distance  $\Lambda$ , which corresponds to the period of the Bragg condition. A schematic of this setup is shown in Figure 6 which shows the UV source being passed through a slit. The advantages of this procedure are that it allows a great deal of flexibility in the grating, including the length, pitch and response. Therefore, with the same setup it is possible to create different grating structures without having to replace any components. However, during the writing process thermal effects and fiber strain have a greater effect on the grating and the spacing. Therefore the grating's length typically needs to be relatively short and groups such as Malo *et al.* [9] have only been able to create second and third order gratings. [1]

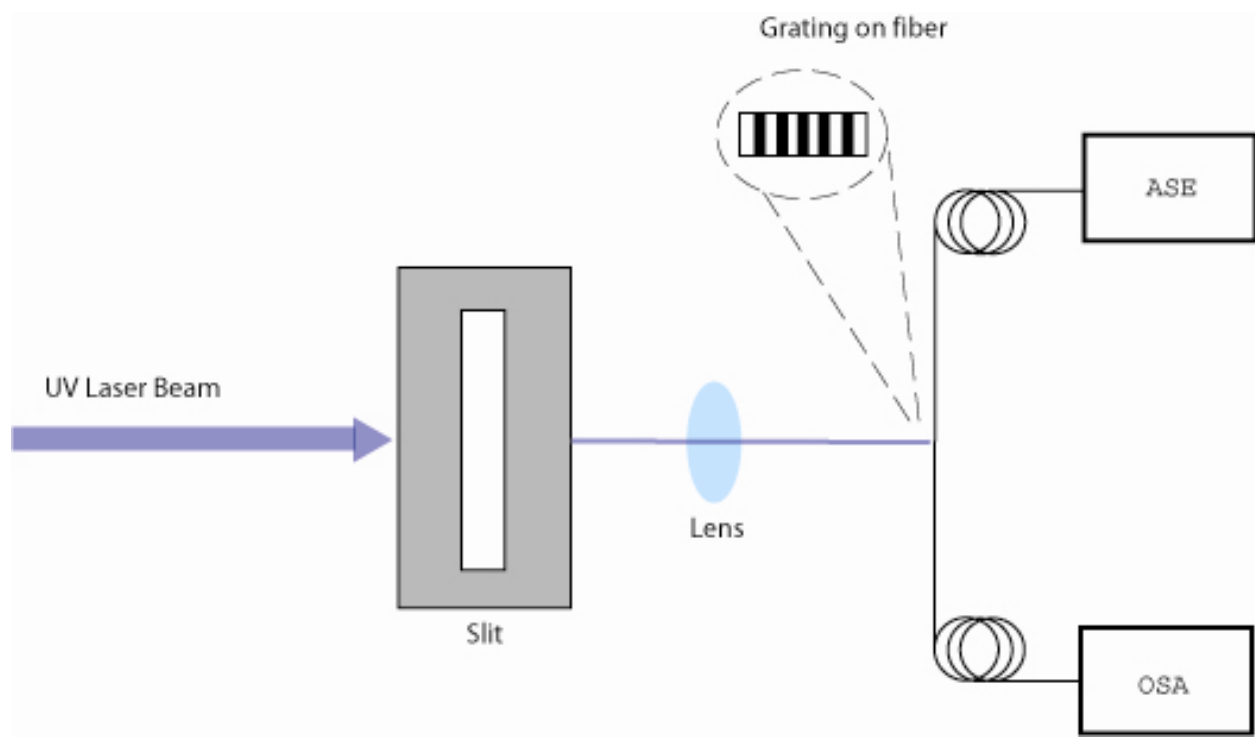


**Figure 6** Illustration of point-by-point fabrication setup

The phase mask technique for writing gratings is one of the most effective methods to fabricate gratings. It was first demonstrated by Hill *et al.* [7] and is currently the method employed in our lab. This uses a diffractive optical element to spatially modulate the incident UV beam. The two types of phase masks are those formed by e-beam lithography and those formed holographically. The benefit of the holographic method over the e-beam is that there is no stitch error in the grating pattern on the mask. The phase mask has a period  $2\Lambda$  where  $\Lambda$  is the same period used in the Bragg condition. With the proper depth of the phase mask the zero-order is canceled out and the plus and minus first-order diffraction beam contains most of the light's power. This is used to create an interference pattern on the fiber, and when the fiber is placed close enough, a permanent change is created in the fiber's core. This in turn causes the periodic structure to be inscribed into the fiber core [1]. An illustration of this technique is given below in Figure 7. Figure 8 shows a photograph taken from our lab of the phase mask with the fiber glowing under the UV light. Figure 9 is a photograph taken from our lab of the plus and minus first-order diffraction pattern.

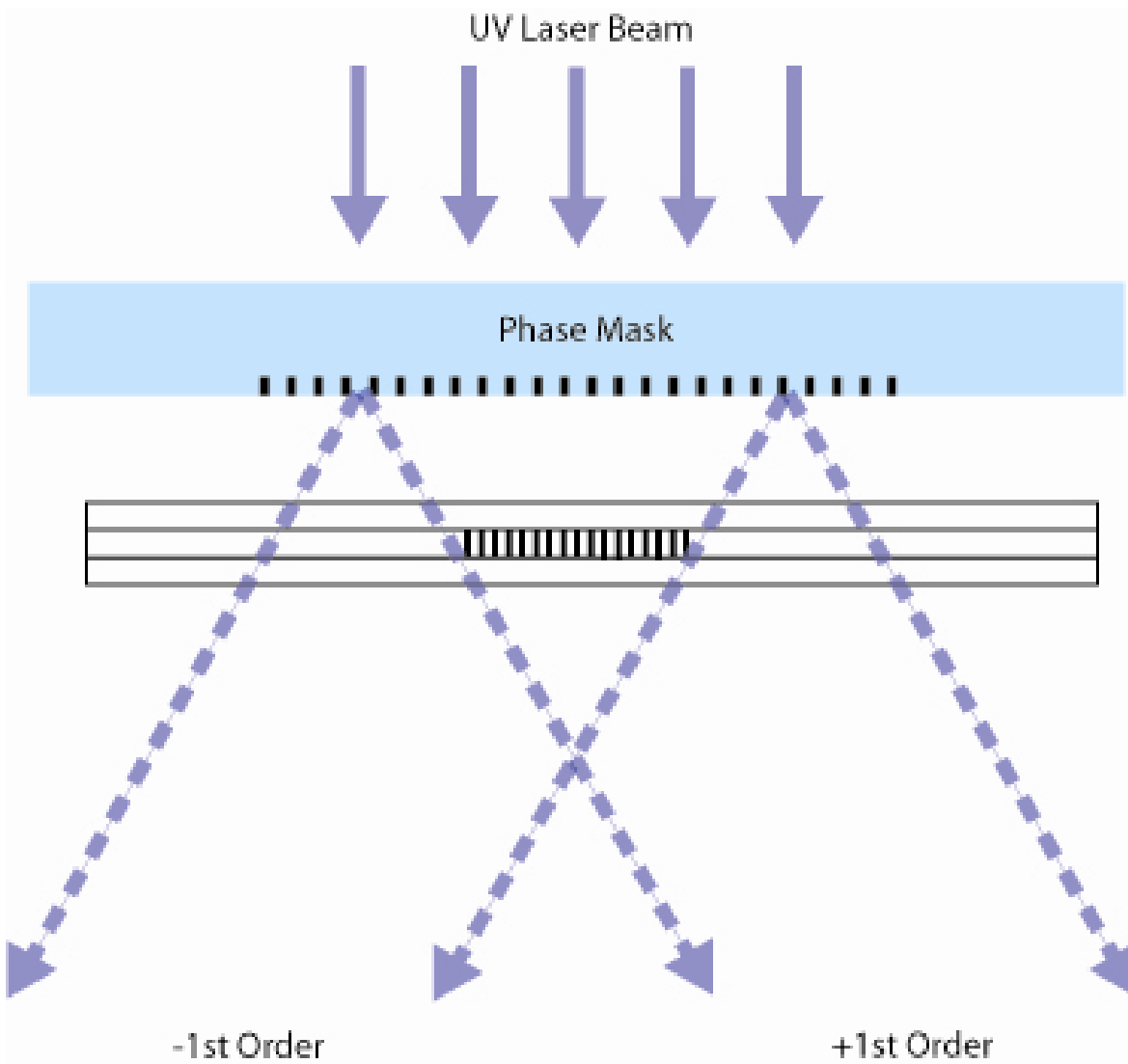


**Figure 7** Schematic of phase mask geometry for inscribing Bragg gratings into optical fiber

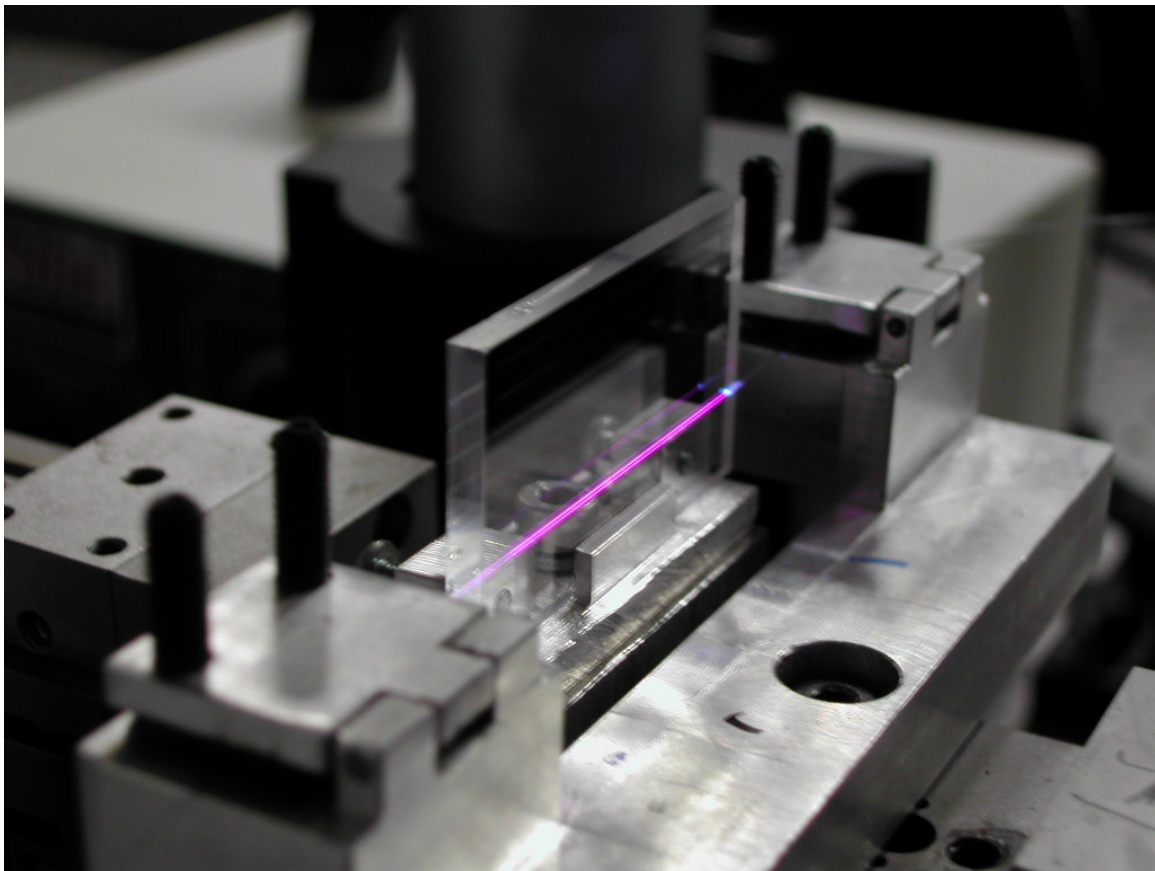


**Figure 8** Photograph of FBG being written using phase mask technique

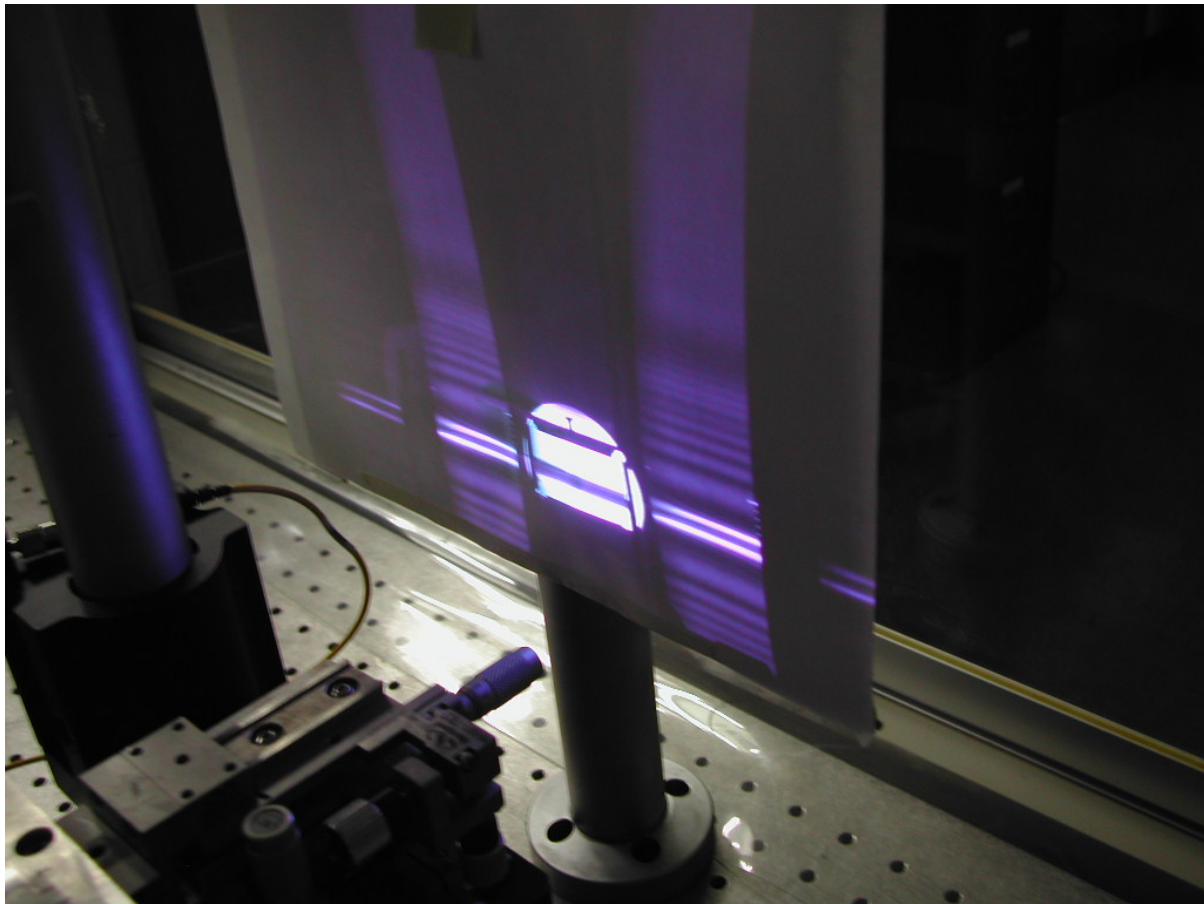


**Figure 9** Photograph of first-order diffraction pattern

The main peak in the reflection spectrum in a length of fiber with a constant perturbation in the index of refraction is shown in Figure 10a and 10b. In addition to the main peak there are also additional side lobes present. In many applications it is desirable to reduce or eliminate these side lobes. This is known as apodization. Apodization is accomplished by varying the amplitude of the coupling coefficient along the length of the grating. This is done by the inclusion of a phase mask that has a Gaussian profile for the diffraction efficiency and was first demonstrated by Albert *et al.* [11]. Apodization is applicable to all FBGs regardless of the writing technique. Figure 10a is an example of a unapodized grating while 10b is an apodized grating; both were fabricated in our lab. [1]

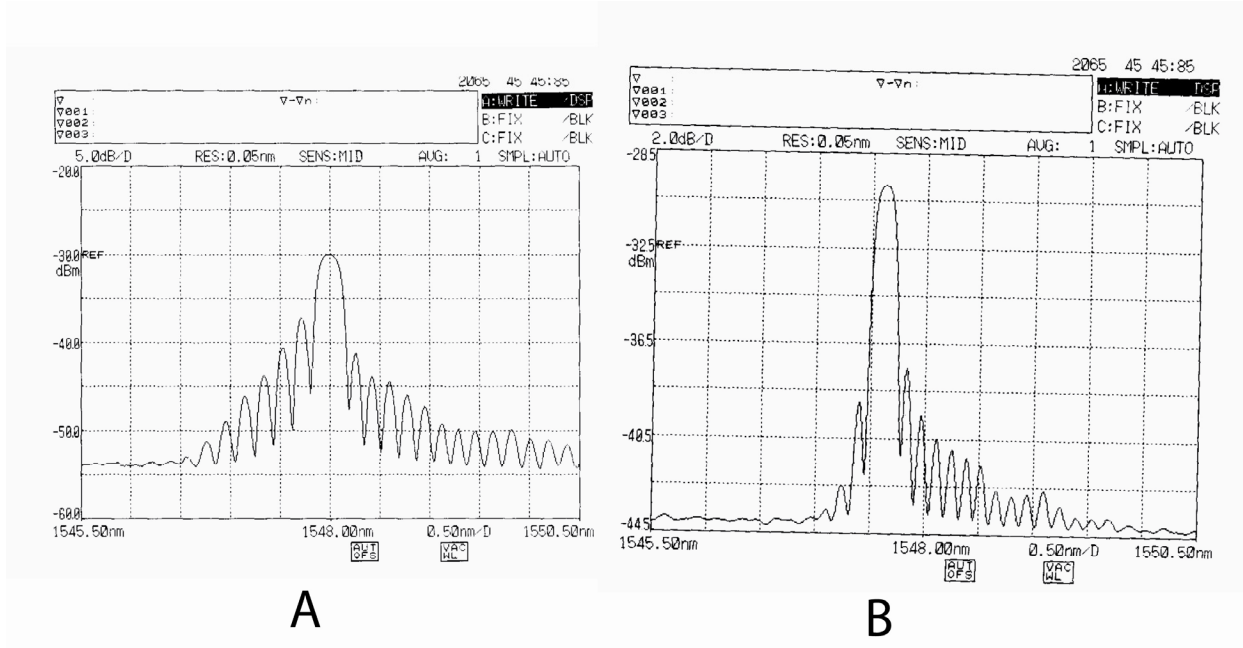


**Figure 10** Sample reflection spectrum of FBG for both unapodized (a) and apodized (b)

## 2.2 PHOTOREFRACTIVITY IN OPTICAL FIBER

The reason that it is possible to inscribe Bragg gratings into optical fiber is because the fiber is photosensitive. Hill *et al.* [10] were the first to demonstrate the photosensitivity of optical fiber in 1978. This discovery lead to the internal inscription technique and was discussed in the previous section. Further advancements were made on the photosensitivity of optical fiber. Lam and Garside [12] determined that the change in the refractive index reported by Hill was due to two-photon absorption. They went on to state that using a UV light source would be more efficient in the fabrication of FBGs. The second important discovery was found by Stone [13], in which he showed that a change in refractive index could be induced in all germanium (Ge) doped fiber. Until this discovery the only fiber available that was photosensitive was a small core fiber that was developed and made by Bell Northern Research. This report led to world-wide interest in the photosensitivity of optical fibers. Meltz *et al.* [8] developed the third breakthrough, the side writing technique known as the interferometric method of inscription.

Despite the fact that photosensitivity in fiber was discovered almost thirty years ago the principles behind it are still not well understood. However, there are two theories that are well conceived, color centers and densification. Doped glass has many defects that have strong absorption, known as color centers. This theory was first proposed by Hand and Russell [14], where they state that the color centers are most likely the result of Ge-Si wrong bonds that are referred to as GODC (germanium-oxygen deficiency center). GODC is a result of high temperature chemical-vapor deposition where GeO becomes more stable than the present  $\text{GeO}_2$ .

The GODC wrong-bond has strong absorption at 240-nm. This leads to the bleaching of the color centers which in turn changes the absorption spectrum in the visible and IR regions and is related to the Kramers-Kronig relationship. When exposed to the UV source, the absorption breaks the wrong-bonds in the glass and creates  $\text{GeE}'$ . The free electron then moves throughout the glass matrix until it reattaches to either  $\text{Ge}(1)$  or  $\text{Ge}(2)$ . This process is depicted below in Figure 11. This theory allows for the change in index of refraction from  $10^{-5}$  to  $10^{-4}$  but cannot account for a change in index of refraction greater than  $10^{-4}$ .

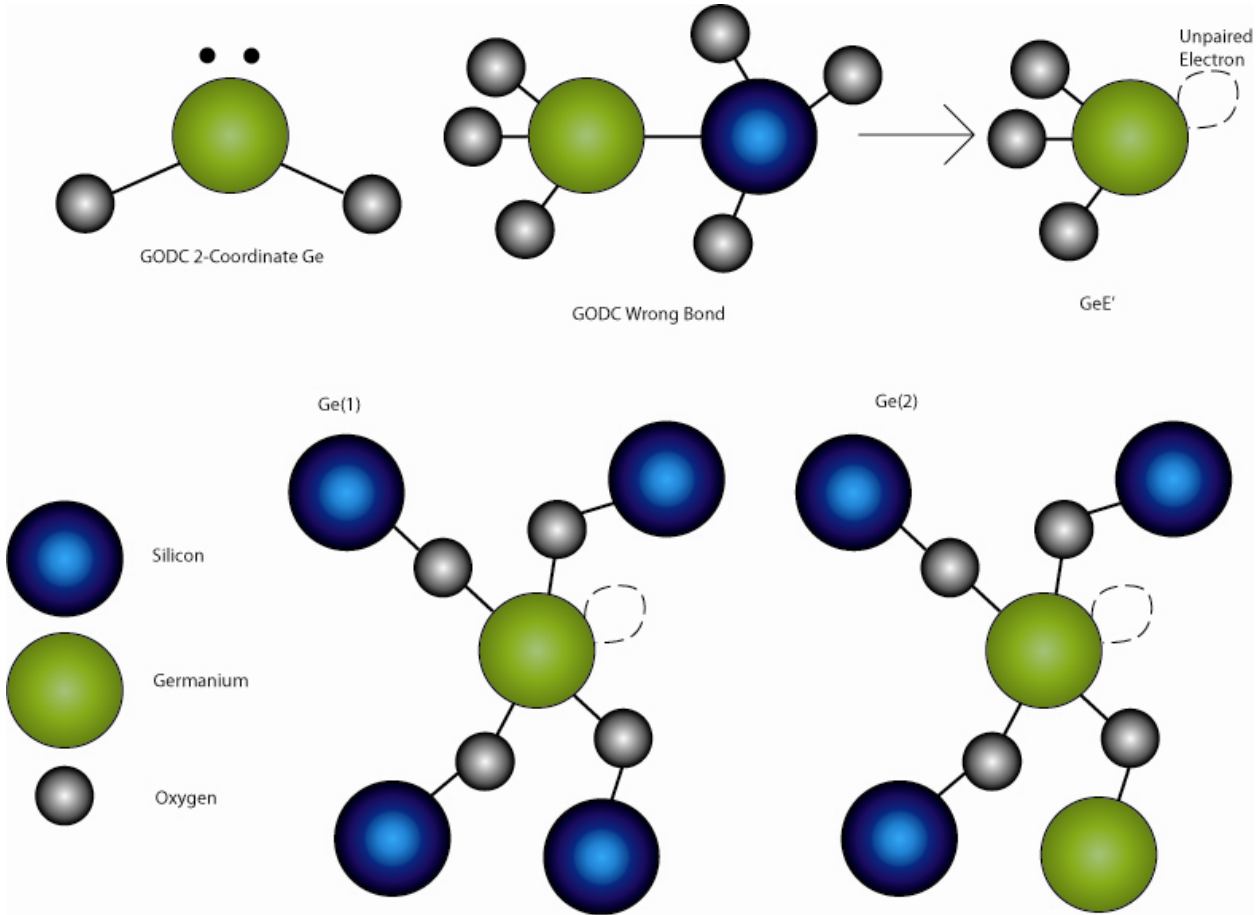


**Figure 11** Figure of bond structures for photo-sensitization and recombination process

Densification comes from the change in the optical density of a material through photolytic defect transformation. The change in the index of refraction is related by the Lorentz-Lorenz equation [15],

$$\Delta n = \frac{(n^2 - 1)(n^2 + 2)}{6n^2} \left( \frac{\Delta\alpha}{\alpha} - \frac{\Delta V}{V} \right).$$

Where  $\Delta\alpha$  is the change in the electric polarizability and  $\Delta V$  is the change in the material's volume. Looking at the equation it is easy to see that as the volume decreases the change in the index of refraction will increase. However, it is important to note that the principles behind polarizability and compaction are not well understood.

Most optical fiber has weak photosensitivity, typically on the order of  $10^{-5}$  to  $10^{-4}$ . Over the years several methods have been developed in order to enhance the photosensitivity (and

therefore the change in index of refraction). These include hydrogen loading, flame brushing, ion implantation and the addition of other dopants [1, 16, 17].

The most commonly used technique to enhance optical fiber's photosensitivity is hydrogen loading (hydrogenization) and was first developed by Atkins *et al.* [16] This method is beneficial in that it allows any optical fiber to have Bragg gratings inscribed in them. At high pressures ( $\sim 1100$ -psi), hydrogen molecules diffuse into the fiber's core. The hydrogen that is diffused into the fiber reacts with the Ge-O-Si bonds under UV laser radiation. This in turn creates additional OH. This increases the oxygen deficiency and follows the reaction process of GODC described earlier. The addition of more OH in turn increases the amount of GODC present in the fiber and thus increases the amount of absorption at 240-nm. The obtainable index change in the fiber is increased to the order of  $10^{-3}$  to  $10^{-2}$ . It typically takes a week of hydrogen soaking in order to obtain the desired photosensitivity in the fiber. The time required can be lessened to two days by increasing the temperature ( $\sim 150^\circ\text{C}$ ) during the loading process.

The downside of this process is that it uses high pressure hydrogen, which in itself is very dangerous and requires special precautions. The time required to obtain the necessary sensitivity can take up to several weeks and therefore large quantities of fiber are typically loaded at a time which requires storing at very cold temperatures ( $-40^\circ\text{C}$ ) to keep the hydrogen from out diffusing. Also, the method by which hydrogenization works is that it causes an increase in OH in the fiber. This creates problems in that OH absorbs in the  $1.3\text{-}\mu\text{m}$  telecomm window. While the excess hydrogen can be out-diffused by thermal annealing, this process can shift the resonance peak up to a few nanometers, thus causing difficulties in reproducing the same grating center repeatedly.

Similar to hydrogen loading in increasing photosensitivity is flame brushing. This method increases the sensitivity in local areas in waveguides by using multiple brushings with a hydrogen flame around  $1700^\circ\text{C}$ . Like hydrogen loading this method obtains an index change around  $10^{-3}$ . The biggest disadvantage is that the exposure to the flame greatly reduces the durability of the fiber and increases the likelihood of the fiber breaking. [1]

Ion implantation is used to increase local areas of optical waveguides and fused silica. In fact ion implantation is the only method that has the ability to make pure fused silica photosensitive. It works by shooting ions at an optical material at energies between 100keV and 5Mev with densities between  $10^{14}$  and  $5 \times 10^{17}$  ions/cm $^2$ . The ions rearrange the structure of the

material and causes surface defects due to bonds being broken. When exposed to UV radiation, the region that was exposed to the ions exhibits a negative index change as opposed to an increase. Verhaegen *et al.* [17] showed that in fused silica implanted with Si<sup>2+</sup> ions at 5MeV, exposed with 1kJ/cm<sup>2</sup> ArF UV light, that they obtained an index change of -1.8x10<sup>-3</sup>.

In addition to the mentioned methods, which are used to enhance the sensitivity of the fiber after it is made, using other dopants beforehand has shown an increase in the photosensitivity of fiber as well. This method is desirable because it is possible to obtain high sensitivities without hydrogen loading the fiber. It requires adding other dopants to the Ge during the fiber drawing process and typically includes boron, aluminum and tin. [1]

### 2.3 FBGS AS SENSORS

The most influential impact of FBGs is their ability to act as application specific sensors. This is accomplished by monitoring the wavelength shift of the reflection spectrum. The spectrum will change based on environmental conditions, specifically applied strain and the surrounding temperature for quasi-static point sensing. The principle behind the spectrum's shift from an applied strain is that it stretches the fiber, in turn causing an increase in the pitch of the grating. Another factor is that the index of refraction changes from the strain due to photoelasticity. The temperature dependency arises from the thermal expansion of the fiber material (silica) and the refractive index being related to the temperature. The following relationship gives the wavelength shift dependency on strain and temperature,

$$\Delta\lambda_B = 2n_{eff}\Lambda \left( \left\{ 1 - \left( \frac{n_{eff}^2}{2} \right) [p_{12} - \nu(p_{11} + p_{12})] \right\} \varepsilon + \left[ \alpha + \frac{\left( \frac{dn_{eff}}{dT} \right)}{n_{eff}} \right] \Delta T \right). \quad [2]$$

Where  $p_{ij}$  are the piezo coefficients and  $\alpha$  is the coefficient of thermal expansion. From this relationship it has been experimentally confirmed that for smf-28 there is a 1-nm shift for approximately every 1000- $\mu\text{e}$  applied to the grating [1, 2]. While a 13-pm shift occurs for approximately every 1°C change in temperature [1, 2]. The main advantage of FBG sensors is

that the sensing is due to the shift in the Bragg wavelength and not the light intensity in the fiber or the losses in the fiber.

Over the years many different methods have been developed for the monitoring of quasi-static strain fields using FBG sensors. The vast majority of these sensing techniques employ the use of broad-band light sources with a bandwidth that is capable of covering the entire operating region. To detect the wavelength shift in FBG peak, it is compared with a filter with the gratings having a spectral width between 0.05 and 0.3-nm. The two methods available to monitor the FBG shift are the use of static measurement methods or the use of a scanning filter [1].

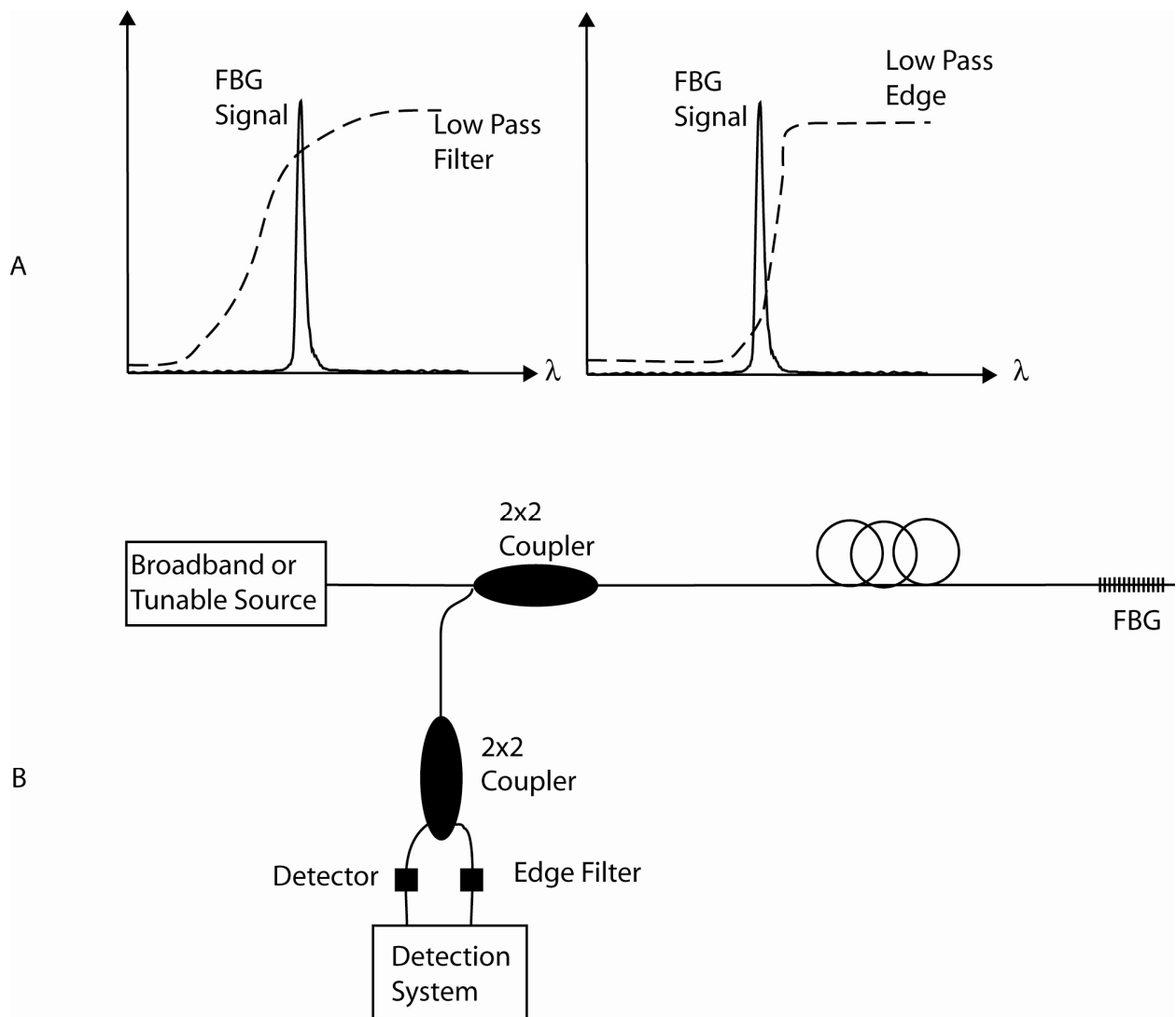


**Figure 12** Examples of low-pass filtering techniques for FBG sensor systems (a) and a sensor system employing a low pass filter technique (b)

The static measurement method includes the use of a broad-band light source and edge filters. These methods observe the intensity of the reflected signal that is changed due to a low-pass filter as depicted in Figure 12b. As the spectrum shifts due to environmental influences more of the reflected signal is filtered out. This allows the determination of the FBG shift by measuring the intensity of the reflected light at the receiver. However, there are several downsides to this method in that the broad-band method has a limited sensitivity restricted by the slope of the filter and the edge filter has a limited range of operation. In 1992 Melle *et al.* [18] developed a ratiometric method for static filter sensing. This method eliminated the influence of the light source intensity and losses in the system, thus reducing the signal-to-noise ratio. Despite this development the measurement range of the sensing system is still inversely proportional to the resolution of the system. [1, 2]

The most successful FBG sensor systems employ scanning optical filters. These methods have a tunable pass-band filter. The FBG wavelength shifts when environmental changes occur, to detect the FBG peak the filter must be adjusted to keep the overlap between the FBG and the filter peaks to produce the maximum reflected signal and therefore determining the shift. Examples include the Fabry-Perot, FBG and acousto-optic filtering techniques [1].

The Fabry-Perot (FP) filtering technique is used for detecting FBG wavelength shift, specifically in fiber communications systems to remove receiver noise [1, 2]. The benefit of using a FP filter for the sensing system is that it is very stable and easy to use. The FP filter is essentially a band-pass filter that has a Lorentzian line shape with a typical bandwidth of approximately 0.3-nm. Additional benefits include a large operating range (tens of nm) and that they are limited only by their free spectral range, or the distance between the two mirrors. Tuning the filter requires the use of Piezo-Electric (PZT) elements to change the cavity spacing between the two mirrors. The FP filter can be implemented two ways, the tracking method (closed loop) which can only track one grating or the scanning method which allows the use of multiple gratings in series. The tracking method has the FP filter locked on to the resonance peak of one FBG and the control voltage for the PZT is used to obtain the change in wavelength. The scanning method allows for the use of multiple FBGs in the sensing system so long as the gratings don't overlap and lie within the free spectral range of the FP filter. The drawback of

this method is that there is a line-broadening effect in the spectral peak which reduces the resolution of the sensor.

It is possible to detect the wavelength shift of the grating sensor by placing a tunable FBG at the receiver end of the system. The FBG filter is attached to a PZT which allows for the grating to be tuned with an applied voltage. The FBG filter is then wavelength matched to the sensing FBG when the sensor is in equilibrium. Due to the strain shifting the wavelength linearly in an FBG, it is possible to know the shift of the sensor by how much strain is required to be applied to keep the wavelengths of the sensor and receiver constant. An advantage of this technique is that it allows for the use of FBGs in parallel or series and the resolution is only limited by the PZT used on the receiver. Jackson *et al.* [18] was the first group to demonstrate this method by using a reflectometric system (parallel gratings). The most significant drawback of using an FBG filter is that the system requires the use of PZT elements, which drastically increase the cost.

The acousto-optic filtering technique uses a solid state component in which the filtering wavelength is selected by an input RF signal. This method allows for a very large tuning capability, on the order of several microns, that has fast scanning capabilities with a narrow filter bandwidth. The large span is ideal for large grating arrays in which the scan range is only limited by the spectral range of the broad-band source. Using this sensing system also requires very few components and it connects to optical fiber without the use of coupling optics. Parallel sensing can be accomplished with multiple RF signals. The performance of the sensor can be improved by using a smaller filter band-width. Dunphey *et al.* [20] have achieved a resolution less than 1-pm over a 120-nm range with a band-width of 0.2-nm. [1, 2]

Since FBG sensors respond temperature and strain simultaneously it is necessary to be able to discriminate the two from one another. This is impossible to accomplish with the use of only grating and is the most significant limitation to FBG sensors. This does not affect dynamic strain sensing, only quasi-static, because the dynamic method does not use an absolute value for the shift, but rather a phase-shift that has thermal dependencies at lower frequencies than the resonant frequency. Therefore in order to measure both temperature and strain it is necessary to use multiple gratings and have one of them isolated from either temperature or strain. Another method would be to use two different sensor elements that each have different responses to

temperature and strain. Using this method the following matrix method can be used to find strain and temperature,

$$\begin{bmatrix} \Delta\lambda_1 \\ \Delta\lambda_2 \end{bmatrix} = \begin{bmatrix} K_{\varepsilon 1} & K_{T1} \\ K_{\varepsilon 2} & K_{T2} \end{bmatrix} * \begin{bmatrix} \varepsilon \\ T \end{bmatrix}.$$

In order for this approach to work one must employ the use of two different lengths of fiber that have different material properties. Xu *et al.* [21] discovered that different resonant wavelengths have different responses to temperature and strain. Using this method it is possible to determine temperature within  $\pm 5^{\circ}\text{C}$  and  $\pm 10-\mu\text{e}$ . [1, 2]

## 2.4 TRANSVERSE STRAIN SENSOR

Over the past several years there have been several studies on using FBGs to measure transverse strain. Lawrence *et al.* [1] employed the use of polarization maintaining (PM) fiber to measure the transverse components of the strain on a fiber. The gratings were written in stressed induced high-birefringent PM fiber. This fiber consisted of an inner core and cladding that was encompassed by an elliptical stress-applying region. This region was doped with boron during the drawing process; this in turn caused a change in the thermal expansion coefficient. The strong birefringence induced by thermal stress due to different coefficients of thermal expansion between the boron doped section and the rest of the fiber. A schematic of this fiber is given below in Figure 13. The significant birefringence produced a significant separation of the FBGs peaks for the two orthogonal modes and is shown below in Figure 14.

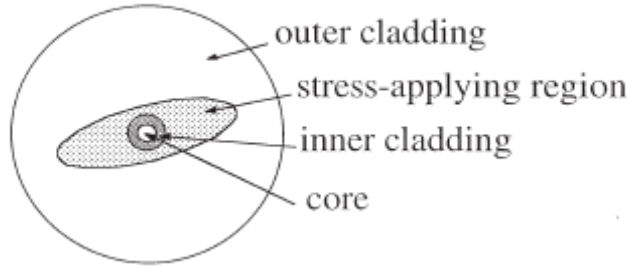


**Figure 13** Schematic of PM fiber used by Lawrence *et al.* [3]

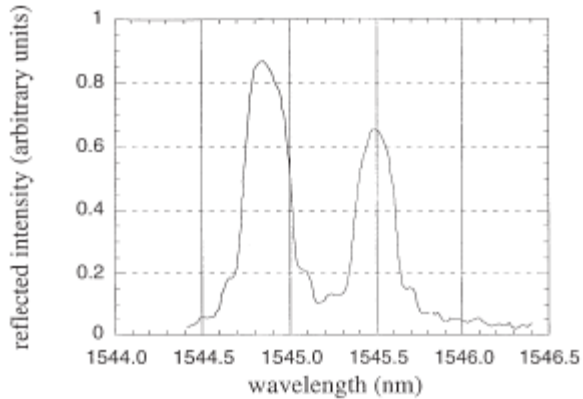


**Figure 14** Reflection spectra of PM fiber used by Lawrence *et al.* [3]

It was shown that the FBG wavelength shift in the reflection spectrum was linear with an applied transverse load. It was also shown that the orientation has a significant impact on the peak shifts. In order to calibrate the sensor they employed the use of finite element analysis to simulate the average strain in the fiber core induced by transverse external loads. The simulated results were used to calculate the K matrix which relates the FBG peak shifts to the strain induced in the fiber core as shown in the following equation,

$$\begin{bmatrix} \Delta\lambda_1 \\ \Delta\lambda_2 \end{bmatrix} = K \begin{bmatrix} \varepsilon_{22} \\ \varepsilon_{33} \end{bmatrix}$$

where  $K$  is a  $2 \times 2$  matrix. Since the wavelength shift is determined experimentally and the strain is determined from the FEA, it is possible to find the  $K$  values through simple matrix manipulation. The calibration process provided good predictions of the FBG peak shifts under an external load. When compared with the experimental results it proved that the FEA gave accurate predictions of the fiber's internal strains.

Ye *et al.* [5] developed an interrogation system to monitor multi-axis strain in bow-tie PM fiber. This system is necessary because in PM fiber the birefringence is small. This could cause problems in discerning the two peaks depending upon the orientation of the fiber. Also, when there is a significant overlap in the two orthogonal modes, the changes in one mode may affect the other. The system had the broad-band light source split through a PM fiber coupler to the length of fiber with the grating. The reflected light would then be passed back through a scanning Fabry-Perot tunable filter. The separation of the two modes allowed them to be recorded independently. What they observed was that the wavelength shift was different for the two polarizations when a load was applied. [5]

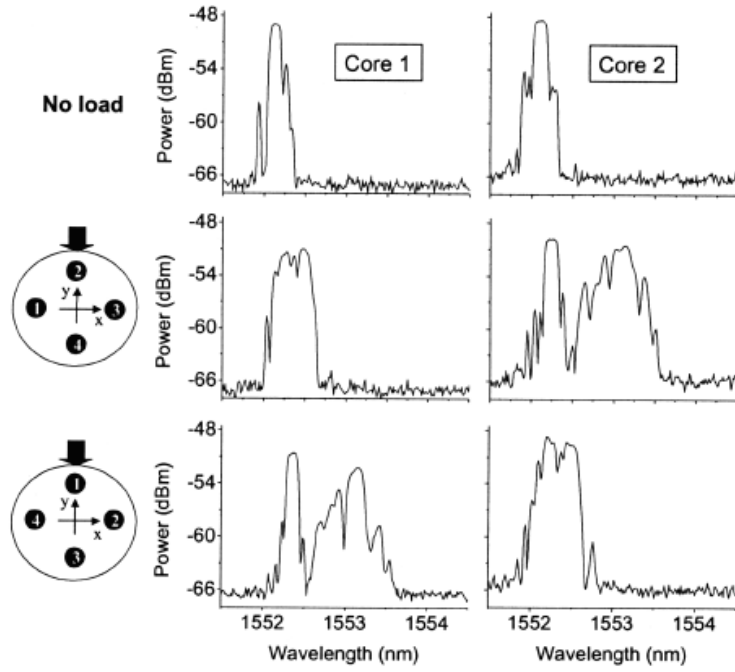


**Figure 15** Reflection spectra from Silva-Lopez *et al.* for two orientations of multi-core fiber [6]

Silva-Lopez *et al.* [6] employed the use of a multi-core fiber in order to measure the applied transverse load on a fiber. The fiber consisted of four cores not in the center of the fiber, they were placed far enough away that there was no coupling between the two cores. When the fiber was applied to stress, the core that was closest to the applied load experienced a large splitting in the spectrum. They proposed a differential calculation from the induced birefringence in the cores at different locations in order to determine the direction and magnitude of the load. The major benefit of this system is that it uses the splitting of the peaks to determine the load and direction, not an absolute value of the wavelength shift, thus making the sensor temperature and axial strain independent. Further, the orientation and the magnitude of applied load can be determined simultaneously. [6]

However, optical fiber is not manufactured for measuring transverse strain. Solid fiber disperses the stress around the fiber's edge as opposed to transferring it into the fiber's core, greatly reducing the transverse strain. In this thesis we used microstructured fiber to increase the fiber's sensitivity to transverse stress. We employed the use of two-hole optical fiber with an off-centered core. The addition of these air holes allowed for an increase in the internal stresses in the fiber core. The major benefit of increasing the fiber's sensitivity to the external load is the ability to eliminate the need for a complex system to discern the two polarizations from one another because the measurement is done solely on the amount of splitting between the two modes as opposed to that magnitude of the light. In order to accurately predict the grating's response we used FEA to determine the average stress in the fiber core. Like with Lawrence *et al.* [3] the use of FEA proved to give accurate results on the grating's response and allows for the creation of application specific fiber.

In this chapter we discussed the necessary background needed in order to understand the principles behind fiber Bragg gratings. This included what a FBG is and different fabrication methods currently employed. Photosensitivity was covered including the underlying principles behind this phenomenon. Then the different methods of using FBGs as sensors were discussed. This covered different configurations of the sensing systems and the methods in which they work. Finally using FBGs as transverse strain sensors was covered. This included the previous work done in this field along with how we propose to advance this field.

## **3.0 THEORY**

### **3.1 STRESS IN A STRUCTURE**

Finite element analysis is the process in which a numerical method applies partial differential equations to describe the behavior of a body [22, 23]. FEA is accomplished by taking the object one wishes to test and meshing the object. Meshing involves dividing the solution domain into many small finite pieces. The behavior of each element is described by the displacement of the elements and the material properties, and all the elements are assembled so that continuity and equilibrium are satisfied between all the adjacent elements. This allows for the determination of a unique solution that is specific to the overall system of linear equations. The setup of the system of equations is sparsely populated, or that most of the coefficients are zero, which shall be covered in more detail later in this section.

In order to understand the principles behind this analysis it is necessary to have a good understanding of stress and how it relates to the FEA. When a body has external forces acting upon it, or when this body exerts a force on its neighboring parts, it is said to be in a state of stress. Taking a volume element situated in a stressed body, there are two types of forces acting upon it. First of these are body forces and are the results of gravity and are proportional to the volume of the element. Second, we have the external forces applied to the surface of the element by the neighboring elements. [22, 23]

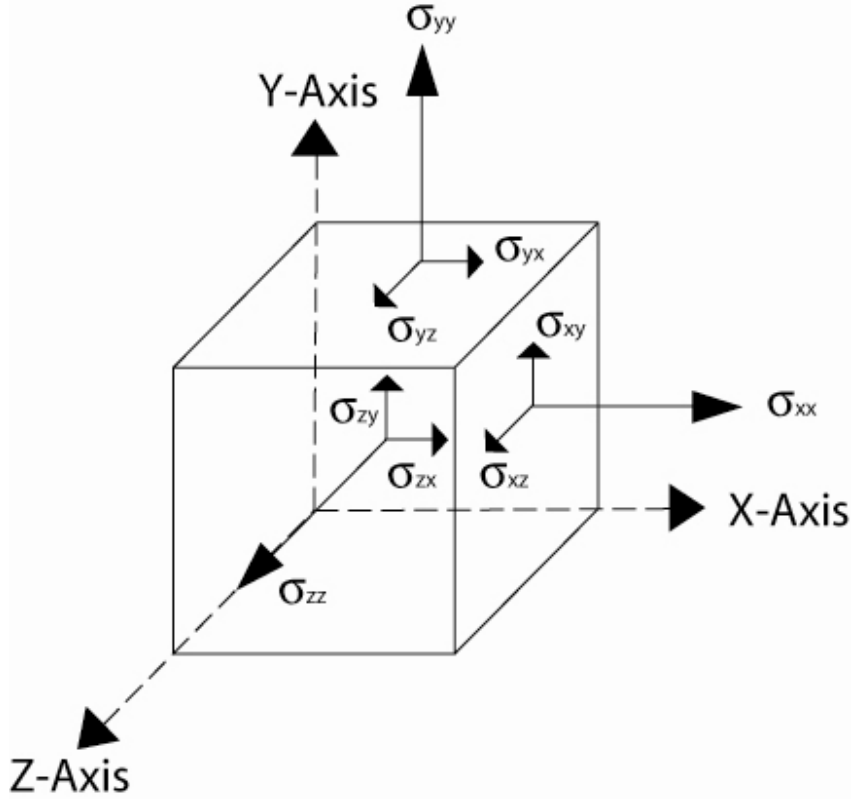


**Figure 16** Three dimensional Cartesian Stress

These forces are proportional to the surface area of the element are defined as stress, as shown in the following equation

$$\sigma \text{ (stress)} = \frac{\text{Force}}{\text{Area}}. \quad (3.1)$$

Now that a definition of stress has been given it is necessary to distinguish the source of the stresses. As it pertains to this thesis, we are only concerned with a homogenous medium. This is when the material properties are homogeneous throughout the body, all parts are in static equilibrium, and there are no body forces or body torques. Taking the cube from Figure 16, a force will be transmitted across each face of the cube from the surrounding material into the internal material. The force across each face is able to be broken up into three components. These consist of the direct stresses ( $\sigma_{xx}$ ,  $\sigma_{yy}$ ,  $\sigma_{zz}$ ) which are either tensile or compressive (depending on the sign of the stress) and are caused by the force normal to the area [22]. The

other components are the shear stresses ( $\sigma_{xy}$ ,  $\sigma_{xz}$ ,  $\sigma_{yz}$ ) and are caused by the shear forces parallel to the area. The stress can then be written as the following 3x3 matrix,

$$\boldsymbol{\sigma} = \begin{bmatrix} \sigma_{xx} & \sigma_{xy} & \sigma_{xz} \\ \sigma_{yx} & \sigma_{yy} & \sigma_{yz} \\ \sigma_{zx} & \sigma_{zy} & \sigma_{zz} \end{bmatrix}. \quad (3.2)$$

Nye [22] states that for equilibrium to take place when no stress is present the sum of the stresses in one direction must equal zero. In order for this to be true then symmetry must hold for the stress matrix and therefore  $\sigma_{xy}=\sigma_{yx}$  or for the general case,

$$\sigma_{ij} = \sigma_{ji}. \quad (3.3)$$

Where the i and j terms are the normal and parallel components of the stress, respectively. This in turn allows for the stress matrix to be rewritten as,

$$\boldsymbol{\sigma} = \begin{bmatrix} \sigma_1 & \sigma_6 & \sigma_5 \\ \sigma_6 & \sigma_2 & \sigma_4 \\ \sigma_5 & \sigma_4 & \sigma_3 \end{bmatrix}. \quad (3.4)$$

This form of the matrix then allows the stress matrix to be written in the following 6x1 matrix,

$$[\boldsymbol{\sigma}] = \begin{bmatrix} \sigma_{xx} \\ \sigma_{yy} \\ \sigma_{zz} \\ \sigma_{yz} \\ \sigma_{xz} \\ \sigma_{xy} \end{bmatrix} = \begin{bmatrix} \sigma_1 \\ \sigma_2 \\ \sigma_3 \\ \sigma_4 \\ \sigma_5 \\ \sigma_6 \end{bmatrix}. \quad (3.5)$$

Likewise, the strain can also be reduced down into the following 3x3 matrix

$$\boldsymbol{\varepsilon}_{ij} = \begin{bmatrix} \varepsilon_{xx} & \varepsilon_{xy} & \varepsilon_{xz} \\ \varepsilon_{yx} & \varepsilon_{yy} & \varepsilon_{yz} \\ \varepsilon_{zx} & \varepsilon_{zy} & \varepsilon_{zz} \end{bmatrix} = \begin{bmatrix} \varepsilon_1 & \frac{1}{2}\varepsilon_6 & \frac{1}{2}\varepsilon_5 \\ \frac{1}{2}\varepsilon_6 & \varepsilon_2 & \frac{1}{2}\varepsilon_4 \\ \frac{1}{2}\varepsilon_5 & \frac{1}{2}\varepsilon_4 & \varepsilon_3 \end{bmatrix}. \quad (3.6)$$

This matrix can then be transformed into the following 6x1 matrix

$$[\varepsilon] = \begin{bmatrix} \varepsilon_{xx} \\ \varepsilon_{yy} \\ \varepsilon_{zz} \\ \varepsilon_{yz} \\ \varepsilon_{xz} \\ \varepsilon_{xy} \end{bmatrix} = \begin{bmatrix} \varepsilon_1 \\ \varepsilon_2 \\ \varepsilon_3 \\ \frac{1}{2}\varepsilon_4 \\ \frac{1}{2}\varepsilon_5 \\ \frac{1}{2}\varepsilon_6 \end{bmatrix}. \quad (3.7)$$

When a solid body is subjected to an applied stress it changes shape. As long as this change is below the elastic limit the body will return to its original shape when the stress is removed. Hooke's Law states that for small stresses the strain is directly proportional to the magnitude of the applied stress, and is given by the following equation,

$$\varepsilon_{ij} = s_{ijkl} \sigma_{kl}. \quad (3.8)$$

This form gives that there are eighty-one  $s_{ijkl}$  coefficients [22]. However, remembering that stress is symmetrical (given from equation 3.3). This in turn would require the following condition to hold,

$$s_{ijkl} = s_{jilk}, \quad (3.9)$$

and is reduced down into a 6x6 matrix with thirty-six independent coefficients.

The elasticity 6x6 matrix for an isotropic material can be determined from the following table reproduced from Nye [22],

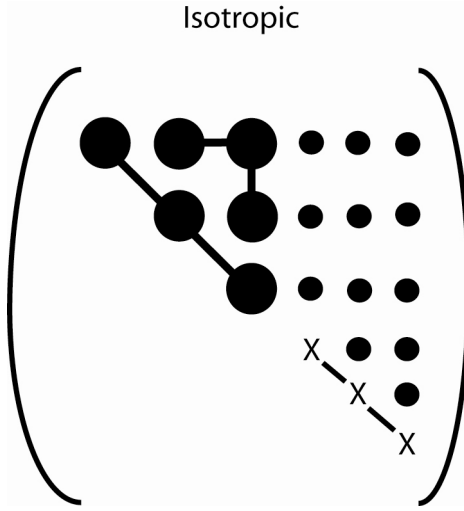


**Figure 17** Isotropic crystal Matrix

Where the small dots are equal to zero, large dots are non-zero components and are equal when connected via a solid line and the X's are equal to  $2(s_{11}-s_{12})$ .

The strain can be found using the following relationship

$$[\varepsilon] = [s]^* [\sigma]. \quad (3.10)$$

When the matrix multiplication is worked out the following equations are obtained,

$$\varepsilon_1 = s_{11}\sigma_1 + s_{12}\sigma_2 + s_{12}\sigma_3 \quad (3.11)$$

$$\varepsilon_2 = s_{12}\sigma_1 + s_{11}\sigma_2 + s_{12}\sigma_3 \quad (3.12)$$

$$\varepsilon_3 = s_{12}\sigma_1 + s_{12}\sigma_2 + s_{11}\sigma_3 \quad (3.13)$$

$$\varepsilon_4 = 2(s_{11} - s_{12})\sigma_4 \quad (3.14)$$

$$\varepsilon_5 = 2(s_{11} - s_{12})\sigma_5 \quad (3.15)$$

$$\varepsilon_6 = 2(s_{11} - s_{12})\sigma_6. \quad (3.16)$$

In elasticity textbooks [23] the strain equations are commonly written as the following equations

$$\varepsilon_1 = \varepsilon_{xx} = \frac{1}{E} [\sigma_{xx} - \nu(\sigma_{yy} + \sigma_{zz})] + \alpha(\Delta T) \quad (3.17A)$$

$$\varepsilon_2 = \varepsilon_{yy} = \frac{1}{E} [\sigma_{yy} - \nu(\sigma_{xx} + \sigma_{zz})] + \alpha(\Delta T) \quad (3.17B)$$

$$\varepsilon_3 = \varepsilon_{zz} = \frac{1}{E} [\sigma_{zz} - \nu(\sigma_{xx} + \sigma_{yy})] + \alpha(\Delta T) \quad (3.17C)$$

$$\varepsilon_6 = 2\varepsilon_{xy} = \frac{1}{G} \sigma_{xy} \quad (3.17D)$$

$$\varepsilon_5 = 2\varepsilon_{xz} = \frac{1}{G} \sigma_{xz} \quad (3.17E)$$

$$\varepsilon_4 = 2\varepsilon_{yz} = \frac{1}{G} \sigma_{yz} \quad (3.17F)$$

with E being Young's modulus (N/m<sup>2</sup>), v is Poisson's ratio, G is the shear modulus (N/m<sup>2</sup>). Comparing the coefficients we obtain the following

$$s_{11} = \frac{1}{E} \quad s_{12} = \frac{-\nu}{E} \quad 2(s_{11} - s_{12}) = \frac{1}{G}$$

and therefore allows us to define G as

$$G = \frac{E}{2(1+\nu)}.$$

With  $\alpha$  being the coefficient of thermal expansion (per °C) and  $\Delta T$  is the temperature change from the reference value (°C). As it applies to this thesis, the thermal terms can be neglected due to all work being done at room temperature with negligible change in temperature in the fiber.

The stress-strain relationship equations can be manipulated so that the stress component is on the left hand side of the equation and is commonly referred to as the material constitutive equation and is as follows

$$[\sigma] = [D]^* [\varepsilon] \quad (3.17)$$

where [D] is the material property matrix and is the inverse of the elasticity matrix,

$$s^{-1} = D.$$

For many cases it is possible to reduce a three-dimensional problem to a two-dimensional problem where only the X-Y plane is modeled. There are two methods in doing so, with different considerations made towards the Z-plane. The first of these is plane stress and this is used for a thin part in the Z-direction where the stress is neglected ( $\sigma_{zz}=0$ ). The other is plane strain and is used to define thick models in the Z-direction where the strain is neglected but the stress is not ( $\varepsilon_{zz}=0, \sigma_{zz}\neq0$ ). In this thesis, we are concerned with the plain strain assumption in that we can ignore the strain in the Z-direction but the stress is a required value needed to theoretically determine the peak splitting. [22]

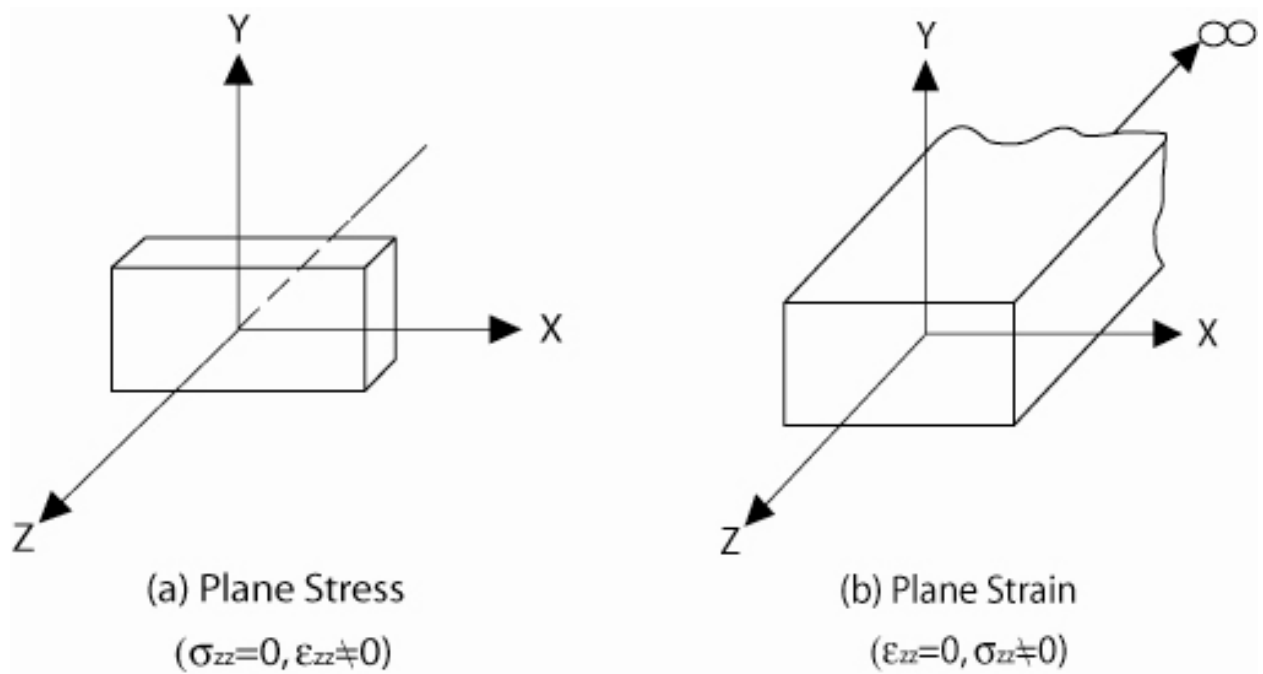


**Figure 18** Two dimensional plan stress and plane strain problems

Using the plain strain approximation and setting equation 3.17C to zero the following relationship is obtained

$$\sigma_{zz} = \nu(\sigma_{xx} + \sigma_{yy})$$

this converts the Hooke's law expression given in equation 3.18 to

$$\begin{bmatrix} \varepsilon_{xx} \\ \varepsilon_{yy} \\ \varepsilon_{xy} \end{bmatrix} = \begin{bmatrix} \frac{1-\nu^2}{E} & -\nu(1+\nu) & 0 \\ -\nu(1+\nu) & \frac{1-\nu^2}{E} & 0 \\ 0 & 0 & \frac{1+\nu}{E} \end{bmatrix} * \begin{bmatrix} \sigma_{xx} \\ \sigma_{yy} \\ \sigma_{xy} \end{bmatrix} \quad (3.19)$$

Using the previous relationship for manipulating the stress term onto the left-hand side of the equation the material property matrix (for plain strain) can be defined as

$$[D] = \frac{E}{(1-2\nu)(1+\nu)} \begin{bmatrix} 1-\nu & \nu & 0 \\ \nu & 1-\nu & 0 \\ 0 & 0 & 1-2\nu \end{bmatrix}$$

It is now desirable to determine how the displacements are related to the elements and their nodes in a meshed network. For simplicity we will only discuss a three-node triangular element here, because it is widely used in FEA. It is possible to relate the following principles to an element with more nodes.

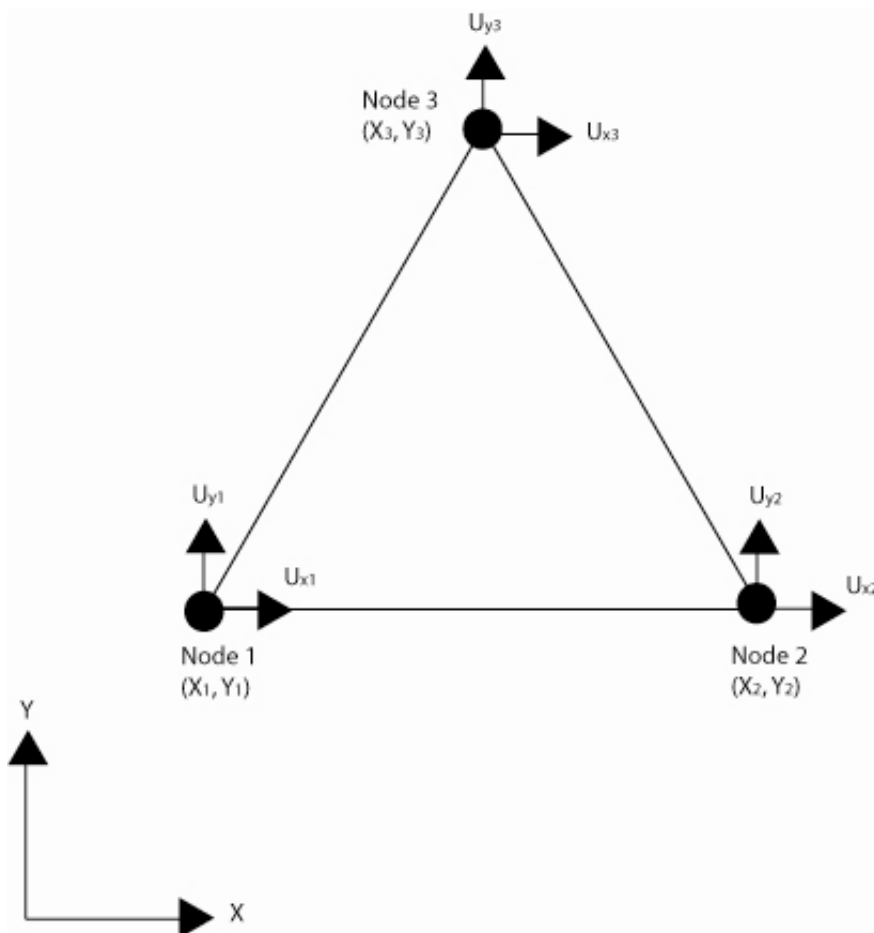


**Figure 19** Two-dimensional triangular three-node element

For the element, it is necessary to know the displacement of the nodes in both the X and the Y-directions. We begin by assuming a linear variation in the displacement over each of the elements, which allows an expression in terms of X and Y to be developed [23],

$$u_x(x, y) = C_1 + C_2x + C_3y \quad (3.20A)$$

$$u_y(x, y) = C_4 + C_5x + C_6y \quad (3.20B)$$

where the C terms are constants that can be expressed in terms of the nodal coordinates. Therefore the overall displacement matrix can be written as

$$\begin{bmatrix} u_{x1} \\ u_{y1} \\ u_{x2} \\ u_{y2} \\ u_{x3} \\ u_{y3} \end{bmatrix} = \begin{bmatrix} 1 & x_1 & y_1 & 0 & 0 & 0 \\ 0 & 0 & 0 & 1 & x_1 & y_1 \\ 1 & x_2 & y_2 & 0 & 0 & 0 \\ 0 & 0 & 0 & 1 & x_2 & y_2 \\ 1 & x_3 & y_3 & 0 & 0 & 0 \\ 0 & 0 & 0 & 1 & x_3 & y_3 \end{bmatrix} * \begin{bmatrix} C_1 \\ C_2 \\ C_3 \\ C_4 \\ C_5 \\ C_6 \end{bmatrix}$$

This equation can be abbreviated to

$$[u_e] = [A]*[C] \quad (3.21)$$

thus relating the displacement vector ( $[u_e]$ ), the coordinate matrix ( $[A]$ ) and the constant vector ( $[C]$ ).

It is possible to relate the strain in the element to the displacement and is given by the following relationships

$$\varepsilon_{xx} = \frac{\partial u_x}{\partial x} = C_2$$

$$\varepsilon_{yy} = \frac{\partial u_y}{\partial y} = C_6$$

$$\varepsilon_{xy} = \frac{\partial u_x}{\partial y} + \frac{\partial u_y}{\partial x} = C_3 + C_5$$

This allows the strain vector to be written as

$$[\varepsilon] = \begin{bmatrix} \varepsilon_{xx} \\ \varepsilon_{yy} \\ \varepsilon_{xy} \end{bmatrix} = \begin{bmatrix} 0 & 1 & 0 & 0 & 0 & 0 \\ 0 & 0 & 0 & 0 & 0 & 1 \\ 0 & 0 & 1 & 0 & 1 & 0 \end{bmatrix} * \begin{bmatrix} C_1 \\ C_2 \\ C_3 \\ C_4 \\ C_5 \\ C_6 \end{bmatrix}$$

this reduces to

$$[\varepsilon] = [X]^* [C] \quad (3.22)$$

Recalling the relationship with the stress on the left hand side, the expanded form of the equation becomes

$$[\sigma] = [D]^* [X]^* [C] = [D]^* [X]^* [A^{-1}]^* [u_e]$$

The above approach must also be done for each element in the mesh, causing the system of equations to become larger. Also of note is that increasing the nodes or changing from two-dimensions to three-dimensions rapidly increases the complexity of the equations for the stress [23]. The equations covered in this section are what FEA software packages use to determine the stress and strains in a structure.

### 3.2 BIREFRINGENCE

Light, being an electro-magnetic wave, has two polarizations, the X and Y-direction. This is vital in the appearance of splitting the resonant peak of a FBG. The cause of the splitting is due to artificial (induced) birefringence caused by stress applied to the crystal and is known as the photoelastic effect [22].

The permittivity and dielectric constants are functions of the stress (therefore so is the refractive index) applied to the crystal. A change in a crystal's refractive index due to an applied stress is also due to the photoelastic effect [22]. When a stress is applied to the crystal the refractive index is given by the following expression

$$n = n_o + aE_o + a'\sigma + bE_o^2 + b'\sigma^2 + \dots \quad (3.23)$$

where  $a$ ,  $a'$ ,  $b$ ,  $b'$  are constants,  $E_o$  is the applied electric field and  $\sigma$  is the applied stress. Because we are only concerned with the stress applied to the material equation 3.23 can be reduced to the following first-order equation [22]

$$n = n_o + a'\sigma \quad (3.24)$$

The refractive index of a crystal can be defined by an ellipsoid with its coefficients being the components of the relative dielectric impermeability tensor and can be defined as

$$B_{ij} = \varepsilon_o \frac{\partial E_i}{\partial D_j} = \frac{1}{n_{ij}^2} \quad (i, j = 1, 2, 3), \quad (3.25)$$

therefore the total impermeability tensor is defined as

$$[B] = \begin{bmatrix} B_{11} & B_{12} & B_{13} \\ B_{21} & B_{22} & B_{23} \\ B_{31} & B_{32} & B_{33} \end{bmatrix} = \begin{bmatrix} \frac{1}{n_{11}^2} & \frac{1}{n_{12}^2} & \frac{1}{n_{13}^2} \\ \frac{1}{n_{21}^2} & \frac{1}{n_{22}^2} & \frac{1}{n_{23}^2} \\ \frac{1}{n_{31}^2} & \frac{1}{n_{32}^2} & \frac{1}{n_{33}^2} \end{bmatrix}. \quad (3.26)$$

The refractive index change due to the first-order photoelastic effect is given by

$$\Delta \left( \frac{1}{n_{ij}^2} \right) = \Delta B_{ij} = p_{ijkl} * \varepsilon_{kl} \quad (i, j, k, l = 1, 2, 3),$$

with  $p_{ijkl}$  being a fourth-rank tensor and the inverse of the elasto-optical coefficients giving the photoelastic effect and  $\varepsilon_{kl}$  being the second-rank stress tensor defined in the previous section.

The 6x6 photoelastic tensor defined for an isotropic material in Cartesian coordinates is defined as [4]

$$p_{mn} = \begin{bmatrix} p_{11} & p_{12} & p_{12} & 0 & 0 & 0 \\ p_{12} & p_{11} & p_{12} & 0 & 0 & 0 \\ p_{12} & p_{12} & p_{11} & 0 & 0 & 0 \\ 0 & 0 & 0 & \frac{(p_{11} - p_{12})}{2} & 0 & 0 \\ 0 & 0 & 0 & 0 & \frac{(p_{11} - p_{12})}{2} & 0 \\ 0 & 0 & 0 & 0 & 0 & \frac{(p_{11} - p_{12})}{2} \end{bmatrix}. \quad (3.27)$$

Recalling the second rank strain sensor given in Equation 3.6 and using Nye's [22] notation the following relationship is obtained

$$\Delta \left( \frac{1}{n_m^2} \right) = \Delta B_m = p_{mn} \varepsilon_n \quad (m, n = 1, 2, 3, 4, 5, 6).$$

Therefore the change in the index of refraction can be expressed as [4]

$$\begin{bmatrix} \Delta\left(\frac{1}{n_1^2}\right) \\ \Delta\left(\frac{1}{n_2^2}\right) \\ \Delta\left(\frac{1}{n_3^2}\right) \\ \Delta\left(\frac{1}{n_4^2}\right) \\ \Delta\left(\frac{1}{n_5^2}\right) \\ \Delta\left(\frac{1}{n_6^2}\right) \end{bmatrix} = \begin{bmatrix} p_{11} & p_{12} & p_{12} & 0 & 0 & 0 \\ p_{12} & p_{11} & p_{12} & 0 & 0 & 0 \\ p_{12} & p_{12} & p_{11} & 0 & 0 & 0 \\ 0 & 0 & 0 & \frac{(p_{11} - p_{12})}{2} & 0 & 0 \\ 0 & 0 & 0 & 0 & \frac{(p_{11} - p_{12})}{2} & 0 \\ 0 & 0 & 0 & 0 & 0 & \frac{(p_{11} - p_{12})}{2} \end{bmatrix} * \begin{bmatrix} \varepsilon_1 \\ \varepsilon_2 \\ \varepsilon_3 \\ \varepsilon_4 \\ \varepsilon_5 \\ \varepsilon_6 \end{bmatrix} \quad (3.28)$$

From the above equation, the following relationships for the first-order change in refractive index can be found [4]

$$\begin{aligned} \Delta\left(\frac{1}{n_1^2}\right) &= -2 \frac{\Delta n_1}{n_1^3} = p_{11}\varepsilon_1 + p_{12}(\varepsilon_2 + \varepsilon_3) \\ \Delta\left(\frac{1}{n_2^2}\right) &= -2 \frac{\Delta n_2}{n_2^3} = p_{11}\varepsilon_2 + p_{12}(\varepsilon_1 + \varepsilon_3) \\ \Delta\left(\frac{1}{n_3^2}\right) &= -2 \frac{\Delta n_3}{n_3^3} = p_{11}\varepsilon_3 + p_{12}(\varepsilon_1 + \varepsilon_2) \\ \Delta\left(\frac{1}{n_4^2}\right) &= -2 \frac{\Delta n_4}{n_4^3} = \frac{(p_{11} - p_{12})}{2}\varepsilon_4 \\ \Delta\left(\frac{1}{n_5^2}\right) &= -2 \frac{\Delta n_5}{n_5^3} = \frac{(p_{11} - p_{12})}{2}\varepsilon_5 \\ \Delta\left(\frac{1}{n_6^2}\right) &= -2 \frac{\Delta n_6}{n_6^3} = \frac{(p_{11} - p_{12})}{2}\varepsilon_6 \end{aligned}$$

Remembering the stress-strain relationship, it is possible to produce the change in refractive index for the six components of stress and these are given by [4]

$$\Delta n_x = -\frac{n_1^3}{2E} \{ (p_{11} - 2\nu p_{12})\sigma_x + [(1-\nu)p_{12} - \nu p_{11}] * [\sigma_y + \sigma_z] \} \quad (3.29)$$

$$\Delta n_y = -\frac{n_2^3}{2E} \{ (p_{11} - 2\nu p_{12})\sigma_y + [(1-\nu)p_{12} - \nu p_{11}] * [\sigma_x + \sigma_z] \} \quad (3.30)$$

$$\Delta n_z = -\frac{n_3^3}{2E} \{ (p_{11} - 2\nu p_{12})\sigma_z + [(1-\nu)p_{12} - \nu p_{11}] * [\sigma_x + \sigma_y] \} \quad (3.31)$$

$$\Delta n_{xy} = -\frac{n_6^3}{2E} (p_{11} - p_{12})(1 + \nu) \sigma_{xy} \quad (3.32)$$

$$\Delta n_{xz} = -\frac{n_5^3}{2E} (p_{11} - p_{12})(1 + \nu) \sigma_{xz} \quad (3.33)$$

$$\Delta n_{yz} = -\frac{n_4^3}{2E} (p_{11} - p_{12})(1 + \nu) \sigma_{yz} \quad (3.34)$$

In the absence of shear stresses,  $\sigma_{xy} = \sigma_{yz} = \sigma_{xz}$  and the system is biaxial [22]. For applied normal stress and for propagation along the z-axis the changes in the Bragg wavelengths are governed by changes in  $\Delta n_x$  and  $\Delta n_y$  and are given by [4]

$$\begin{aligned} \Delta \lambda_{B,x} &= -\frac{n_{eff}^3 \Lambda_B}{E} * \{(p_{11} - 2\nu p_{12})\sigma_x + [(1-\nu)p_{12} - \nu p_{11}] * [\sigma_y + \sigma_z]\} + \frac{2n_{eff} \Lambda_B}{E} * \{\sigma_z - \nu[\sigma_x + \sigma_y]\} \\ \Delta \lambda_{B,y} &= -\frac{n_{eff}^3 \Lambda_B}{E} * \{(p_{11} - 2\nu p_{12})\sigma_y + [(1-\nu)p_{12} - \nu p_{11}] * [\sigma_x + \sigma_z]\} + \frac{2n_{eff} \Lambda_B}{E} * \{\sigma_z - \nu[\sigma_x + \sigma_y]\}. \end{aligned}$$

The first term in the equations correspond to the applied transverse stress, while the second terms are the same and arise from the longitudinal strain applied to the fiber. Therefore the second term is able to be ignored when calculating the change in the Bragg wavelength peak-splitting and reduce to [4]

$$\Delta \lambda_{B,x} = -\frac{n_{eff}^3 \Lambda_B}{E} * \{(p_{11} - 2\nu p_{12})\sigma_x + [(1-\nu)p_{12} - \nu p_{11}] * [\sigma_y + \sigma_z]\} \quad (3.35)$$

$$\Delta \lambda_{B,y} = -\frac{n_{eff}^3 \Lambda_B}{E} * \{(p_{11} - 2\nu p_{12})\sigma_y + [(1-\nu)p_{12} - \nu p_{11}] * [\sigma_x + \sigma_z]\}. \quad (3.36)$$

The above derivation was taken from Gafsi and El-Sherif [4] with added details from Nye [22].

The following table gives the necessary values needed for SMF-28 and two-hole fiber, with the effective indices being obtained from RSoft, the grating period from the known grating in our lab and the  $p_{11}$  and  $p_{12}$  from Gafsi and El-Sherif [4].

**Table 1** Fiber Parameters

$n_{eff}$ (SMF-28)	1.441047
$n_{eff}$ (Two-Hole)	1.439001
Grating Period	506.4-nm
$p_{11}$	0.121-m <sup>2</sup> /N
$p_{12}$	0.270-m <sup>2</sup> /N

In this chapter we provided a detailed mathematical background on stress in a structure and birefringence. With this information the reader should be able to understand exactly how it is possible to relate stress in the optical fiber to the induced birefringence and why it is possible to use FEA to accurately simulate the mechanical behavior of the fiber.

## **4.0 ANSYS MODELING**

### **4.1 FIBER MODELS**

#### **4.1.1 SMF-28**

In order to have a base model for comparison, it was necessary to create a model of standard telecommunications fiber (SMF-28). While SMF-28 has a width of 125 $\mu\text{m}$  and a circular core 8 $\mu\text{m}$  wide, for comparison we employed a model of solid fiber that had an outer diameter of 220 $\mu\text{m}$  as does the two-hole fiber. To model the mechanic behavior of silica fiber the following characteristics of silica glass were used as listed in Table 2 [4].

**Table 2** Material Properties of Fused Silica in  $\mu\text{MKS}$  units

Young's Modulus (E)	$74.52*10^3$
Density	$2.201*10^{-15} \text{ Kg}/\mu\text{m}^3$
Poisson's Ratio ( $\nu$ )	0.17

After the fiber model was created, it was necessary to mesh the structure. This was done using the PLANE183 model. This is a two-dimensional model that has 8 nodes, each with two degrees of freedom (X and Y). The model was chosen because it is a higher order 2-D model with quadratic behavior, and is suited for modeling irregular shaped meshes. A 2-D model was used because it is a plain strain model. This is desirable because it reduces the computation time needed in order to solve the system of equations. To precisely model the deformation of the

fiber and the external load a fine mesh was required. A mesh size of 2- $\mu\text{m}$  was used to construct the mesh. This value was chosen to ensure the simulation can be performed in a reasonable amount of time.

In order to model the compression plates, a line was used to represent both the top and bottom plate. Due to the plate's weight not being a factor in the compression of the fiber, an actual plate model was not necessary. After the contacts between the fiber and the "plates" were established it was necessary to apply the load to the fiber. However, because a 2-D model was used, it was necessary to convert the force. This was done by taking the force multiplied by the conversion factor (micron) and then divided by the length.

$$F_{2-D} = \frac{\text{Force} * \mu\text{m}}{\text{length}}$$

Since the model was modeled using  $\mu\text{MKS}$  units the length of the grating (1-cm) needed to be converted into microns (1-cm=1E4- $\mu\text{m}$ ) for the proper length. The force was then applied to both directions of the fiber. After the simulation had completed at a specified load the stresses in the core were needed for the peak-splitting equation. This was carried out by taking the stress ( $\sigma_{x,y,z}$ ) at each node in the core, and then taking the average of the directional stress component to be inserted into the equations 3.35 and 3.36. This was done for several applied loads. Below in Figure 20 is an example of the model used to simulate the solid fiber in ANSYS.

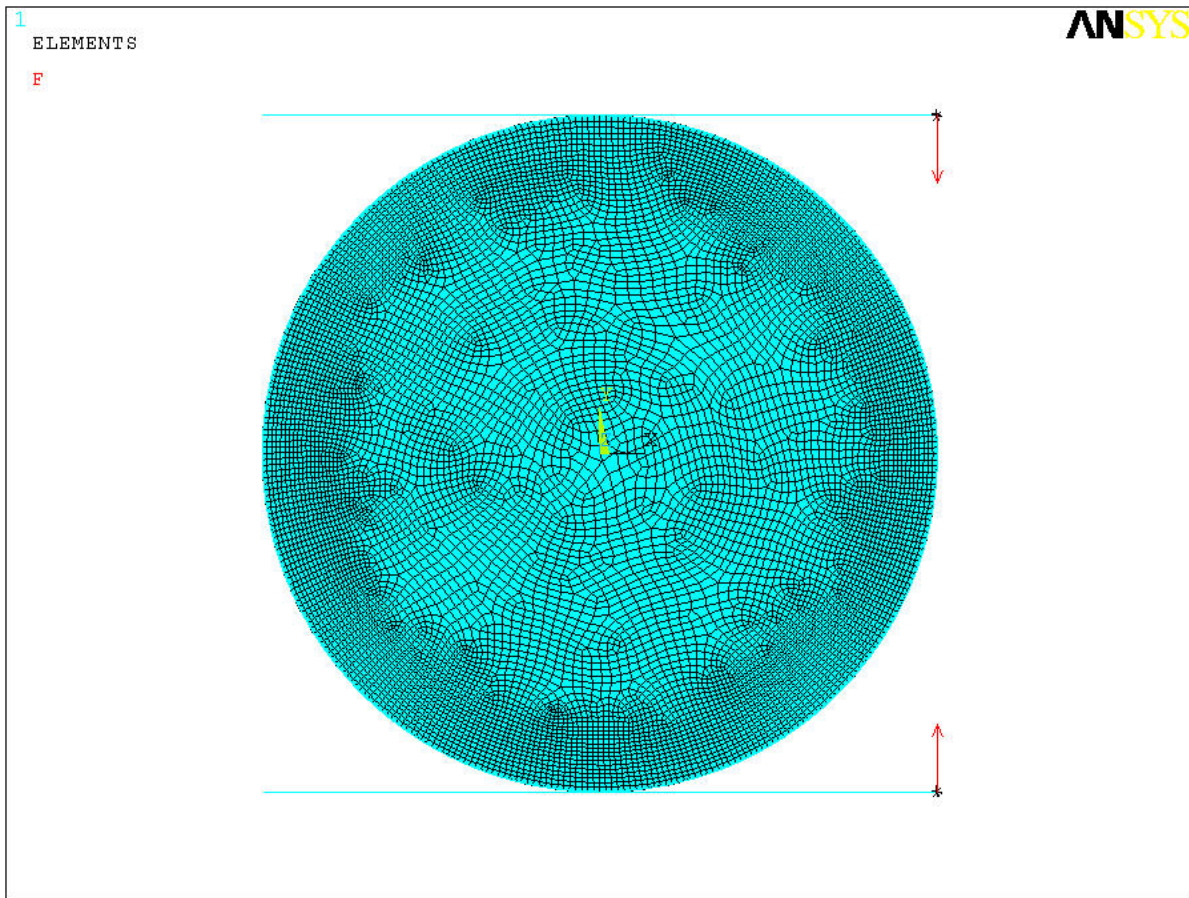


**Figure 20** SMF-28 Simulation Model

#### 4.1.2 Two-Hole Fiber

For the two-hole fiber it was necessary to obtain the characteristics of the fiber in order to make the model. The two-hole fiber had a width of  $220\mu\text{m}$  and each air hole was  $90\mu\text{m}$  wide. The core however was not in the center of the fiber, but was offset towards one of the air holes and was elliptical as opposed to circular. The traits of the fiber can be seen in the cross-sectional photograph below in Figure 21.



**Figure 21** Cross-Section of two-hole fiber

From the photograph of the fiber in Figure 21, the illustration in Figure 22 was made. The two-hole fiber has an elliptical core that is  $4\mu\text{m} \times 10\mu\text{m}$ , offset  $4\mu\text{m}$  from the center, with a spacing of  $16\mu\text{m}$  between the two air holes.

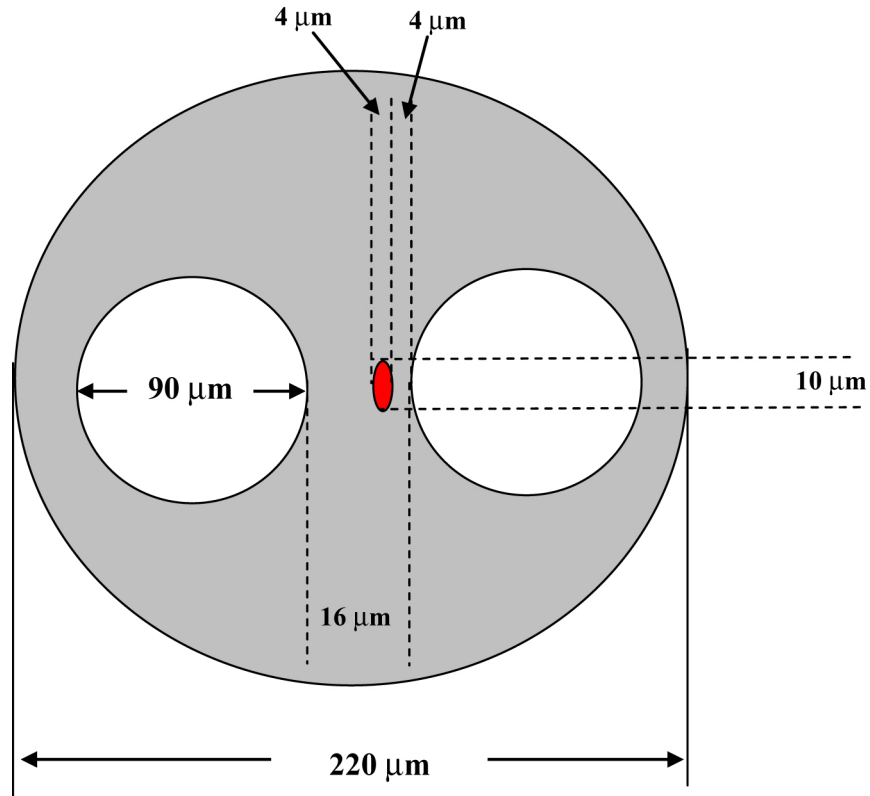


**Figure 22** Illustration of two-hole fiber with dimensions

This illustration is what was used to create the model used in ANSYS for both vertical and horizontal orientation of the air holes. The models were made in accordance with how the solid fiber model was done. The only exception being that now there were air holes placed vertical or horizontal to the applied loads. Figure 23 is the model used for the air holes in the vertical orientation and is given as an example.

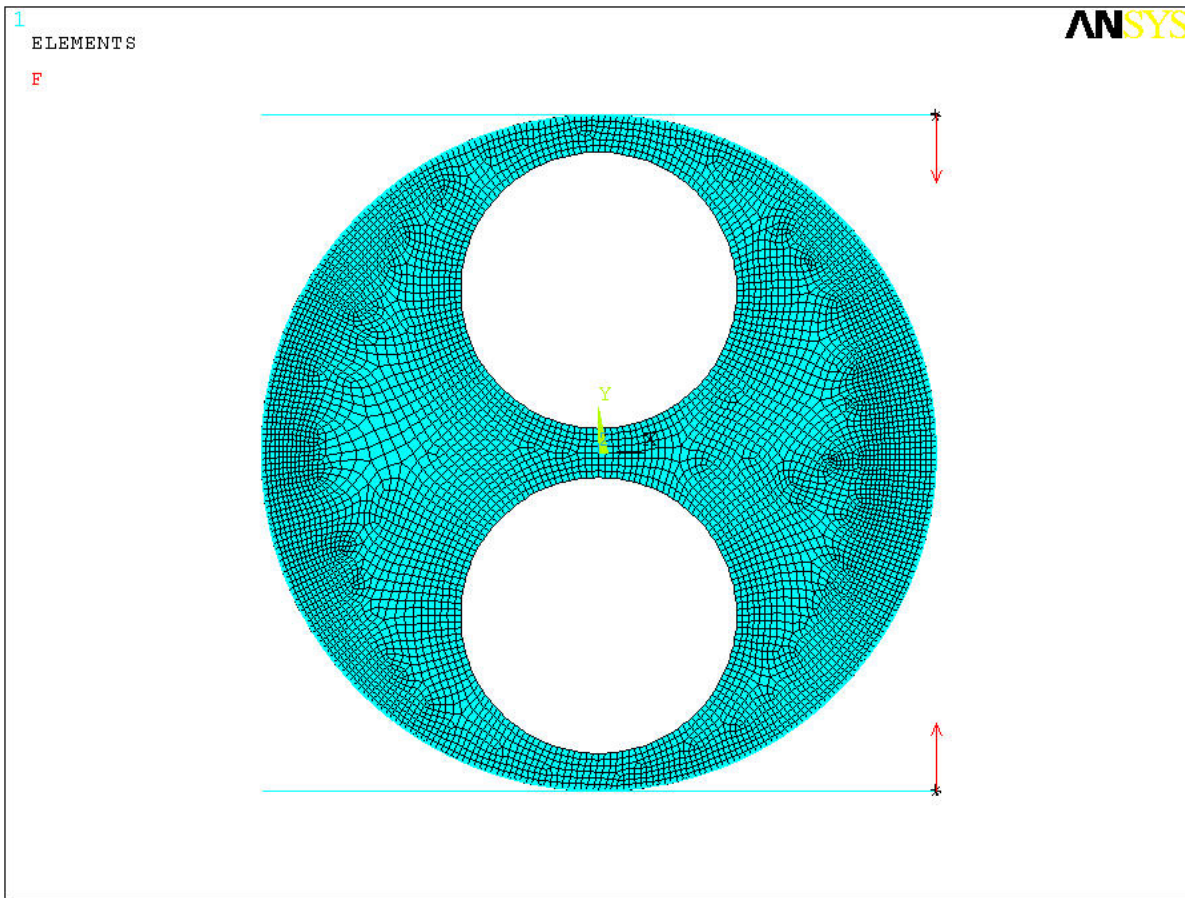


**Figure 23** Two-Hole Fiber Simulation Model, Holes in the Vertical Orientation

## 4.2 ANSYS RESULTS

### 4.2.1 Contour Plots

In the following section the contour plots obtained in ANSYS will be shown. It should be noted that the load applied in each of the Figures is 50-N/cm, and that the units for the stress are in MPa. Also, each Figure was cropped in ANSYS in order to obtain the best representation of the stresses through the fiber.

#### 4.2.1.1 SMF-28

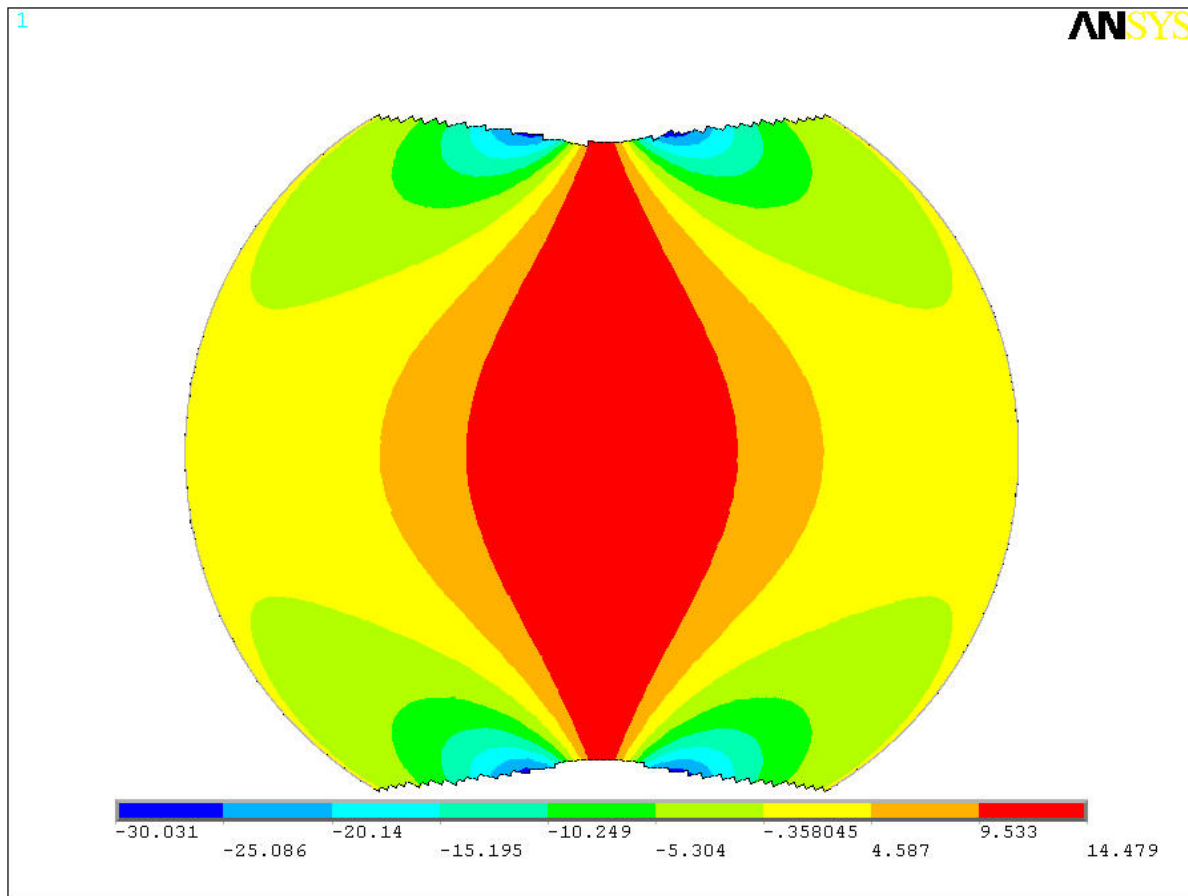


**Figure 24** Stress in the X-direction ( $\sigma_x$ ) for SMF-28

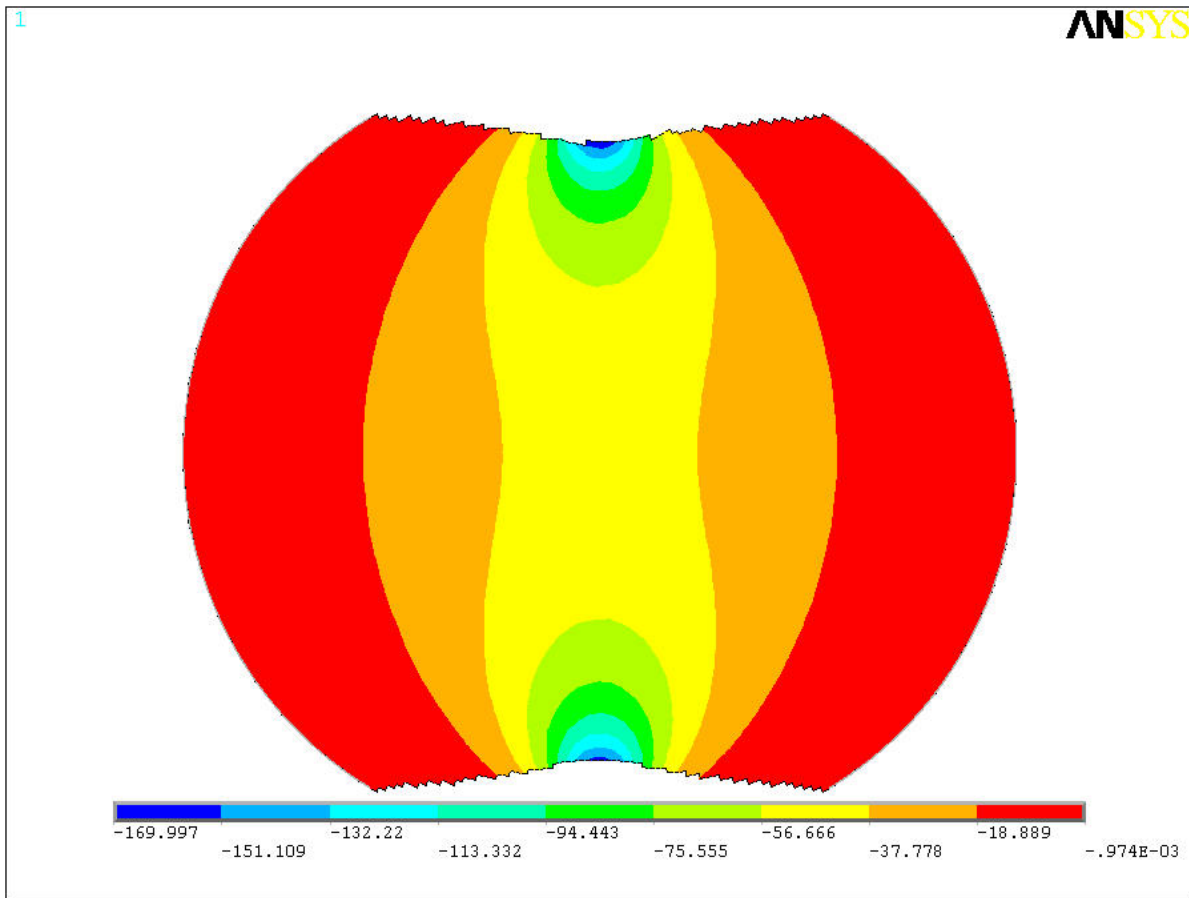


**Figure 25** Stress in the Y-direction ( $\sigma_y$ ) for SMF-28

In Figures 24 and 25 one can see that the stress in the fiber consists of both compression (negative) and tensile (positive) stresses. In the case of the stress in the X-Direction it is seen that the stress is pushing outward from the center in relation to the fiber being compressed between the two plates. In the Y-direction the stress is focused in the center of the fiber, with the stress on the edge being negligible with respect to the stress that is seen in the rest of the fiber. In a solid fiber, when a transverse load is applied vertically to the fiber, the maximum stress takes place at the contact point and vicinity. In the area of the fiber center, the stress is dispersed across the entire fiber due to the increased area of the reaction plane in the fiber center. This is confirmed by a FEA using ANSYS 10.0 shown in Fig. 25. Therefore, the sensitivity of fiber Bragg gratings in the fiber core to transverse stress reduces dramatically. Since the stress is

measured by pressure per unit area, the stress induced in fiber core can be focused by reducing the reaction area in the fiber center.

#### 4.2.1.2 Two-Hole Vertical Orientation

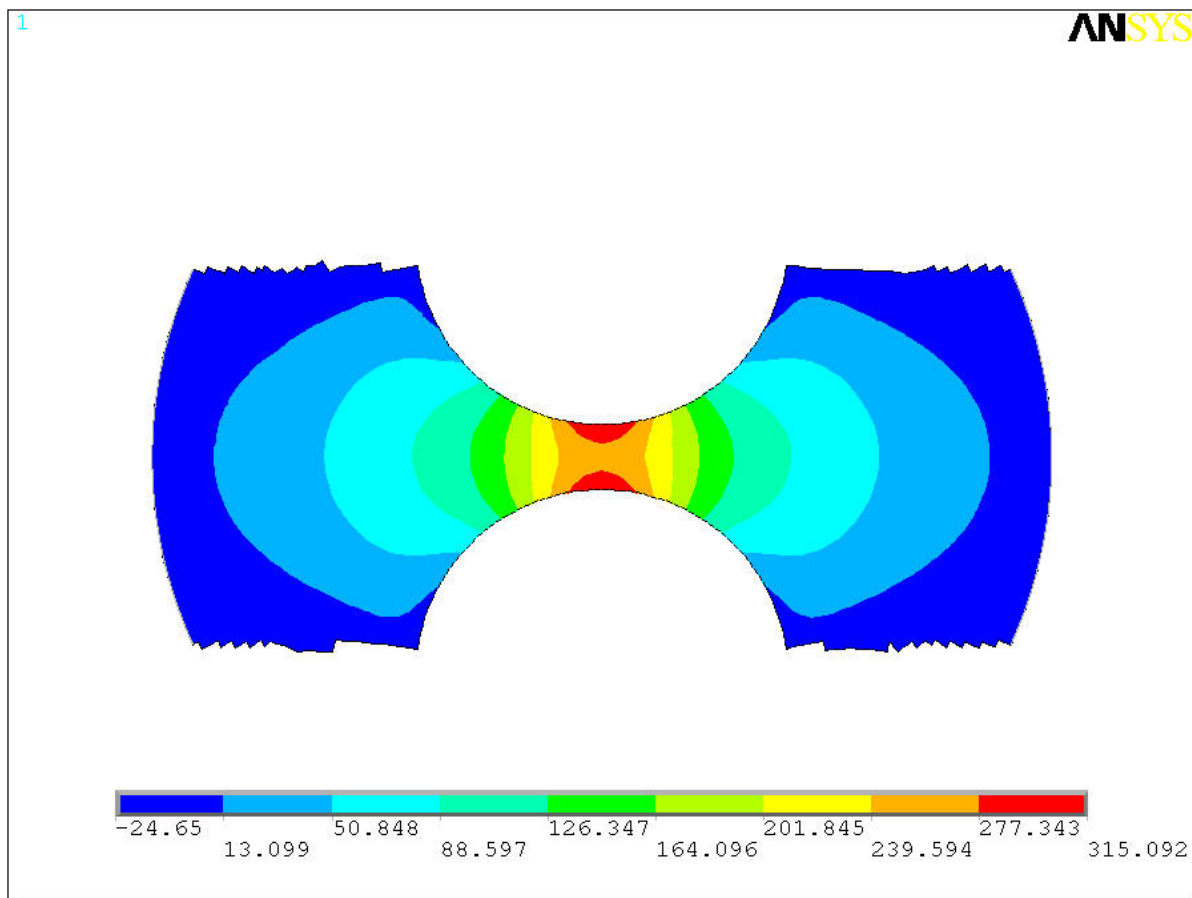


**Figure 26** Stress in the X-direction ( $\sigma_x$ ) for two-hole fiber in the vertical orientation

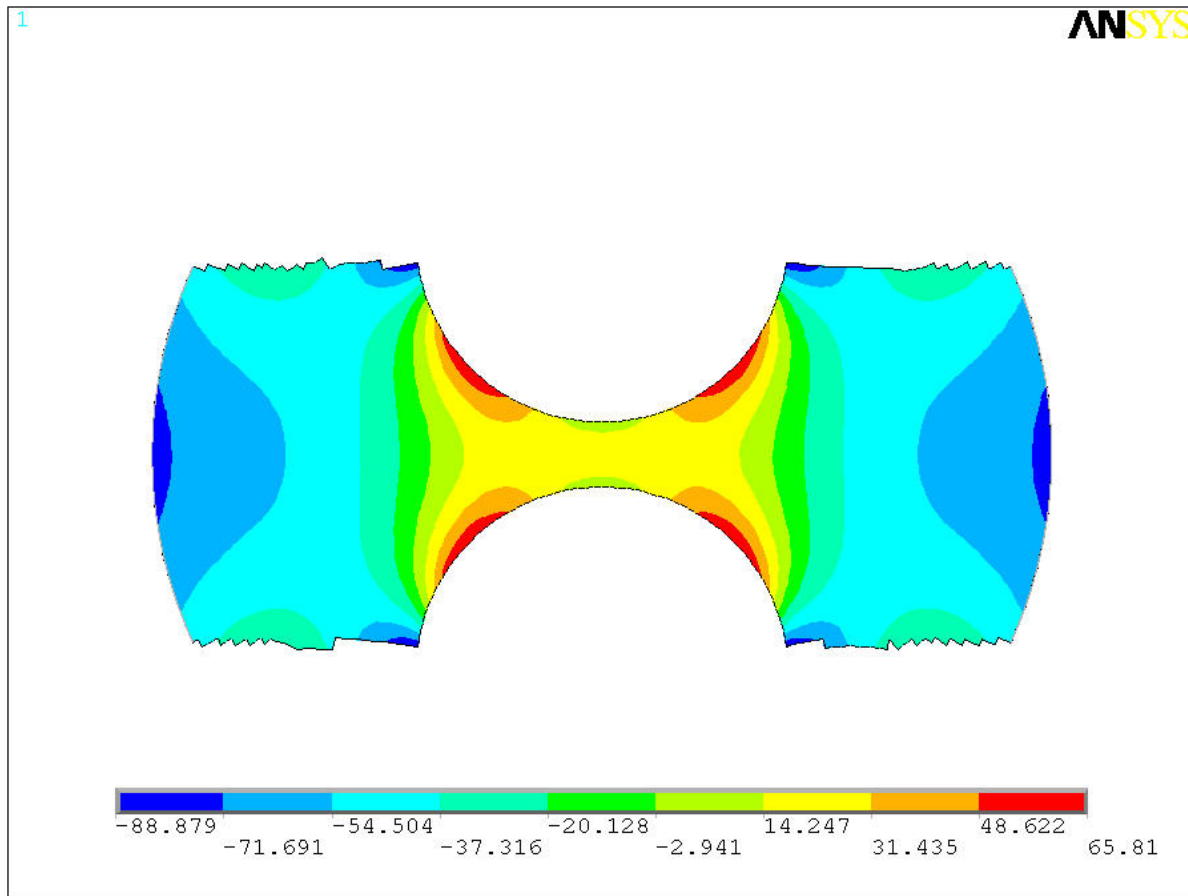


**Figure 27** Stress in the Y-direction ( $\sigma_y$ ) for two-hole fiber in the vertical orientation

When the air holes are in the vertical orientation (parallel to the force) the stress is deflected around the air holes. In the X-direction the stress in the fiber core is entirely tensile stress and is the dominant component of the stress in the fiber's core. The stress in the Y-component is a factor of approximately 20 times less than the X-direction component. The stresses are shown for the X and Y components in Figures 26 and 27, respectively.

#### 4.2.1.3 Two-Hole Horizontal Orientation

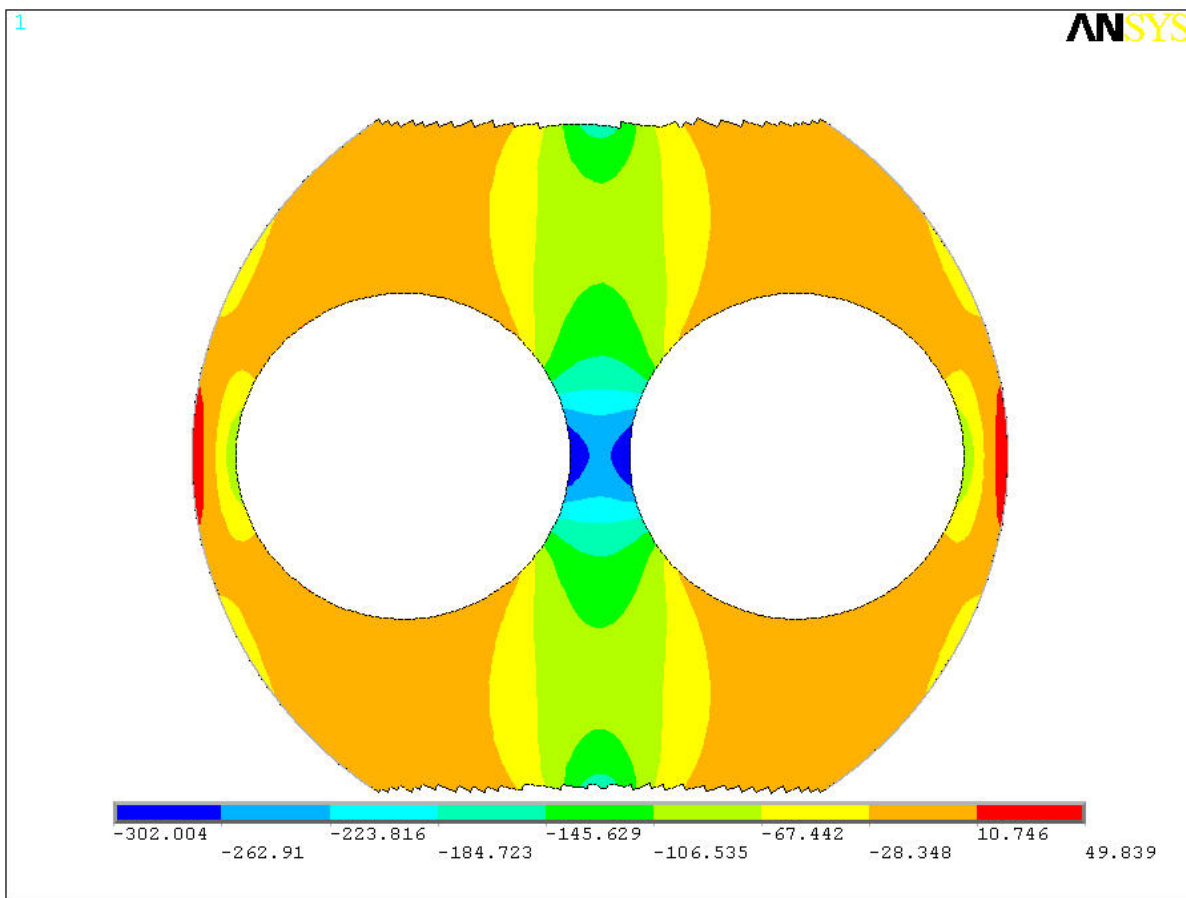


**Figure 28** Stress in the Y-direction ( $\sigma_y$ ) for two-hole fiber in the horizontal orientation

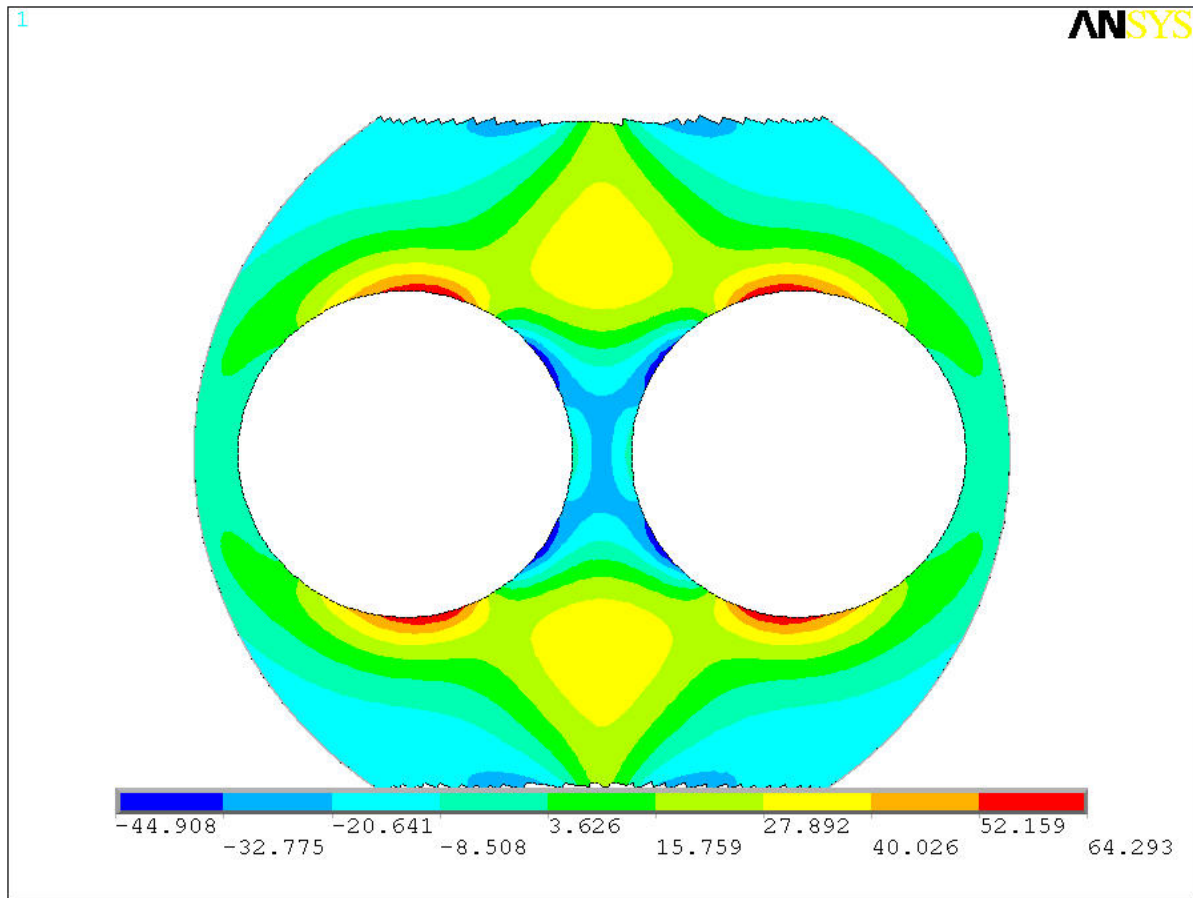


**Figure 29** Stress in the X-direction ( $\sigma_x$ ) for two-hole fiber in the horizontal orientation

In the horizontal orientation the dominant stress in the fiber core is compression stress and is dominated by the Y-directional component of the stress and can be observed in Figure 28. While the X component of the stress depicted in Figure 29 is again approximately 20 times less. In this orientation the air holes act to focus the stress into the fiber core as opposed to deflecting it.

#### 4.2.1.4 45° Rotation

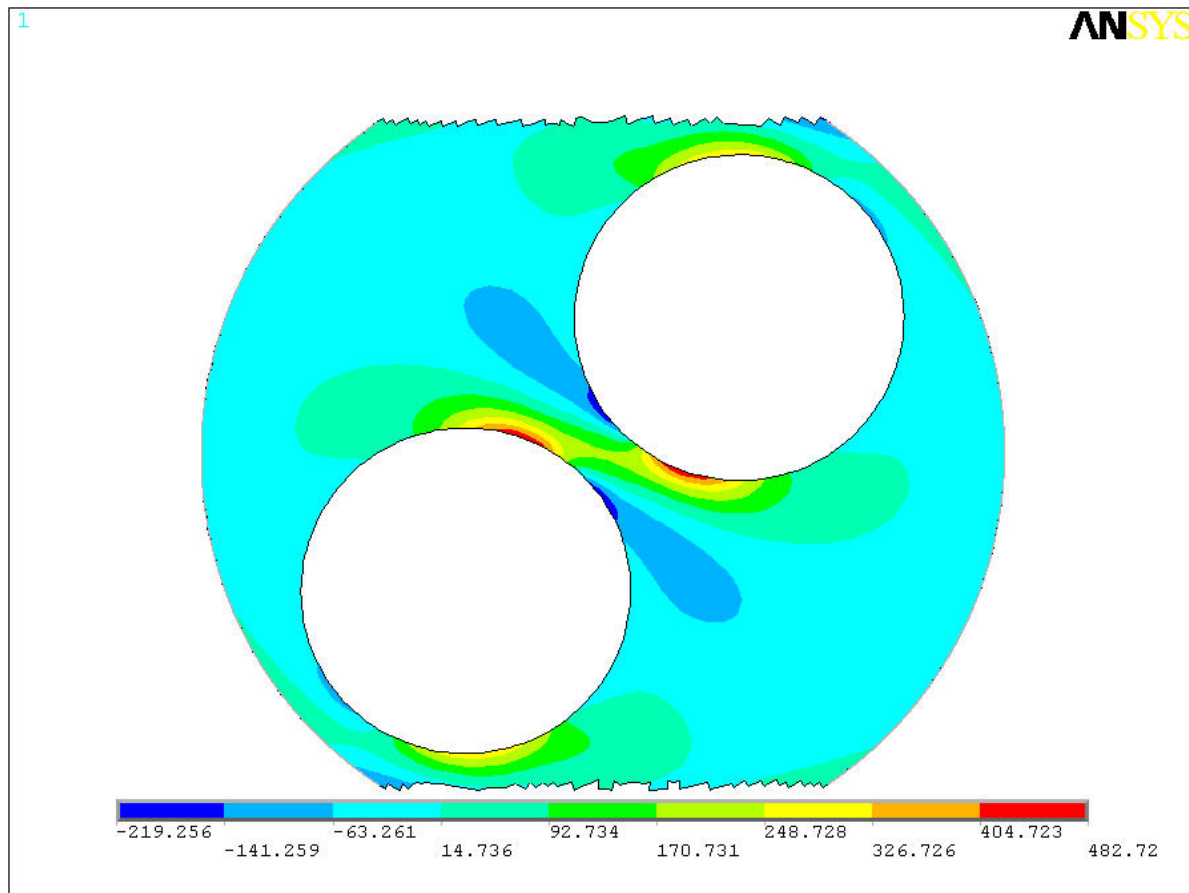


**Figure 30** X-Component ( $\sigma_x$ ) of two-hole fiber rotated 45°

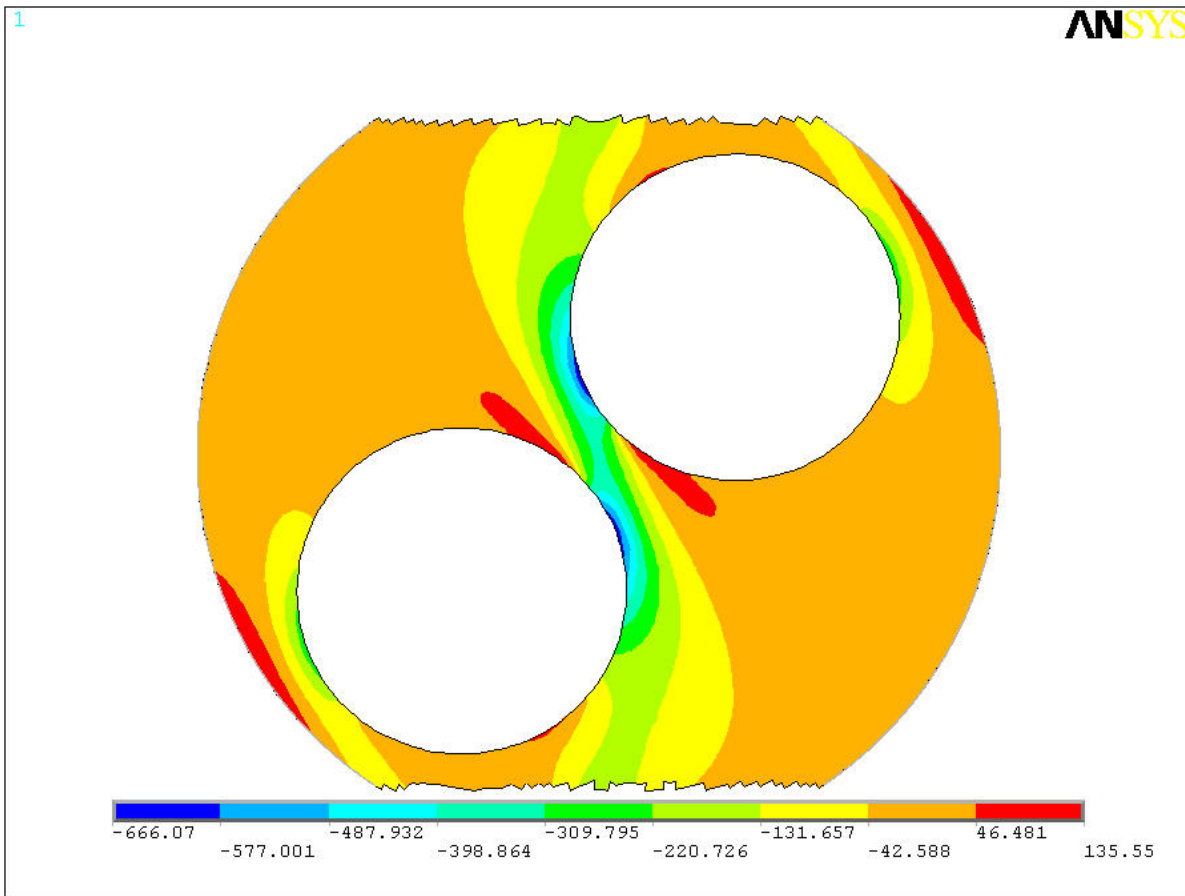


**Figure 31** Y-Component ( $\sigma_y$ ) of two-hole fiber rotated 45°

The above contour plots in Figures 30 and 31 shows the stress in the two-hole fiber when the air-holes have been rotated 45° off axis for the X and Y components of stress, respectively. In this orientation the air-holes no longer entirely deflect the stress as when the air holes are vertical. However, the air-holes also do not completely focus the stress into the fiber's center. What occurs is a combination of both compressive and tensile stress in the fiber's core, which the compressive stress (Y-component) being twice that of the tensile stress (X-Component).

#### 4.2.2 Stress through fiber

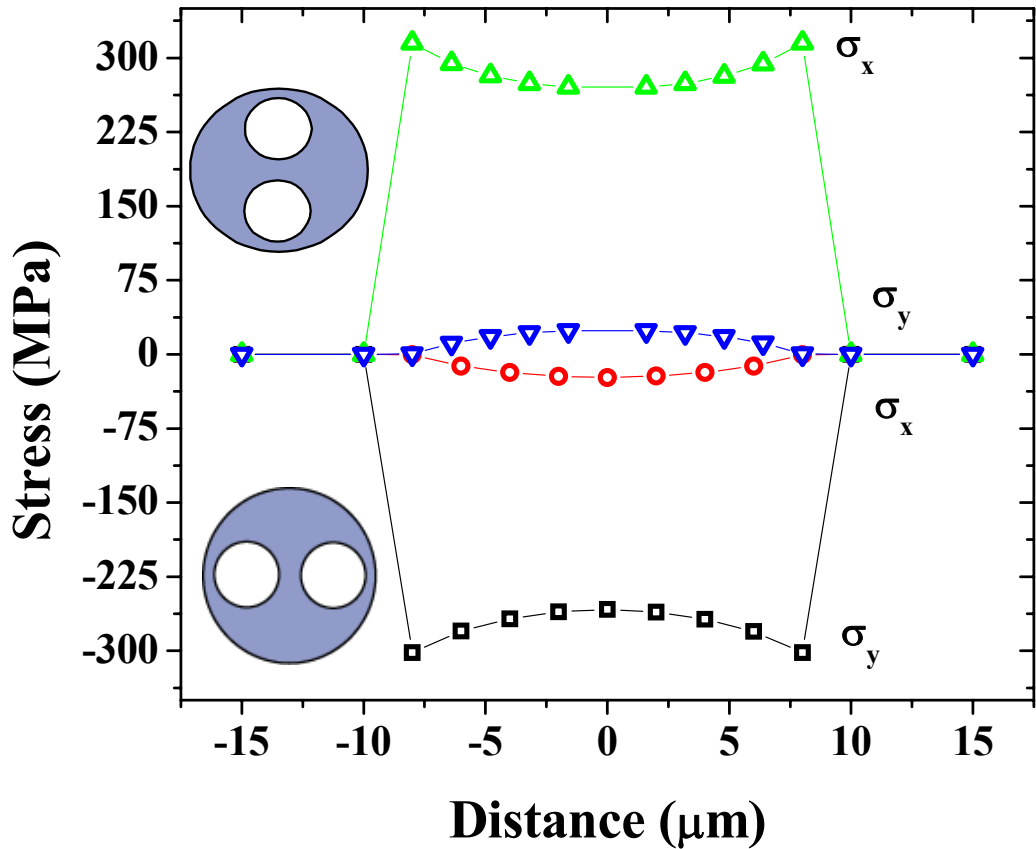


**Figure 32** Stress vs. distance between the air holes in two-hole fiber (F=50-N)

A better example of how the stress reacts between the two air holes based upon the orientation of the fiber is shown in Figure 32 above. This illustrates the dominance of either tensile or compression stress with regards to the air-holes orientation with respect to the applied load. In order to maximize the sensitivity of the FBG sensor the fiber core should be placed at the edge of one of the air-holes.

### 4.2.3 Peak Splitting Plots

#### 4.2.3.1 SMF-28

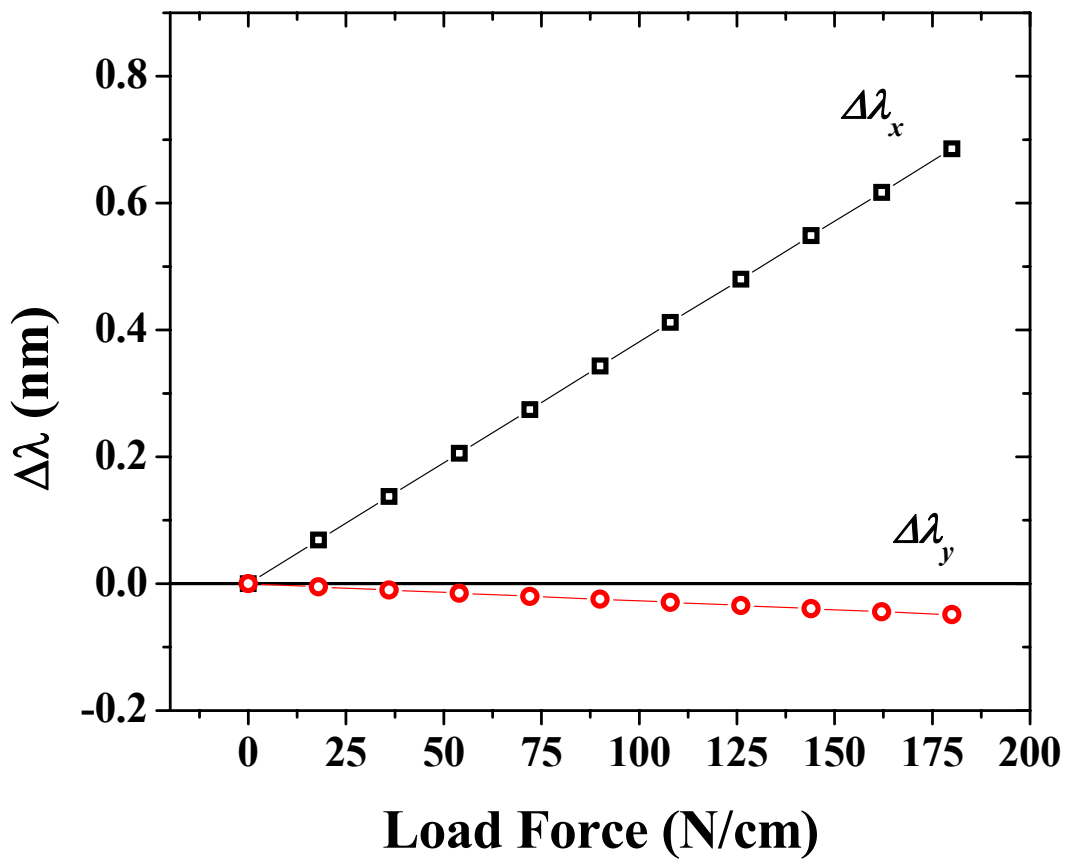
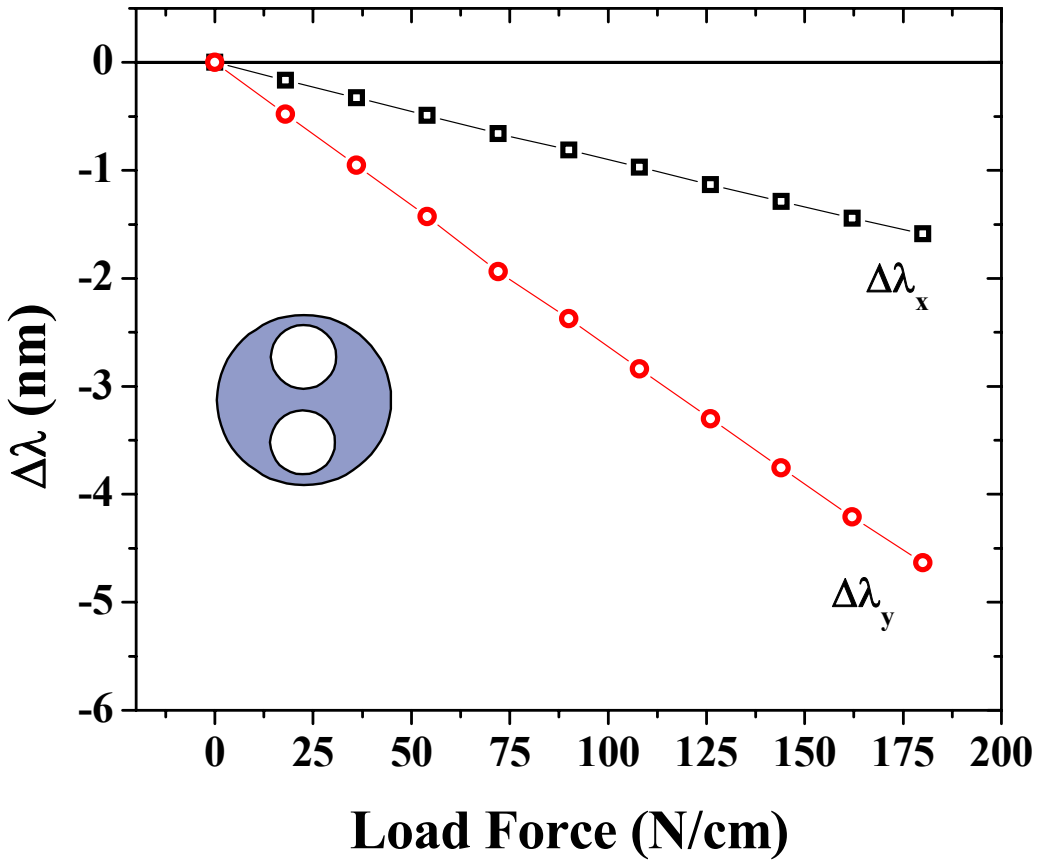


Figure 33 Peak splitting plot for SMF-28

Above in Figure 33 the change in the resonance peak wavelength is plotted vs. the applied load to the grating. Here the polarizations of the light split into two distinct peaks, however the Y-polarization is a factor of seven times less than the X-polarization. While the X-

polarization has a red-shift (positive) the Y-component of the light has a blue-shift (negative) with respect to the initial peak wavelength. The results seen here match that of Gafsi and El-Sherif [4] for SMF-28.

#### 4.2.3.2 Vertical Orientation



**Figure 34** Peak splitting of two-hole fiber in the vertical orientation

In the vertical orientation shown above in Figure 34, the air holes act in deflecting the stress around them, thus causing the stress between the air holes to push outward and be

completely dominated by tensile stress. This in turn causes both polarizations to blue-shift at a greater magnitude than that of SMF-28.

#### 4.2.3.3 Horizontal Orientation

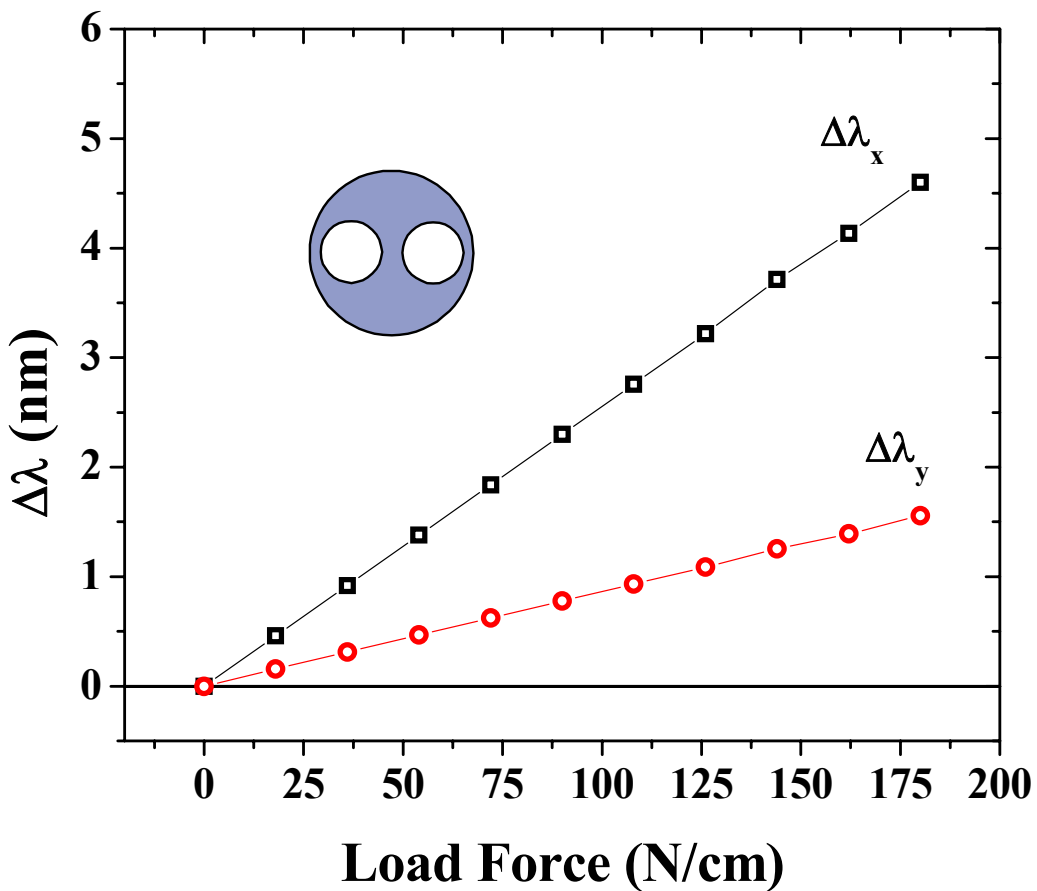


**Figure 35** Peak splitting of two-hole fiber in the horizontal orientation

With the air holes in the horizontal orientation the air holes act to focus the stress between them and into the fiber core. However, in this orientation the stress is dominated by

compression stress which in turn causes a red-shift in both polarizations and can be seen above in Figure 35. This is significant because this shows that depending on the orientation of the air holes, not only is the type of stress different, but more importantly the direction of the spectral response changes. This allows one to determine the direction of the compression with respect to the orientation of the fiber.

#### 4.2.3.4 Splitting at 45 Degree Rotation

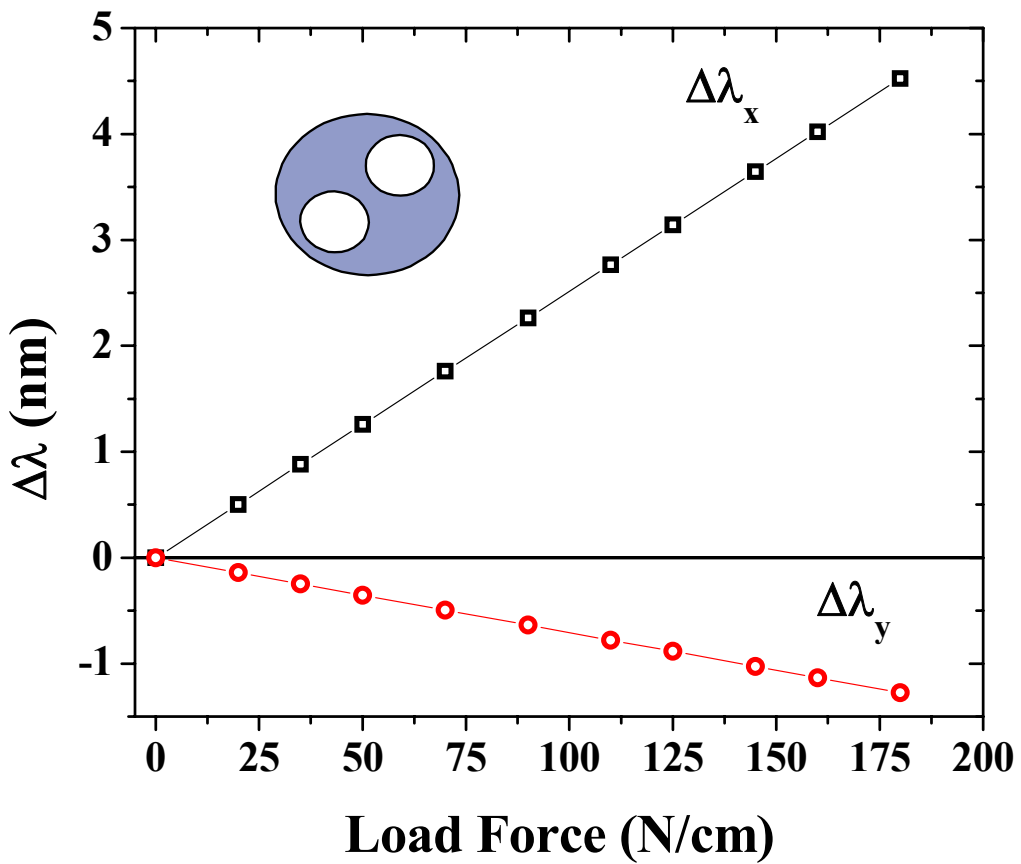


**Figure 36** Peak splitting for two-hole fiber at 45° rotation

When the fiber is rotated so that the air-holes are rotated by  $45^\circ$  the stress is dominated by compressive stress, but also has a significant component of tensile stress as with SMF-28. However, the magnitude of the stress is much larger than that of standard fiber due to the air-holes. This causes a larger spectral shift in which the X-polarization mode has a shift approximately four times as large as the Y-polarization and the spectral shifts are approximately 5 times larger than that of SMF-28 and can be seen above in Figure 36.

#### 4.2.3.5 Splitting as a Function of Rotation

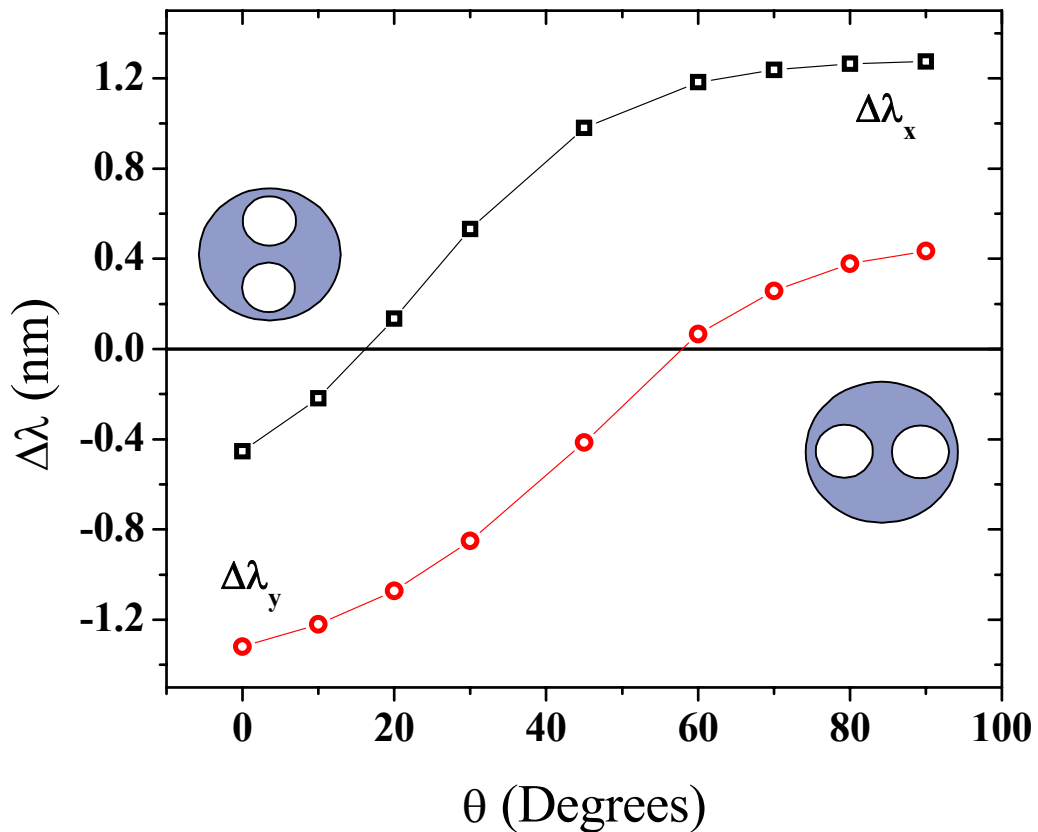


**Figure 37** Peak splitting as a function of rotation ( $F=50\text{-N/cm}$ )

As depicted in Figure 37, the peak splitting follows a sinusoidal response as it moves from vertical ( $\theta=0^\circ$ ) to horizontal ( $\theta=90^\circ$ ) orientation.

This chapter covered everything pertaining to the simulations done employing FEA. The method in which the models were created in ANSYS was given, specifically how converting the 3-D model into the 2-D model that was used. The stress profiles for the SMF-28 and the two-hole fiber are presented. This includes the vertical and horizontal orientations of the two-hole fiber along with the fiber oriented to  $45^\circ$  off-axis. The birefringence plots are given for both fibers including the angular dependency of the two-hole fiber. Our simulations have confirmed that if air-holes are introduced, the sensitivities of the FBG sensors to the transverse stress increases by approximately 20 times more in twin-hole fibers than in solid fibers with the same diameter. The asymmetric air-hole configurations have also produced an orientation sensitive strain sensor for 3-D embedded stress measurement. These simulation results will be compared with experiments in the next chapter.

## **5.0 EXPERIMENT**

### **5.1 FABRICATION AND SETUP**

In order to experimentally verify our simulations two different gratings were needed, one in SMF-28 and another in the two-hole fiber. Both fibers were hydrogen soaked at 1100-psi for 10 days to increase their photosensitivity. 1-cm gratings were inscribed into the gratings using a 248-nm KrF excimer laser and a phase mask. Before the phase mask, the beam was passed through a 1-cm slit with an apodization mask to filter out the additional modes in the spectral peak. The two-hole fiber was aligned in the fabrication setup with the air-holes in the vertical direction. This was done to avoid any deflection of the beam by the air holes. After writing the gratings the fibers were annealed at 100°C for 24 hours in order to out diffuse any remaining hydrogen.

The experimental setup used for the compression required a compression stage that could apply a constant static load that could be measured. This was accomplished by using a screw mechanism for the load, and a load cell beneath the anvil to measure the applied load. This setup is similar to the one employed by Silva-Lopez *et al.* [6]. The setup required two fibers, the fiber under test and a dummy fiber. The dummy fiber was needed to ensure that a constant even load was applied to the fiber. Both fibers were clamped into place and tensioned to the point that they were lying flat upon the anvil. The two-hole fibers required alignment of the air holes in either vertical or horizontal orientation. This was accomplished by using a 20x microscope objective and a CCD camera to observe the orientation. To make things easier a rotation stage, consisting of a fiber chuck and a 360° rotator, was used to rotate the fiber. The test fiber was fusion spliced to SMF-28 that was connected to a circulator (so that we would have reflection spectra as opposed to transmission). To the input end of the circulator an optical spectrum analyzer (OSA) and Er-doped amplified spontaneous broadband source (ASE) were connected.

For the testing several loads were applied to the SMF-28 grating and the two-hole fiber grating with its air holes in both orientations. In order to determine where the peaks were centered a two-peak Gaussian fit was applied to the spectrums. This allowed for a better determination of the peaks, especially when the splitting was very small.

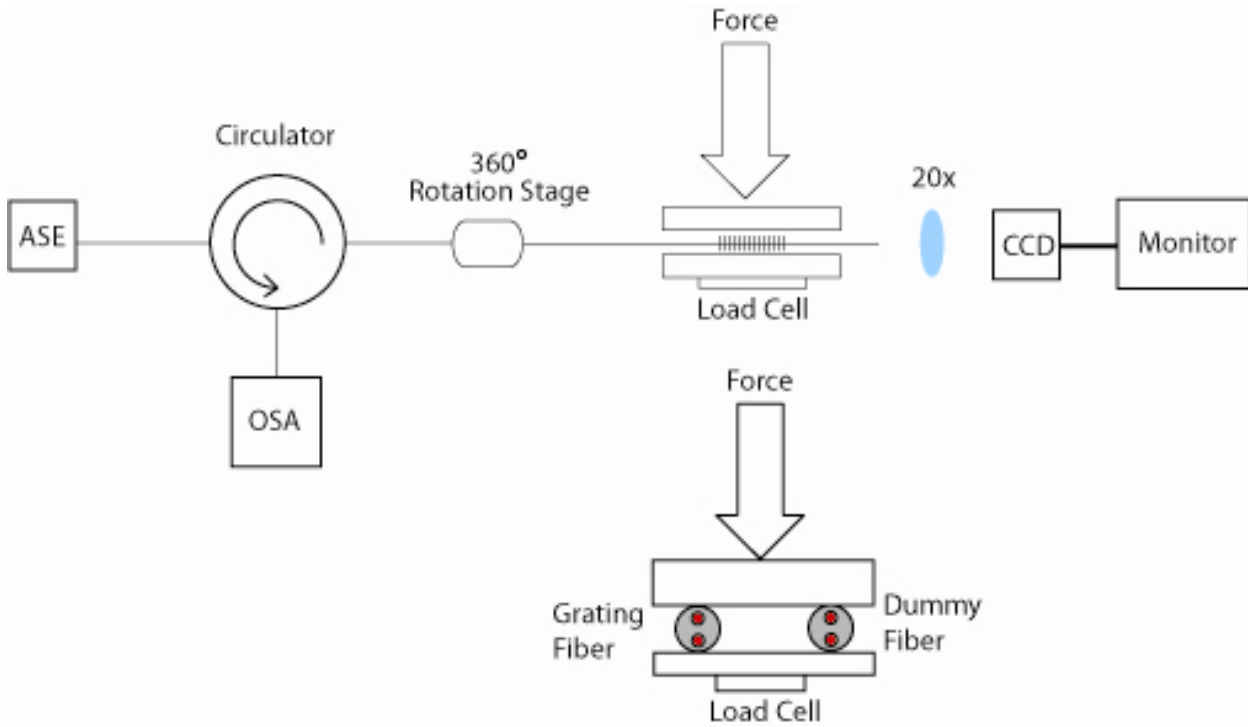


**Figure 38** Illustration of experimental setup.

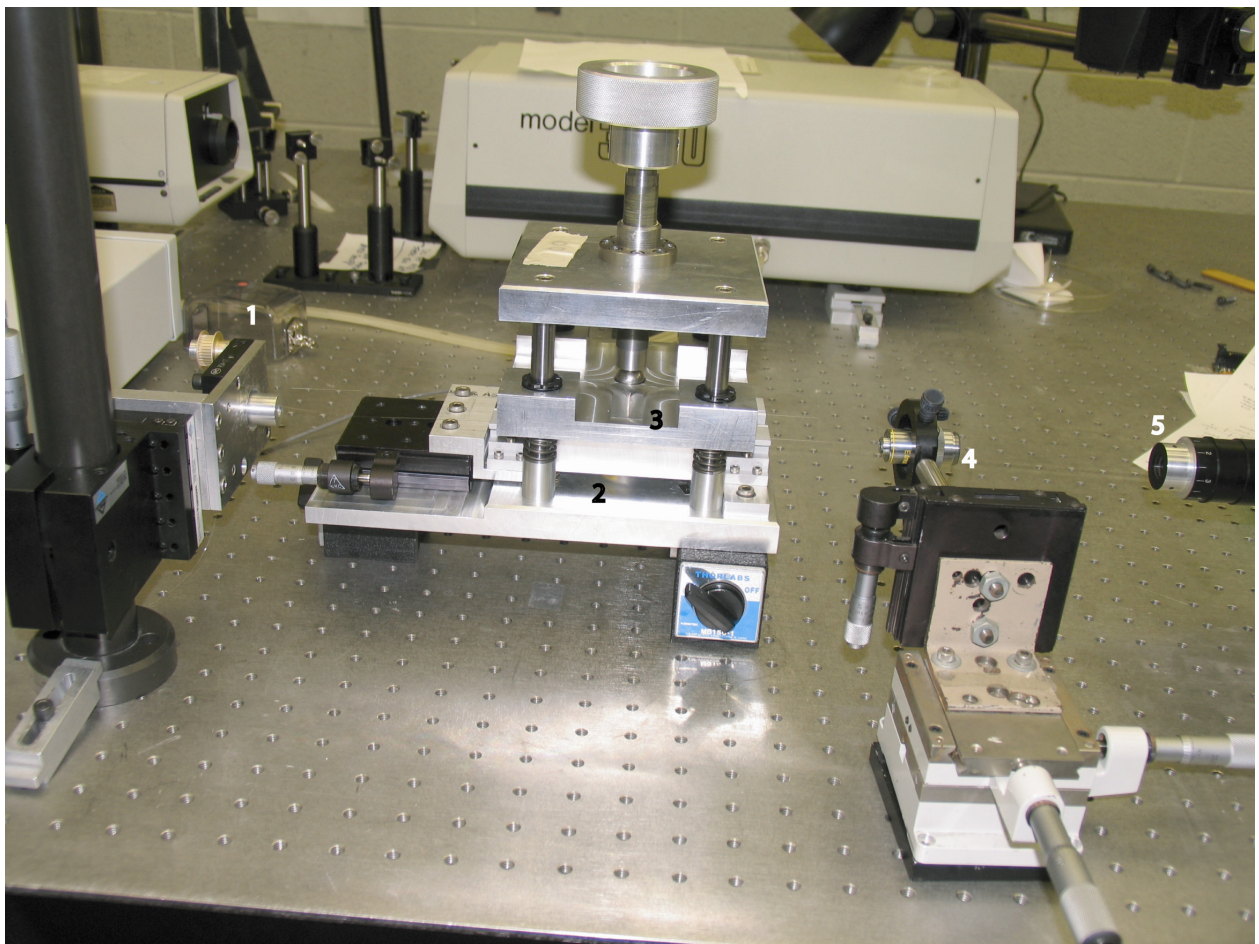


**Figure 39** Photograph of rotation stage (1), load cell (2), compression stage (3), microscope objective (4) and CCD camera (5)

## 5.2 RESULTS

### 5.2.1 SMF-28

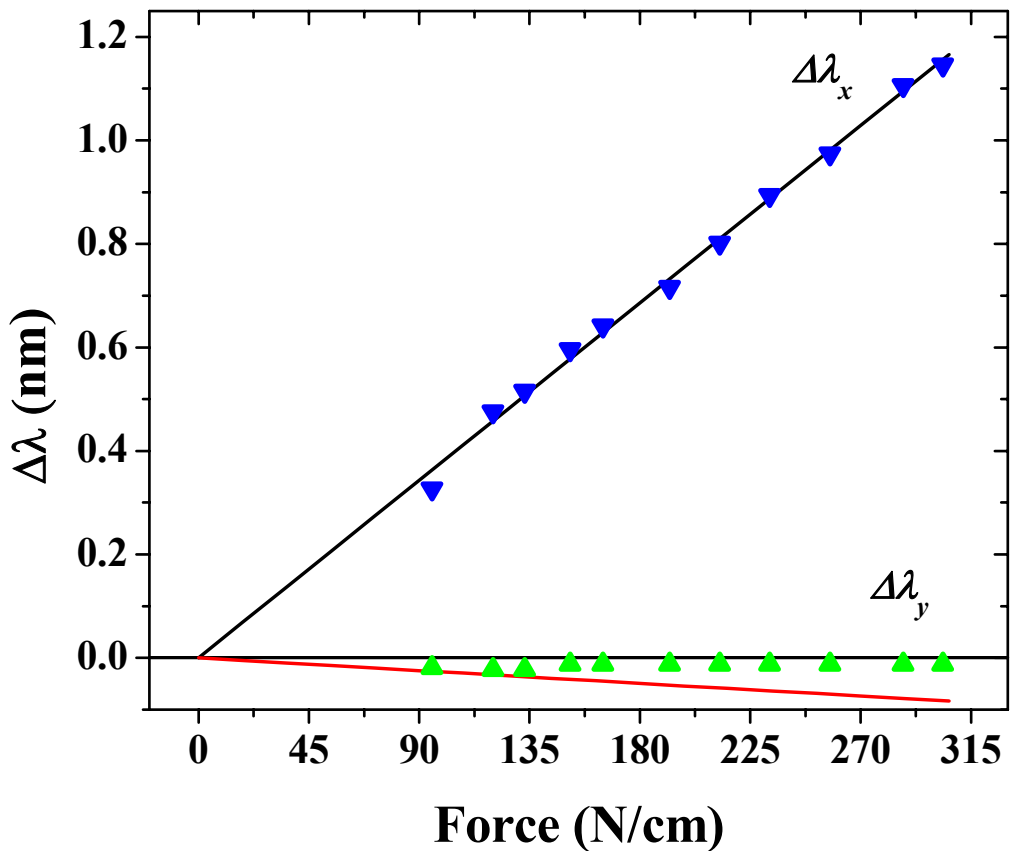


**Figure 40** Simulated and experimental results plot for SMF-28. The solid lines represent the simulated values

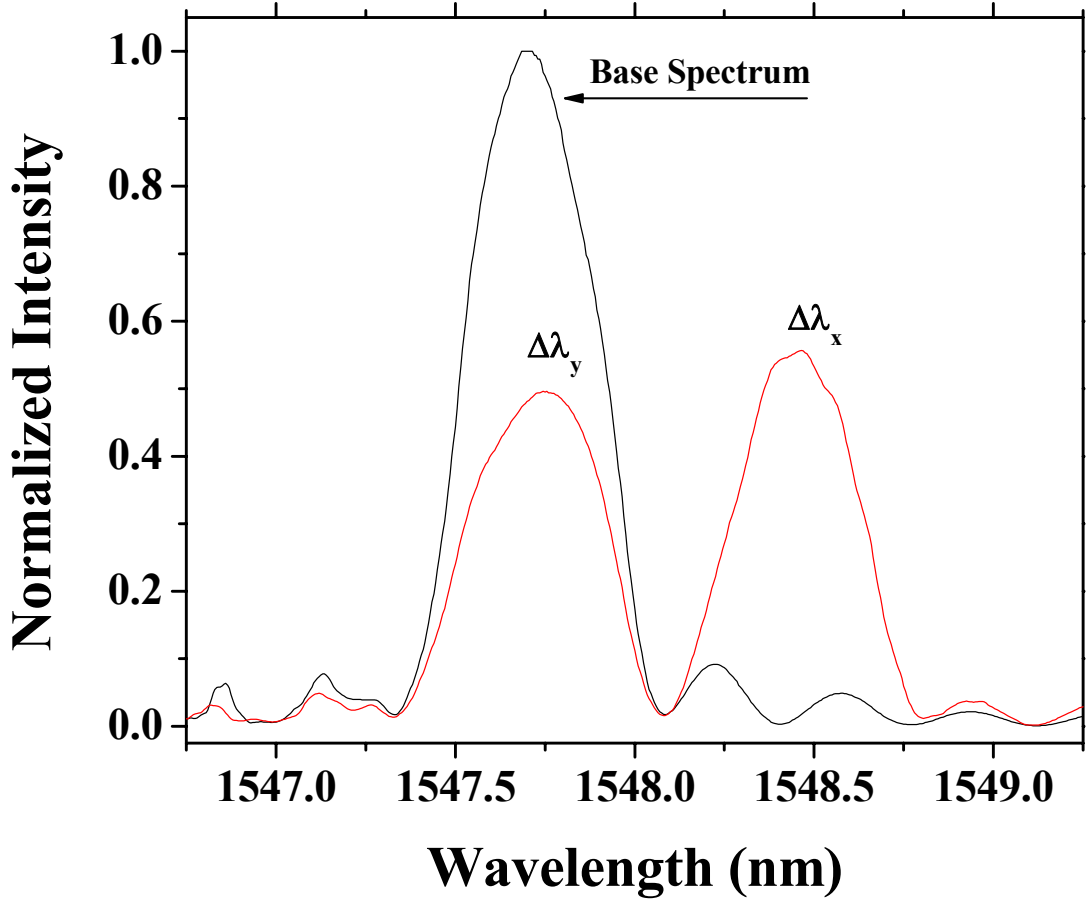


**Figure 41** Normalized spectral response of solid fiber at 197-N/cm

In Figure 40 the experimental results for the smf-28 are plotted against their simulation results and shows good agreement between the two. Figure 41 is an example of the peak splitting in the smf-28 fiber that was used to obtain the experimental values. These results will be discussed in greater detail in section 5.2.3.

### 5.2.2 Two-Hole Fiber

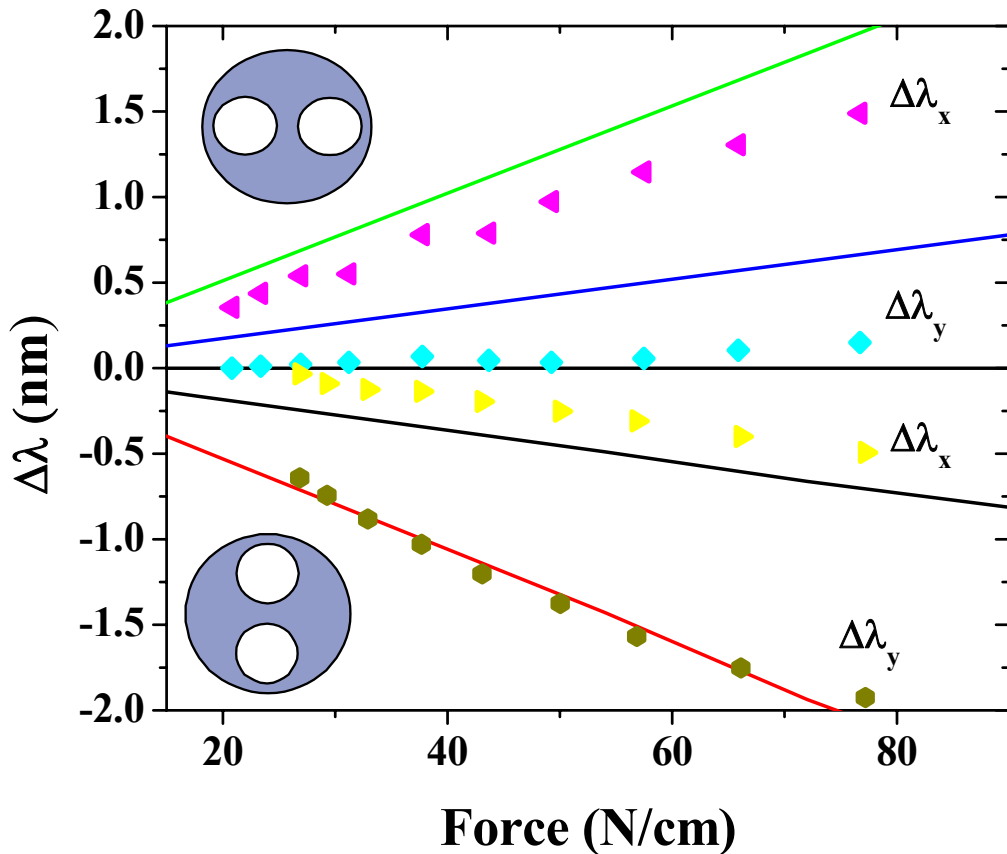


**Figure 42** Simulated and experimental results for two-hole fiber in vertical and horizontal orientations. The solid lines represent the simulated values.

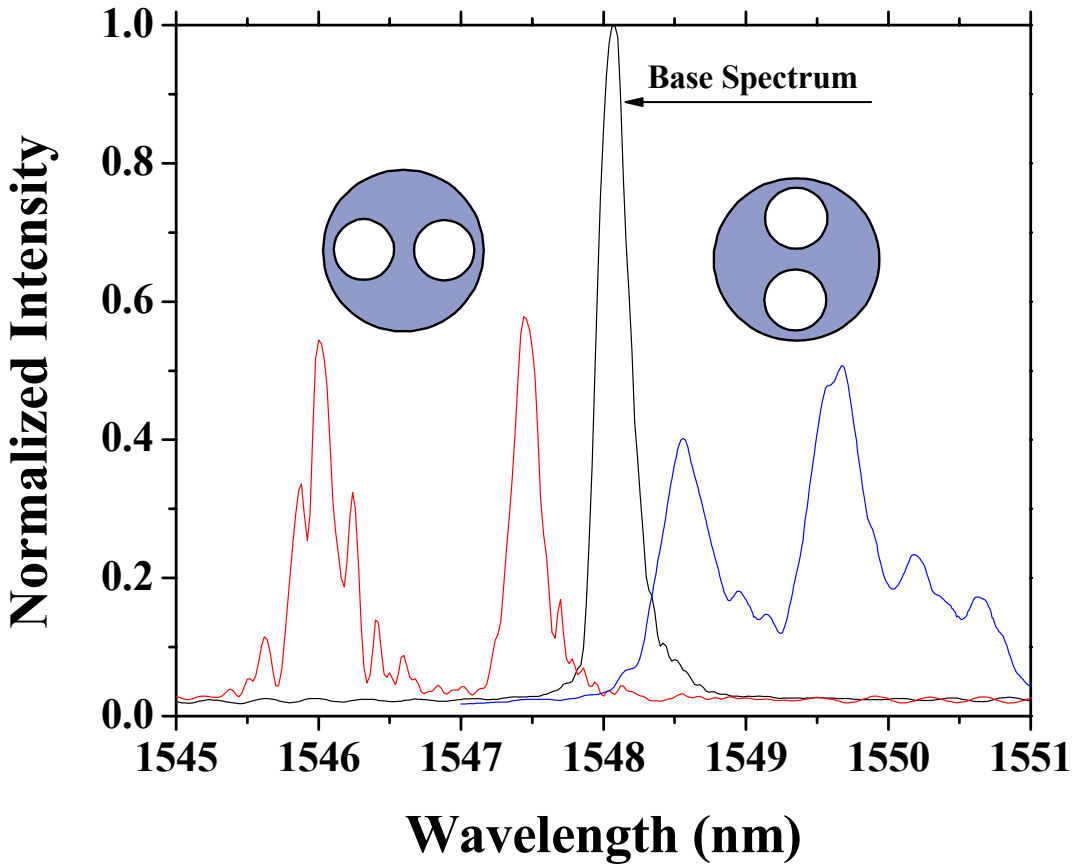


**Figure 43** Normalized spectral response of two-hole fiber for both vertical and horizontal orientations at 80-N/cm

In Figure 42 the experimental results for the smf-28 are plotted against their simulation results and shows that the peak splitting does follow the trend that was predicted. Figure 43 is an example of the peak splitting in the smf-28 fiber that was used to obtain the experimental values. More discussion of these results will be presented in the following section.

### 5.2.3 Comparison with Simulated Results and Discussion of Error

As one can see, the experimental results do compare qualitatively to those of the simulated results. For the SMF-28 the stress in the fiber is mainly dominated by a negative (compression) stress but has a presence of tensile (positive stress) which results in the X-polarization shifting more than the Y polarization (Figure 33). When the two-hole fiber is placed under the transverse load the vertical air holes cause a blue shift (Figure 34) in both of the polarizations. Looking at the stress profile in the ANSYS plots (Figures 26 and 27) one sees that when the air-holes are vertical, only a tensile stress is present. With the horizontal air-holes, both peaks experience a red shift (Figure 35) and the stress is entirely compressive (Figures 28 and 29). Therefore it makes sense that the SMF-28 has the shift of the peaks that it has. In fact a correlation can be deduced in that tensile stress causes more of a shift in the Y-polarization while compressive stress causes a greater shift in the X-polarization.

From the plotted results of the simulations and the experiments (Figures 40 and 41) we can see that the FEA is an excellent method in determining how the FBG will respond under stress. However there is noticeable discrepancy in some of the plots. This could arise from the fact that when making the model of the fiber in ANSYS, the air holes were assumed to be perfectly round. This is not the case, as one can see when looking at the photograph of the two-hole fiber (Figure 21). With the air holes not being perfectly round, they would in turn deflect or focus the stress differently throughout the fiber.

Another material effect that could have caused error in the peak splitting is the presence of air holes in the fiber cladding. Looking at the photograph of the fiber (Figure 21) it looks as if there are tiny air holes in the fiber. If this is the case, then these air holes could act as cushions and deflect the stress away or towards the fiber core. This in turn would cause the stress to be either greater or less than was predicted. We also assumed that the fundamental mode profile does not change as the stress is applied to the fiber for our simulations.

Finally the biggest and mostly likely cause of discrepancy in the splitting is the experimental setup. In the setup it was required to have a dummy fiber along with the fiber under test so that the compression would be even across the fiber. If the alignment of either of the fibers was not exact, then the stress profile in the fiber would not be as expected. As seen

with the splitting as a function of rotation (Figure 37) in the simulated results section any off-axis rotation of the fiber will greatly affect the magnitude of the FBG peak splitting and shift.

More importantly, it is necessary to point out that while the exact values of the peak splitting had some error in them, they did behave in the manner that the results from ANSYS predicted they would. This is extremely helpful because we now have a method to not only predict how the stress is in a fiber but also we have the ability to design different fiber structures to try and increase the stress or decrease the stress in the fiber core.

## **6.0 CONCLUSION**

### **6.1 SUMMARY**

In summary, this thesis presents the first systematic studies on the transverse stress impact on microstructure fibers. The combination of simulation and experimental studies promises the development of highly sensitive strain/acoustic fiber sensors. The introduction of air holes in fiber cladding not only increases the sensitivity of a microstructure fiber sensor to the external stress, but also provides the ability to determine the orientation of the external load.

This idea is first illustrated in this thesis using a finite element analysis (FEA) simulation and subsequently confirmed experimentally using a fiber with two air-holes design. Two air-holes reduce the reaction area in the fiber center and effectively focus the stress into the fiber core located between the two air holes. Comparing the solid fiber with the same diameter (220- $\mu\text{m}$ ), the introduction of two air holes with a diameter of 90- $\mu\text{m}$  increases compression stresses by 16 times in the center of twin-hole fiber than that in a solid fiber. The introduction of air holes also breaks the symmetry of the fiber, thus the response of the fiber to external load becomes orientation sensitive. To maximize the sensitivity of the FBG sensors, the fiber core should be placed right beside the air holes. The simulation results provide guidelines for the specialty fiber design and fabrication to produce high-sensitivity fiber transverse strain sensors.

Based on simulation results, a twin-hole fiber with a diameter of 220- $\mu\text{m}$  was chosen for experimental validation. The measurement results are qualitatively consistent with simulation results. The simulation yields a shift in FBG peak at a rate of 26-pm/N/cm for the dominant stress axis and 17.6-pm/N/cm for the other axis, respectively, which is 8 times and 4 times more than a 125- $\mu\text{m}$  diameter solid fiber. The loading experiments were performed with an external load up to 80-N/cm. Well defined FBG peak splitting due to the birefringence induced by the external loaded were clearly identified for a force exceeding 20-N/cm. FBG peak shifts for the

X-polarization are 4 times less than the theoretical prediction for the vertical hole orientation. The most likely cause of the discrepancy was the alignment of the two-hole fiber during the experimental setup. The simulated results show a strong dependency on the angular orientation of the fiber. If the fiber was off axis by even a small amount then that would account for the differences seen between the simulations and the measured results.

As part of the emerging fields of photonics, fiber optical devices based on microstructural fibers have found many exciting applications in telecommunications, sensing, micro-fluidic devices and bio-medical imaging. Many of these applications are unattainable by devices made in traditional fibers. Since microstructural fibers are not well understood, compared to traditional solid fibers, the detailed stress and thermal analysis of microstructural fibers is critical to determine device performance and to find new applications. The results in this work provide a first step towards this and provide proof to the optical fiber community that intelligent design of microstructural fibers can lead to revolutionary new devices and optical sensing systems.

## 6.2 FUTURE WORK

Both simulation and experimental works presented in this thesis were focused on twin-hole fibers since they were the only microstructure fiber available for these thesis studies. Although proof-of-concept results have been obtained, the two-hole structures are not optimized for maximum sensitivity to the transverse stress and birefringence sensing. For the future works, microstructure fibers (supplied by Dr. John Canning of Optical Fiber Technology Center at the University of Sydney, Sydney, Australia) with much more sophisticated air hole design can lead to a much more sensitive fiber sensor. In this section, we present detailed finite element analysis simulation on the mechanical response of various microstructure fibers. By adjusting sizes and locations of air holes and the fiber core, the fiber sensitivity to external strain can be significantly improved. Although experiment works have yet to be performed, we will work with a fiber manufacturer (StockerYale) to carefully balance the sensor performance with the mechanic integrity and manufacturability of specialty fibers. The fiber design and simulation work will provide guidance for fiber fabrication.

On the other hand, complimentary fiber structures can also be designed to produce fiber components that are immune to external impact, in the following sections, we will also present simulation results on this type of fiber.

### 6.2.1 Six-Hole Microstructured Fiber

It is possible to produce microstructured fiber that is highly orientation sensitive if it has the core region connected with supporting arms to the outer-shell of the fiber. An example is shown in Figure 44 below. The stress that is induced in the core by a transverse load can be controlled by the layout, number and size of the supporting arms.



**Figure 44** Cross sectional photograph of six-hole microstructured fiber (provided by Dr. John Canning of Optical Fiber Technology Center at the University of Sydney, Sydney, Australia)

This fiber has six symmetrical air holes placed in the fiber's cladding. The fiber's diameter is 125- $\mu\text{m}$  and the core is 8- $\mu\text{m}$  wide and placed in the fiber's center. Each air-hole is 40- $\mu\text{m}$  in length and 38- $\mu\text{m}$  in width at the widest point. The air-holes are tapered down towards

the center of the fiber and have an egg like shape profile. From the photograph the following model was created in ANSYS.

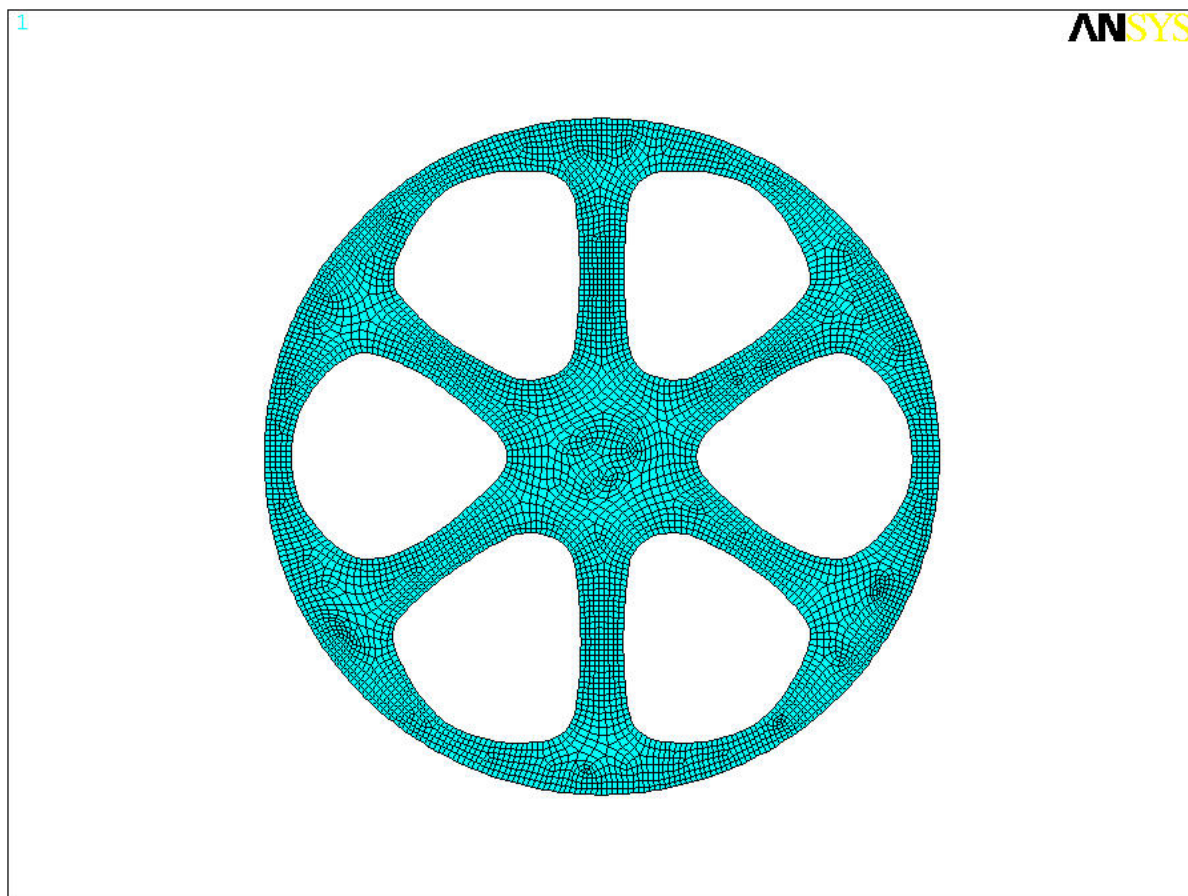


**Figure 45** Meshed ANSYS model of six-hole microstructured fiber

**ANSYS**

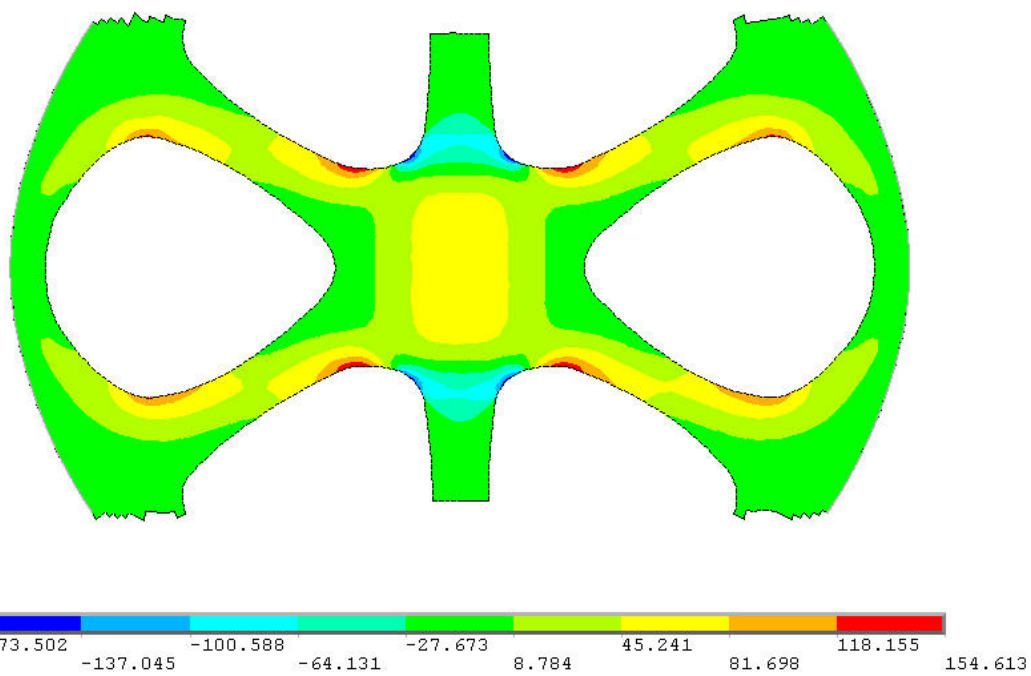


**Figure 46** Six-Hole microstructured fiber X-component of stress (F=50-N/cm)

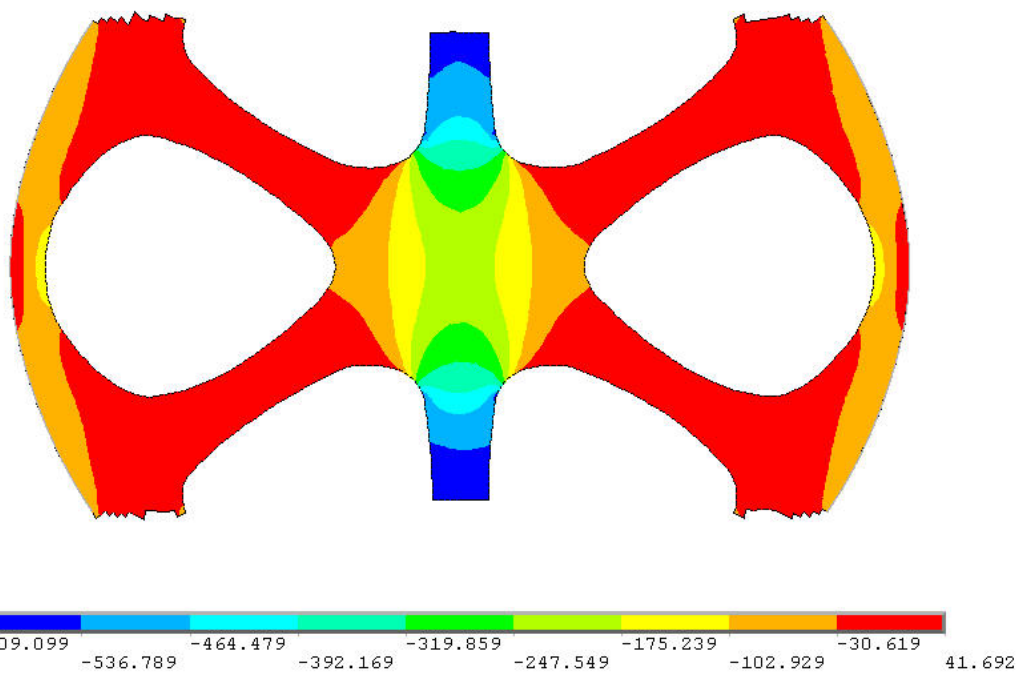


**Figure 47** Six-Hole microstructured fiber Y-component of stress (F=50-N/cm)

From the above contour plots shown in Figures 46 and 47 (F=50-N/cm) the X-component of the stress is approximately 70-MPa and Y-component is approximately -200-MPa. Compared to two-hole fiber with the core in the center (F=50-N/cm) the stress for the horizontal orientation is -23.298-MPa and -258-MPa for the X and Y-components respectively. The vertical orientation has values of 258-MPa and 23.298-MPa for the X and Y-components respectively. Whereas the two-hole fiber has the stress dominated by either tensile or compressive stress based upon the air-hole orientation, the six-hole fiber with the supporting arm parallel to the stress has both. In order to properly determine how the six-hole fiber will react, a model will need to be created with one of the air-holes parallel to the stress as opposed to the supporting arm. Detailed Stress profiles between the air-holes for both orientations of the six-hole fiber will need to be

performed along with the birefringence characteristics of this fiber to determine how the supporting arms affect both.

### **6.2.2 Pressure Sensor**

In addition of transverse stress sensing, high sensitive microstructure fiber sensors have many other applications. In this section, we present simulated results of two-hole fiber as a pressure sensor. As seen from the work done in this thesis it is possible to measure pressure by measuring the peak splitting in the FBG spectrum. It is possible to pressurize the air-holes in the fiber so that they act as a pressure conduit. This allows for the measurement of pressure in a thermally and mechanically stable environment [24, 25]. Continuing with the two-hole fiber that is available we will pressurize one air hole or both air-holes to study the FBG response to pressure. Detailed stress profiles are to be determined between the air-holes along with the profile of the birefringence of the fiber under these conditions.

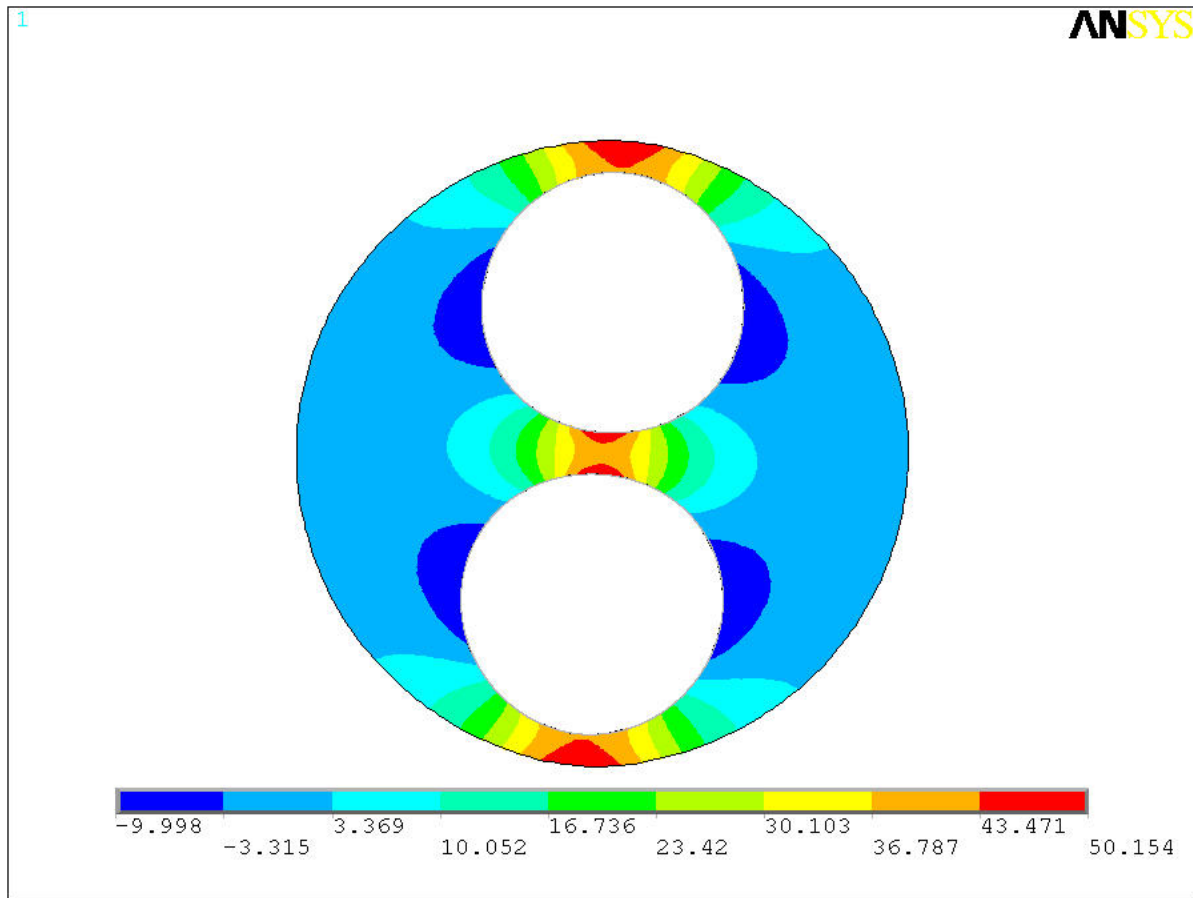


**Figure 48** Two-hole fiber with 100-Bar of pressure in both holes,  $\sigma_x$

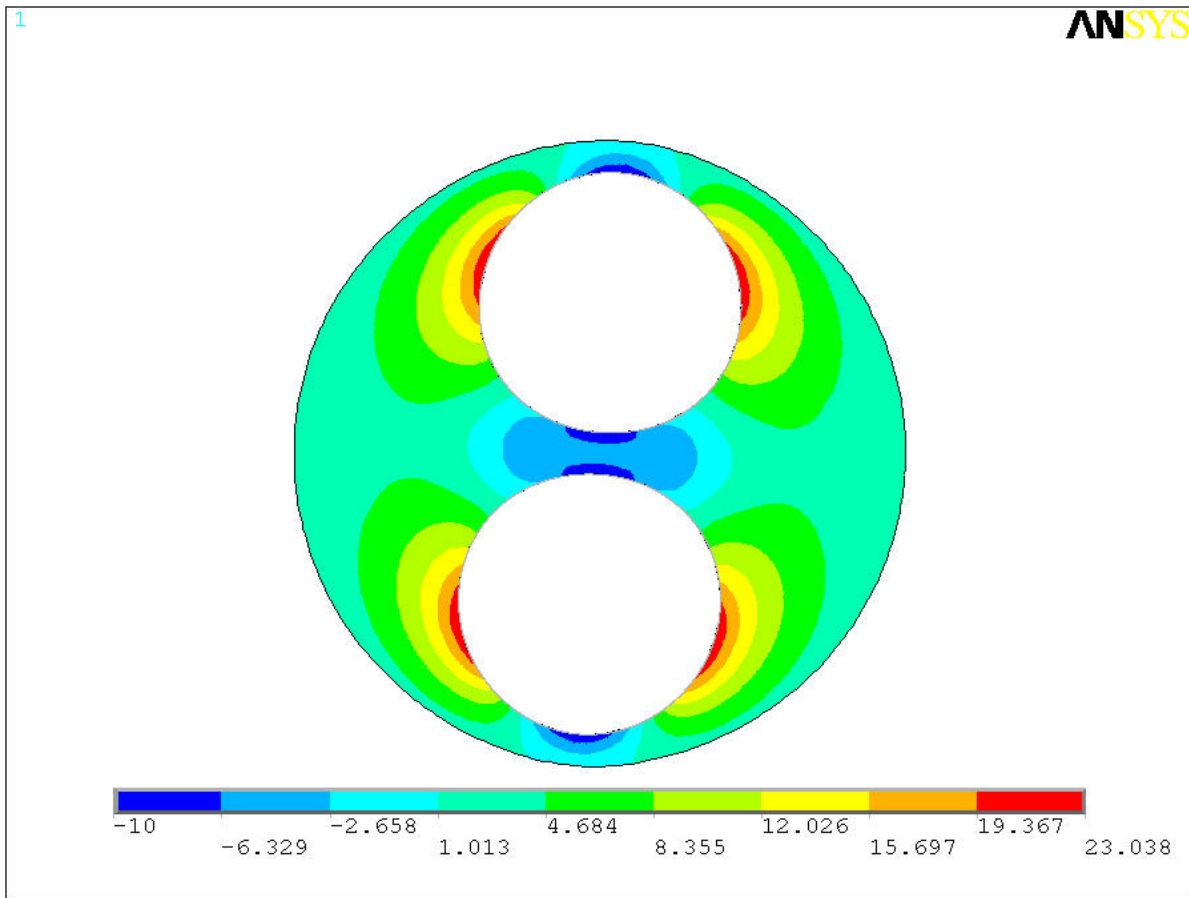


**Figure 49** Two-hole fiber with 100-Bar of pressure in both holes,  $\sigma_y$

When 100-bar of pressure has been applied to both air-holes as seen above in Figures 48 and 49 the X-component of the stress has an approximate value of 43-MPa and -10-MPa for the Y-component. This is substantially lower than when the fiber was placed under an external load. However, the maximum stress between the two air-holes is along the air-hole's edge and as such should produce a significant splitting in the resonance wavelength peak. This will allow us to monitor the pressure within the air-holes.

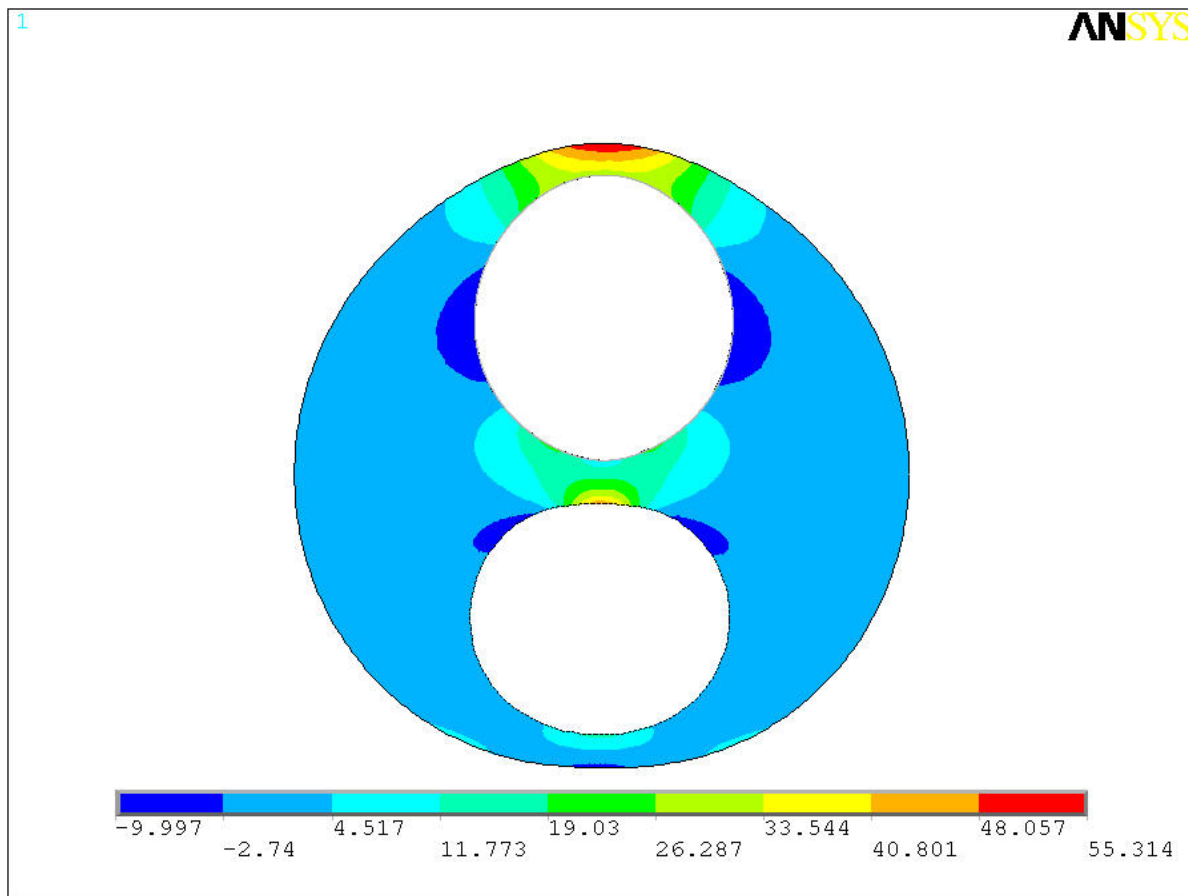


**Figure 50** Two-hole fiber with 100-Bar of pressure in one hole,  $\sigma_x$

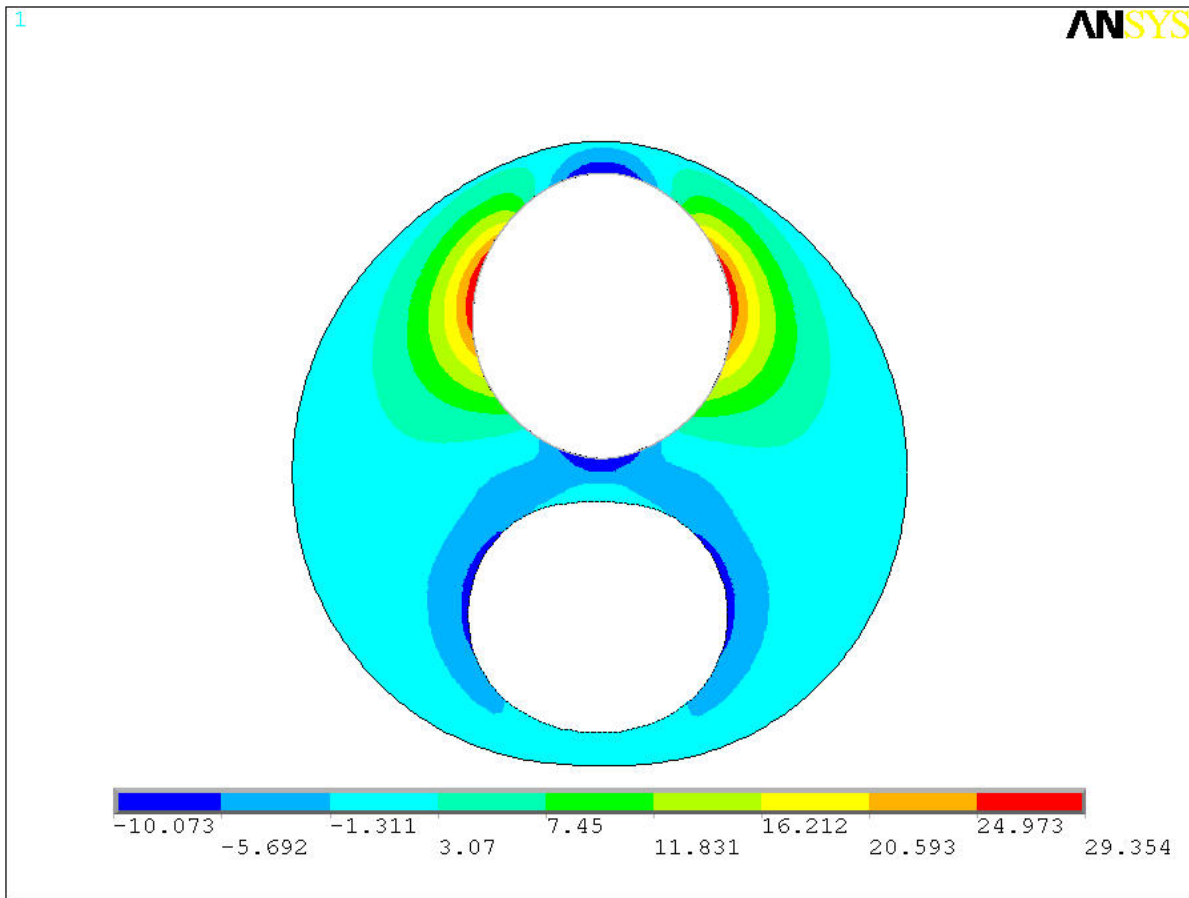


**Figure 51** Two-hole fiber with 100-Bar of pressure in one hole,  $\sigma_x$

When only one air-hole has pressure applied (upper air-hole) to it the maximum stress occurs along the edge of the air-hole that did not have pressure applied to it and can be seen above in Figures 50 and 51. Like with the pressure in both air-holes the stress profile between the air-holes will be determined. However, in measuring the birefringence the core stresses will be measured as if the core was closer to the pressurized air-hole than as if it was closer to the unpressurized air-hole. This will give a better understanding of how the fiber under these conditions will react.

The ANSYS simulations have indicated that the pressure inside the air-holes will introduce significant stress in the fiber core region, which can be effectively measured by FBG sensors. Using either a wavelength division multiplexing or time division multiplexing

technique, an FBG array in two-hole fiber can be used to measure pressure distribution in a number of applications including natural gas pipeline systems. Experiments will be carried out to verify the simulation results.

## BIBLIOGRAPHY

- [1]. Othonos, A. and K. Kalli, *Fiber Bragg Gratings, Fundamentals and Applications in Telecommunications and Sensing*. 1999, Norwood, USA: Artech House Publishing.
- [2]. A. D. Kersey, M. A. Davis, H. J. Patrick, M. LeBlanc, K. P. Koo, C. G. Askins, M. A. Putnam and E. J. Friebel, "Fiber Grating Sensors", *J. of Lightwave Technology*, **Vol. 15**, No. 8, 1442-1463 (1997)
- [3]. C. M. Lawrence, D. V. Nelson, E. Udd and T. Bennett, "A Fiber Optic Sensor for Transverse Strain Measurement", *Exp. Mech.*, **Vol. 39**, No. 3, 202-209 (1999).
- [4]. R. Gafsi and M. A. El-Sherif, "Analysis of Induced-Birefringence Effects on Fiber Bragg Gratings", *Opt. Fiber Technology*, **Vol. 6**, 299-323 (2000).
- [5]. C. C. Ye, S. E. Staines, S. W. Jaems and R. P. Tatam, "A polarization-maintaining fiber Bragg grating interrogation system for multi-axis strain sensing", *Meas. Sci. Technol.* **Vol. 13**, 1446 (2002).
- [6]. M. Silva-Lopez, C. Li, W. N. MacPherson, A. J. Moore, J. S. Barton, J. D. C. Jones, D. Zhao, L. Zhang and I. Bennion, "Differential birefringence in Bragg gratings in multicore fiber under transverse stress", *Opt. Lett.* **Vol. 29**, 2225-2227 (2004).
- [7]. Hill *et al.* "Photosensitivity in optical fiber waveguides: Applications to reflection filter fabrication," *Applied Physics Letters*, **Vol. 32**, 647-649 (1978).
- [8]. Meltz, G., W. W. Morey and W. H. Glenn, "Formation of Bragg gratings in optical fibers by a transverse holographic method," *Optical Letters*, **Vol. 14**, 823-825 (1989).
- [9]. Malo *et al.* "Fiber mode converters: point-by-point fabrication of index gratings, visualization using thermoluminescence and applications," *Optical Fiber Communications Conference*, San Diego, CA, Paper WL3 (1991).
- [10]. Hill *et al.* "Bragg gratings fabricated in monomode photosensitive optical fiber by UV exposure through a phase mask," *Applied Physics Letters*, **Vol. 62**, 1035-1037 (1993).
- [11]. Albert, J. *et al.* "Apodisation of the spectral response of the fibre Bragg gratings using a phase-mask with variable diffraction efficiency," *Electronics Letters*, **Vol. 31**, 222-223 (1995).

- [12]. Lam, D. K. W., and B. K. Garside, “Characterization of single-mode optical fiber filters,” *Applied Physics Letters*, **Vol. 20**, 440-445 (1981).
- [13]. Stone, J., “Photoreactivity in GeO<sub>2</sub>-Doped silica fibers”, *Journal of Applied Physics*, **Vol. 62**, 1987.
- [14]. Hand, D. P., and P. St. J. Russell, “Photoinduced Refractive-Index Changes in Germanosilicate Fibers.” *Optics Letters*, **Vol. 15**, No. 2, 102-104 (1990).
- [15]. Fiori, C., and R. A. B. Devine, “Ultraviolet irradiation induced compaction and photoetching in amorphous thermal SiO<sub>2</sub>,” *Materials Research Society Symposium Proceedings*, **Vol. 61**, 187-195 (1996).
- [16]. Atkins *et al.* “Mechanisms of enhanced UV photosensitivity via hydrogen loading in germanosilicate glasses,” *Electronics Letters*, **Vol. 29**, 1234-1235 (1993).
- [17]. Verhaegen *et al.* “Photorefractive waveguides produced by ion implantation of fused silica,” *Nuclear Instrumentation and Methods in Physics Research B*, **Vol. 106**, 438-441 (1995).
- [18]. Melle *et al.* “A passive wavelength demodulation system for guided-wave Bragg grating sensors,” *IEEE Photonics Technology Letters*, **Vol. 4**, 516-518 (1992).
- [19]. Jackson *et al.* “Simple multiplexing scheme for fiber-optic grating sensor network,” *Optical Letters*, **Vol. 18**, 1192-1194 (1993).
- [20]. Dunphy *et al.* “Instrumentation development in support of fiber grating sensor array,” *Society of Photo-optical Instrumentation Engineers, Distributed and Multiplexed Fiber Optic Sensors III*, **Vol. 2071**, 2-11 (1993).
- [21]. Xu *et al.* “Discrimination between strain and temperature effects using dual-wavelength fiber grating sensors,” *Electronics Letters*, **Vol. 30**, 1085 (1994).
- [22]. Nye, J. F., *Physical properties of crystals*. 1985, Oxford, United Kingdom: Oxford University Press.
- [23]. Becker, A. A., *Finite Element Analysis*. 2004, New York, New York, ASME Press.
- [24]. S. Kreger, S. Calvert, and E. Udd, “High pressure sensing using fiber Bragg gratings written in birefringent side hole fiber”, in *Optical Fiber Sensors Conference Technical Digest, OFS-15* (Institute of Electrical and Electronics Engineers, New York, 2002), pp. 355-358.
- [25]. E. Chmielewska, W. Urbańczyk, and W. J. Bock, “Measurement of pressure and temperature sensitivities of a Bragg grating imprinted in a highly birefringent side-hole fiber,” *Appl. Opt.* **42**, 6284 (2002).